Sustainable production of Fe-Ni alloys by hydrogen-based direct reduction of oxides

Master Thesis | Department of Materials Science and Engineering
Laura Zerafa

Delft University of Technology

TU Delft

2.5 μm

Sustainable production of Fe-Ni alloys by hydrogen-based direct reduction of oxides

by

Laura Zerafa

In fulfilment of the requirements for the Master of Science (M.Sc) degree in Materials Science and Engineering, at Delft University of Technology.

Student number:	6055648
Project duration:	November 1, 2024 – July 16, 2025
Supervised by:	Dr.-Ing. Yan Ma
Faculty:	Mechanical Engineering, Department of Materials Science and Engineering, Delft
Style:	Adapted from TU Delft Report Style, with modifications by Daan Zwaneveld

TU Delft

Acknowledgements

I would like to express my deepest gratitude to my supervisor, Dr.-Ing. Yan Ma, whose academic rigor, professionalism, and commitment to research have been a source of inspiration. I am also thankful to Dr. Poulumi Dey and Prof. Dr. Maria Santofimia Navarro for their guidance and kindly agreeing to serve on my thesis defence committee.

I am extremely grateful to Ing. Hans Brouwer, Drs. Richard Huizenga, Dhr. Ruud Hendrikx, and Ing. Kees Kwakernaak for their unwavering support in material characterisation and for the many insightful discussions over the course of this project. My thanks also go to the MSE Master coordinator, Dr. Sid Kumar, for his valuable assistance with the administrative aspects of the project. I wish to forward my thanks to PhD students Alice Dauzetac, Robert Bobbink, Dr. Daniel dos Santos Avila and Dr. Jungwan Lee for acts as mentors for me during this journey.

My profound appreciation goes to my family for the continuous support that such an intensive journey demands and whose encouragement has been a steady foundation throughout. This experience would not have been the same without the meaningful moments shared with course mates and friends. Above all, I thank God for the many blessings I have received throughout this journey—including the challenges, which have been essential to the learning process, and the individuals I have had the privilege of learning from along the way.

Abstract

Hydrogen-based direct reduction (HyDR) offers a fossil-free route for metalmaking, but its simultaneous application to iron- and nickel-oxides, combining reduction, alloying, and densification in a single solid-state step, has scarcely been studied. Crucially, no work has yet demonstrated HyDR for producing bulk Fe-Ni alloys with controlled microstructures. Furthermore, grain refinement of Fe-Ni alloys via austenite reversion without prior deformation and the attendant challenge of stabilising an austenite–ferrite duplex structure at room temperature remains largely unexplored. This study applies the '*one-step oxide-to-bulk-alloy*' concept to blended Fe_2O_3-NiO pellets, aiming for a fully reduced, dense Fe-Ni alloy with an ultrafine-grained austenite-ferrite duplex microstructure.

Thermogravimetric analysis confirmed near-theoretical mass loss (0.2936) and complete reduction (R = 1 ± 0.002) when the heating rate was limited to 5 °C min^{-1}. Sintering produced densities up to 7.3 g cm^{-3} with just 1.1 % porosity in Fe- 10wt.% Ni samples. Intercritical annealing of Fe-10 wt.% Ni at 560 °C maximised the driving force for the FCC phase, yet sluggish Ni diffusion limited the retained FCC to 5 vol.%. In contrast, Fe- 17 wt.% Ni annealed at 490 °C, achieved 15 vol.% FCC. The optimised TF_5/20_17Ni_490 alloy exhibited < 3% porosity, 0.93 ± 0.08 μm ultrafine-grains and a stable, two-phase microstructure comprising of a 15% Ni-rich FCC phase (25.63 wt.% Ni) and a 85 vol% Ni-lean BCC phase (14.16 wt.% Ni). This demonstrates HyDR's efficacy in producing bulk Fe-Ni alloys with controlled ultrafine-grained two-phase microstructures.

Table of contents

Preliminaries

List of abbreviations

Acronym	Definition
BCC	Body-centred cubic
BF-BOF	Blast furnace and basic oxygen convertor
BSE	Backscattered electrons
CI	Confidence interval
CLSM	Confocal laser scanning microscopy
EBSD	Electron backscatter diffraction
EDX	Energy dispersive x-ray spectroscopy
FCC	Face-centred cubic
GHG	Greenhouse gas
HAGB	High angle grain boundary
HyDR	Hydrogen-based direct reduction
IA	Intercritical annealing
KM	Koistinen-Marburger
K-S	Kurdjumov-Sachs
LIM	Linear intercept method
OR	Orientation relationship
OPS	Oxide polishing suspension
PAGB	Prior austenite grain boundary
PM	Powder metallurgy
RA	Reversed austenite
RKEF	Rotary kiln-electric furnace
SEM	Scanning electron microscopy
TEM	Transmission electron microscopy
TGA	Thermogravimetric analysis
TRIP	Transformation-induced plasticity
UFG	Ultrafine-grained
XRD	X-ray diffraction

List of symbols

Symbol	Descriptor/value
R	Degree of reduction ([-])
m_0	Initial mass (mg)
$m(t)$	Mass at a specific time point, t (mg)
m_f	Final mass (mg)
m_∞	Theoretical mass (mg)
k_{HP}	Hall-Petch constant
k_1	Linear regression constant (°C/wt.% Ni)
k_0	Linear regression constant (°C)
Q	Activation energy ($J \cdot mol^{-1}$)
R_G	Gas constant 8.314 ($J \cdot mol^{-1} \cdot K^{-1}$)
T	Temperature (°C or K)
T_Q	Quenching temperature (°C)
t	Time (s)
D	Diffusion coefficient ($m^2 \cdot s^{-1}$)
J	Diffusion flux ($mol \cdot m^{-2} \cdot s^{-1}$)
A_S	Total surface (interface) area of the compacted sample (m^2)
r_0	Initial radius of a particle (m)
d_γ	Average austenite grain diameter (µm)
d	Average grain diameter (µm)
M_s	Martensite start temperature (°C)
A_{e1}	Austenite transformation start temperature (K or °C)
A_{e3}	Austenite transformation finish temperature (K or °C)
β	Heating rate (°C/min)
f_{RA}	Fraction of reversed austenite
f_γ^{eq}	Fraction of austenite at equilibrium
$f_{\alpha'}$	Fraction of fresh martensite
γ_x	Interfacial energy (mJ)
Δy	Linear shrinkage (mm)
λ	Wavelength (Å)
x	Composition (wt.%)
ΔG_{oxide}	Gibbs free energy change of an oxide ($J \cdot mol^{-1}$)
ΔG_{H_2O}	Gibbs free energy change of H_2O ($J \cdot mol^{-1}$)
ΔG_r^0	Standard Gibbs free energy change of the reaction ($J \cdot mol^{-1}$)
μ_x^p	Chemical potential of elemental component in phase (kJ/mol) where x represents the component and p the phase.
M	Interface mobility (m^4/J·s)
σ_y	Yield strength (MPa)
σ_0	Friction stress (MPa)
P	Number of grain boundary intersections
$\overline{P_L}$	Intercept density $(\mu m)^{-1}$
$\bar{l}$	Mean intercept length (µm)
R^2	R-squared value

List of figures

List of tables

1. Introduction

Carbon dioxide (CO_2) accounts for approximately 74% of total greenhouse gas (GHG) emissions, making it a major driver of climate change due to its abundance and long-lasting presence in the atmosphere. The metal production industry, responsible for around 10% of total GHG emissions, plays a critical role in decarbonisation efforts [1,2].

Notably, the iron and steel sector alone are responsible for approximately 7% of total GHG emissions, with annual production reaching 1.89 billion tonnes as of 2023 [3]. As show in Table 1, the steel sector recorded the highest total CO_2 emissions among material industries in 2017, at 3.7 Gt, with a global production reaching 1.74 billion tonnes. This corresponds to a specific emission intensity of 2.13 tonnes of CO_2 per tonne of steel. By 2022, this intensity had decreased to 1.91 t CO_2/t indicating some efficiency improvements; however, overall emissions remain high due to the sheer scale of steel production [2].

Table 1. Comparison of carbon footprints for key material classes in 2017 and 2022, based on emission intensity (CO_2 per tonne of metal produced). Data for steel, aluminium, petrochemicals, and cements are sourced from Daehn et al. [4] while values for nickel and cobalt are taken from Raabe [5].

Material Class	CO_2 emissions associated with production in 2017 (Gt CO_2 per year)	Average specific CO_2 intensity in 2022 (tonne of CO_2 per tonne of metal produced)
Steel	3.70	1.91
Aluminium	1.00	14.40
Nickel, cobalt	0.01	20.00
Petrochemicals	1.50	1.70
Cement	2.20	0.86

Unless stated otherwise, production emissions include indirect emissions. Reported CO_2 intensities are current global averages and may vary with difference indirect-emissions accounting methods.

Nickel and cobalt production, while contributing relatively little to total global CO_2 emissions in 2017 (0.01 Gt), stands out as one of the most carbon intensive processes per unit of metal produced. As shown in Table 1, the global average emission intensity for nickel and cobalt has risen sharply, reaching 20 tonnes of CO_2 per tonne of metal in 2022, the highest among key material classes used in core industrial value chains worldwide. For nickel, this exceptional high intensity is driven by several factors including declining ore grades, growing reliance on carbon-intensive laterite processing, increasing demand for high-purity products, and the continued use of coal-based power in major producing regions. The primary sources of emissions are the extraction and refining stages, particularly smelting and chemical refining [5].

Recognising the significant environmental challenges posed by the metal production industry, the European Union has set an a legally binding target to achieve net-zero GHG emissions by 2050, effectively aiming for a 100% reduction compared with 1990 levels [6]. This ambitious initiative has inspired many non-European countries to establish their own decarbonisation strategies and policies, such as, but not limited to, China's National Key

Technologies R&D Program and India's Perform, Achieve, and Trade Scheme and Steel Scrap Recycling policy [2].

The blast furnace-basic oxygen furnace (BF-BOF) route dominates global steel production, accounting for 71.1% of crude steel output in 2023 [3]. This process relies heavily on fossil-based reductants (mainly coal and coke), producing an average CO_2 intensity of 2.33 tonnes per tonne of steel, in comparison to 1.37 tonnes for iron produced through direct reduction and electric arc furnace route [3]. Approximately 70% of global nickel production relies on the extraction from lateritic ores, which is significantly more energy-intensive due to the low nickel concentration (~1-2%) in these ores [7,8]. Processing, especially in Indonesia and the Philippines, often involve coal-fire power and energy-demanding methods such as rotary kiln-electric furnace (RKEF) smelting, acid leaching, and carbonyl refining [8].

These statistics underscore the critical need for transformative approaches to iron and nickel ore reduction processes that drive towards decarbonisation. In recent decades, researchers have increasingly focused on exploring various carbon alternatives, with hydrogen-based direct reduction showing significant promise. HyDR has achieved a technology readiness level between 6 and 8 and is approaching widespread industrial deployment [9]. Its ideal implementation involves using "green hydrogen", hydrogen produced entirely through renewable energy sources. This process generates only water, offering a truly sustainable approach. Studies suggest that using HyDR, with hydrogen sourced using renewable energy, could reduce CO_2 emissions in the iron and steel sector by 78-95% [10,11].

2. State of the art

2.1. A sustainable approach for iron nickel alloy production

The '*one-step oxide to bulk alloy*' approach offers a sustainable method for alloy production by directly reducing metallic ores with hydrogen, eliminating the CO_2 emissions associated with fossil-based metal extraction. Illustrated in Figure 1(a) by merging traditionally separate steps, metal extraction, atomic-scale elemental mixing, and bulk compaction, this approach represents a fundamental reimagining of metallurgical production techniques. Additionally, it significantly reduces energy costs linked to liquid processing, and leverages diffusion processes for direct material compaction. Figure 1(b) compares the energy efficiency of the one-step process with that of traditional multi-step methods [12].

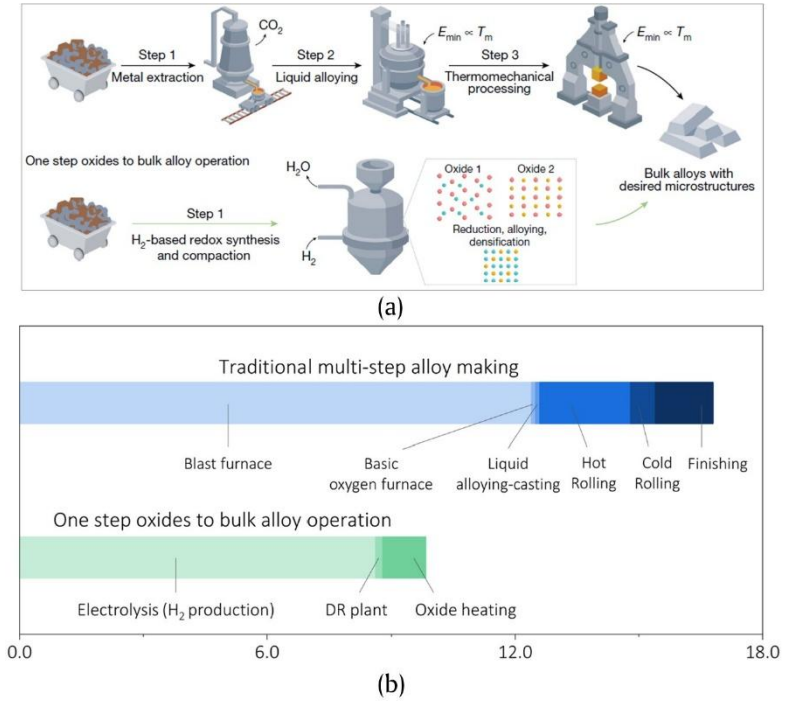

Figure 1. Comparison of (a) process steps and (b) energy consumption between the traditional multi-step alloy making route and the proposed 'one-step hydrogen-based direct reduction' approach [12].

Recognising the substantial environmental impact of processing both iron and nickel, a choice was made to apply the '*one-step from oxides to bulk alloy*' approach, proposed in literature [12], to the production of bulk Fe-Ni alloys. These alloys are in high industrial demand due to their widespread used as a base composition in maraging steels, cryogenic steels and Invar alloys due to their unique mechanical and thermal properties [13–17].

2.2. Thermodynamic feasibility and reaction mechanisms of Fe-Ni oxide reduction and alloy formation

This section outlines the thermodynamic principles that govern the hydrogen-based direct reduction of Fe and Ni oxides. The reaction mechanisms and pathways are also discussed giving depictions of the process on an atomic scale. Explanations give detail as to how hydrogen dissociates, reacts with the Fe- and Ni- metal oxides, and facilitates their transition to metal.

2.2.1. Thermodynamic viability of Fe-Ni oxide reduction and alloy formation using hydrogen

The direct reduction of metal oxides by hydrogen is fundamentally governed by thermodynamic principles that determine the feasibility and efficiency of the reduction process [18,19]. Figure 2(a) plots the change in mixing enthalpy between Fe and element, X, on the y-axis and the driving force for their reduction with hydrogen from their oxide states at 700 ℃ under standard pressure. The x-axis represents $\Delta G_{oxide} - \Delta G_{H_2O}$, from which a positive value indicates both a spontaneous reaction for the oxide of material, X, to be directly reduced by hydrogen to its metallic state and the formation of H_2O from its molecule. Ni exhibits propensity towards both compound formation and a high driving force for direct reduction by hydrogen in relation to other elements taken into consideration [12,19]. The calculated Ellingham diagram, illustrated in Figure 2(b), further supports this behaviour, showing the oxidation reactions of Fe at different valence states and Ni oxides lie above the $2H_2 + O_2 \rightarrow 2H_2O$ reaction line, at temperatures exceeding ~600 ℃. This confirms the that the oxides of both Fe and Ni across different valence states can be fully reduced by hydrogen to metallic Fe and Ni [12].

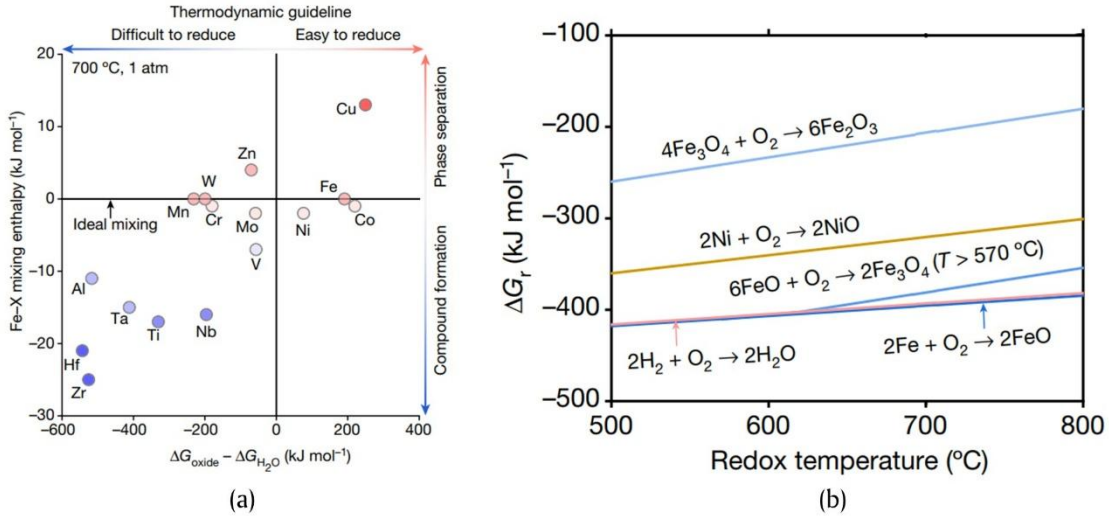

Figure 2. (a) Design treasure map based on thermodynamics. Reducibility of Fe-X with hydrogen is represented by the x-axis (ΔG_{oxide}- ΔG_{H2O}) and is considered for oxides with highest valence states at 700 ℃ under 1 atm (b) Ellingham-Richardson diagram for the oxides of iron (Fe_2O_3, Fe_3O_4, FeO), and nickel (NiO) under standard conditions (1 atm) [12].

The Baur Glässner diagram, shown in Figure 3, depicts the equilibrium-based reaction pathways of Fe- and Ni- oxides as a function of hydrogen partial pressure and temperature. This diagram is a useful tool for predicting the reduction behaviour of the system [20,21]. For temperatures greater than approximately 500 ℃, the reduction of Fe_2O_3 involves multiple sequential steps, proceeding through intermediate oxide phases before reaching metallic iron. In contrast, NiO reduces directly to metallic Ni under relatively low hydrogen partial pressures across the entire temperature range. Similarly, the initial reduction of Fe_2O_3 to Fe_3O_4, requires only negligible hydrogen partial pressures across at all temperatures, indicating favourable thermodynamic driving force. This is consistent with Figure 2(b), which illustrates large Gibbs free energy change associated with these reduction reactions [21]. Based on these thermodynamic tools, the simultaneous hydrogen-driven direct reduction of NiO and Fe_2O_3 to their metallic states and concurrent intermetallic compound

formation, emerges as a thermodynamically viable approach for producing a Fe–Ni alloys from a homogeneous oxide mixture.

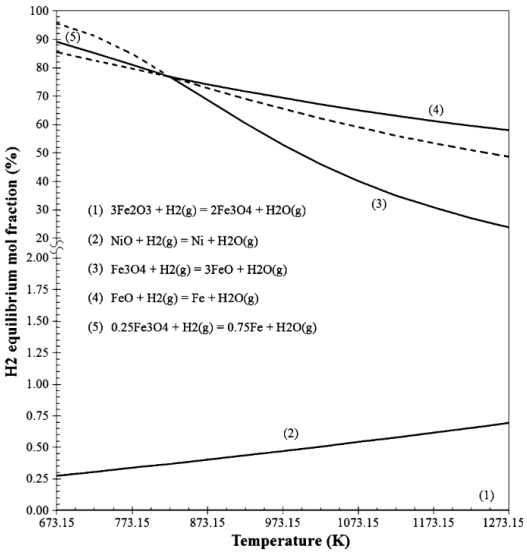

Figure 3. The Baur-Glässner (or phase stability) diagram of the Fe- and Ni-O-H systems [21].

2.2.2. Reaction mechanisms during HyDR of Fe–Ni oxide systems

The reaction steps involved in hydrogen direct reduction are analogous to those observed in other oxide reduction processes using hydrogen. At elevated temperatures, hydrogen molecules (H_2) dissociatively adsorb into vacant interstitial sites on the oxide surface. This is followed by the formation of OH^-, until the second hydrogen atom bonds resulting in the formation of H_2O. finalising the reaction. Subsequently, the resulting water molecule either adsorbs onto the surface or desorbs and evaporates into the gas phase [22,23]. The overall reaction sequence is shown in reactions (r.1 –r.3).

$$H_2 + 2V_a \rightarrow 2H^+ \quad \text{(r.1)}$$

$$H^+ + O^{2-} \rightarrow OH^- + e^- \quad \text{(r.2)}$$

$$OH^- + H \rightarrow H_2O + e^- \quad \text{(r.3)}$$

Where V_a represents a vacant interstitial site on the oxide surface where hydrogen atoms can temporarily reside before participating in further reactions. The reduction sequence relies on the surface, bulk, and defect diffusion of H^+ and O^{2-}. Elementary processes of diffusion and reactions occur at internal phase boundaries between oxide/oxide interfaces [22]. These mechanisms describe and predict the rate of nucleation and growth of the new phase [24]. Figure 4(a) illustrates the reduction of hematite (Fe_2O_3) to magnetite (Fe_3O_4) with hydrogen. During this process, hydrogen gas interacts with the oxide surface by first dissociating into a monoatomic form. This reaction occurs on a free oxide surface (V_a), surrounded by open-pore channels. As hydrogen removes oxygen from the surface (by the formation of H_2O), an activity gradient of Fe^{+2} ions develops across the magnetite phase. The $Fe^{2+}$and electrons migrate toward the internal reaction interfaces, where they react with hematite to produce magnetite, as represented by reaction (r.4) [22].

$$4Fe_2O_3 + Fe^{2+} + 2e^- \rightarrow 3Fe_3O_4 \quad \text{(r.4)}$$

Similarly, when magnetite is reduced to wüstite (FeO_x), the reaction at the magnetite/wüstite interface is given by reaction (5). Note, that wüstite is rarely perfectly stoichiometric, due to the presence of iron vacancies and excess oxygen, and must therefore be accurately represented as FeO_x [20].

$$Fe_3O_4 + Fe^{2+} + 2e^- \rightarrow 4FeO_x \quad \text{(r.5)}$$

Once a dense iron layer forms, the reduction mechanism changes. Oxygen atoms must diffuse from the iron/wüstite interface to the iron/gas interface, as shown in Figure 4(b). At the iron/gas interface, hydrogen reacts with oxygen to form water (H_2O), as described in the reactions (r.1-r.3). The driving force for outbound oxygen diffusion is the gradient of oxygen activity, which moves oxygen from the internal iron/wüstite interface through the iron layer to the external iron/gas interface. At the internal reacting interface, wüstite dissociates into iron and oxygen according to reaction (r.6) [22,25].

$$FeO_x \rightarrow Fe + O \quad \text{(r.6)}$$

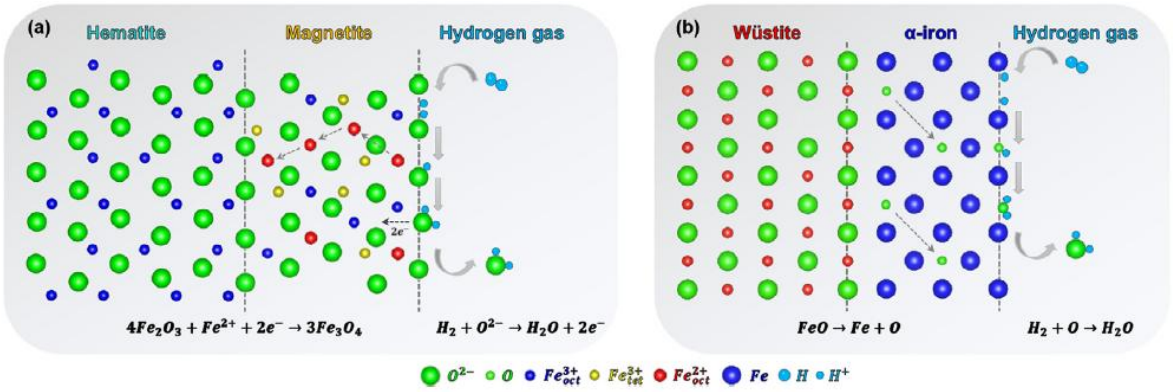

Figure 4. Schematic illustration depicting hydrogen-based direct reduction mechanisms on an atomic scale (a) reduction of trigonal hematite to cubic magnetite and (b) reduction of cubic wüstite to cubic α-iron [22].

The reduction of NiO follows a simpler mechanism compared with Fe_2O_3, as NiO is a single-phase oxide that does not require multiple intermediate phase transformations (r.7). Following the dissociation of hydrogen into atomic hydrogen, they react with the NiO surface, removing oxygen and forming water vapour. The water vapour then desorbs from the nickel surface and flows through the gas layer, preventing reoxidation and allowing the reduction to continue efficiently.

$$Ni^{2+} + 2e^- \rightarrow Ni \quad \text{(r.7)}$$

When a mixture of iron (III) oxide (Fe_2O_3) and nickel oxide (NiO) is reduced, both oxides undergo simultaneous direct reduction in a hydrogen-based atmosphere. This process is depicted schematically in Figure 5. Since NiO does not form intermediate oxide phases like Fe_3O_4 or FeO_x, the reaction is generally faster than iron oxide reduction. At sufficiently high

temperatures, diffusion mechanisms become active, and the resulting metallic Fe and Ni species begin to sinter, ultimately leading to the formation of a bulk Fe-Ni alloy [12]. During this process, complex nickel-iron oxides may form as intermediate or transient phases, potentially altering the reduction pathway and delaying full conversion to metallic phases. However, it has been shown that the formation of stable mixed oxides such as $NiFe_2O_4$, typically requires prolong annealing, over 30 hours, at temperatures of around 1200 ℃ [26].

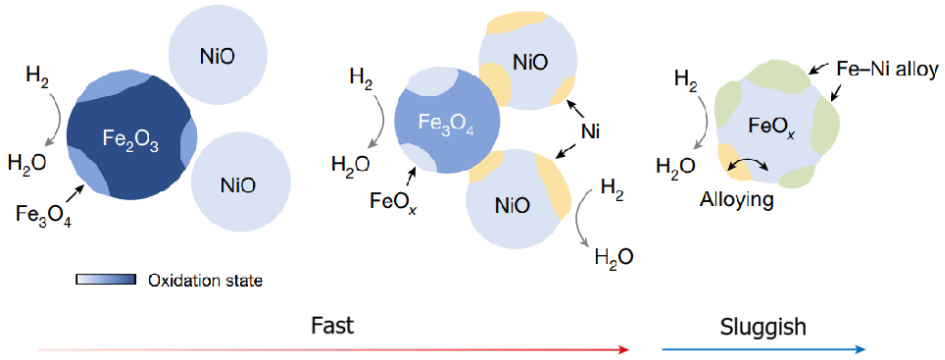

Figure 5. Schematic of the stepwise reduction of iron and nickel oxide. Adapted from Wei et al [12].

Experiments conducted by Wei et al. [12] showed that the first reduction step, $Fe_2O_3 \rightarrow Fe_3O_4$ (left Figure 5), began at approximately 350 °C shown in Figure 6(a), resulting in a continuous increase in the Fe_3O_4 phase fraction which reached around 0.68 at 600 °C. The reduction of NiO started at a slightly higher temperature of about 400 °C, with its phase fraction steadily decreasing as the reaction progresses. From 400 °C onward, a metallic face-centred cubic (FCC) phase, confirmed to be pure Ni, emerged, and its fraction steadily increased to approximately 0.15 by the end of the heating process at 700 °C (Figure 6(a)). During isothermal holding, the NiO phase was fully reduced, corresponding to a further increase in the metallic FCC phase fraction. The Fe_3O_4 phase fraction initially remained constant, followed by the $Fe_3O_4 \rightarrow FeO$ (middle Figure 5) transformation, which peaked at a FeO phase fraction of approximately 0.43. For the remainder of the isothermal holding period, the metallic FCC phase fraction continued to increase, while the phase fraction of FeO_x decreased. As shown in Figure 6(b), the complete reduction of FeO_x to Fe proved to be the slowest step in the overall process.

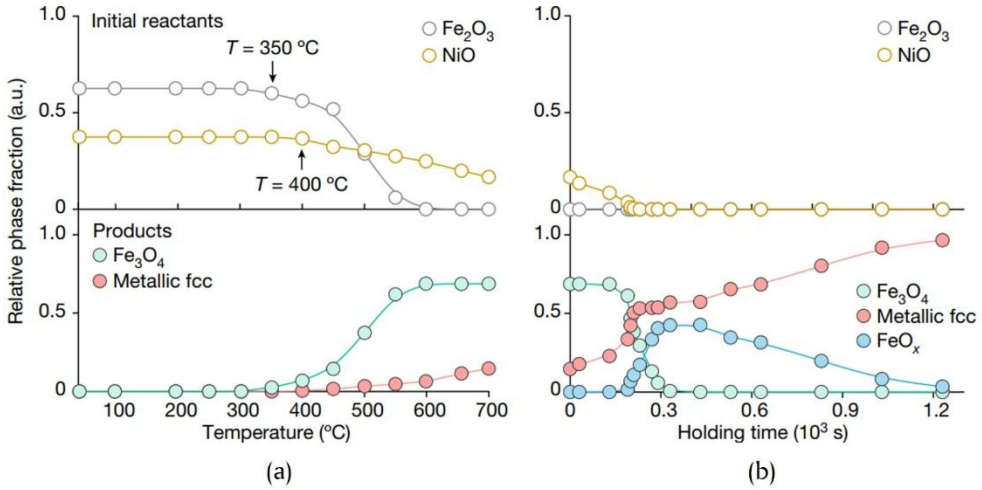

Figure 6. Changes in phase fraction with (a) temperature (°C) and (b) holding time (10^3 s) [12].

2.3. The benefits of ultrafine-grained duplex phase microstructures

There is well-established consensus in the literature regarding the advantages of a duplex phase microstructure, particularly the combination of austenite and ferrite, over a single-phase microstructure. Figure 7(a, b) illustrates electron backscatter diffraction (EBSD) images of an austenitic and duplex stainless steel respectively, both subjected to identical cold rolling and recrystallisation procedures. From the EBSD images, it is evident that the duplex stainless steel exhibited a finer grain size (~1-10 μm) compared with the austenitic alloy. The difference in phases arise from the duplex stainless steel's higher chromium and lower nickel content, which promoted the mixture of ferrite (34%) and austenite (66%) (Figure 7(b)). In contrast, the fully austenitic microstructure is attributed to the higher content of austenite stabilisers, such as Ni, Mn, Cu, and N [27]. As shown in Figure 7(c), a separate study compared the tensile strength and strain percentage of duplex stainless steel with those of austenitic and ferritic stainless steels. The duplex stainless steel exhibited a superior combination of high-tensile strength and good ductility compared to both austenitic and ferritic grades [28]. In duplex microstructures, ferrite contributes to strength, while austenite enhances ductility and toughness, partly due to the transformation-induced plasticity (TRIP) effect [27,29,30].

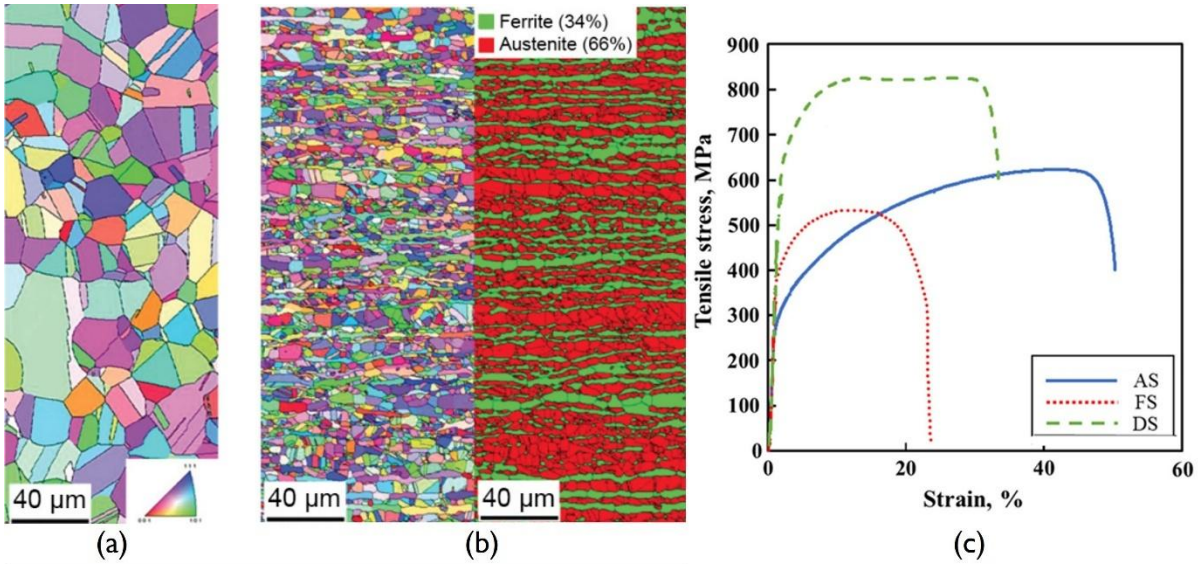

wt. %	C	Mn	Ni	Cu	Si	Cr	N	Fe
Austenitic SS	0.08	8.5	1	1.5	0.5	16	0.20	Bal.
Duplex phase SS	0.1	8	-	-	0.5	20	0.17	Bal.

Figure 7. Electron backscattered analysis of (a) austenitic and (b) duplex phase stainless steel with phase maps and wt.% compositions; both cold-rolled and recrystallised identically. Adapted from Jung et al. [27] (c) Mechanical properties of austenitic (AS), ferritic (FC), and (DS) phase stainless steels [28].

Refining fine-grained structures to a range within the ultrafine range (~0.1-1 μm) can significantly improve mechanical properties. In particular, yield strength increases in accordance with the Hall-Petch relationship: $\sigma_y = \sigma_0 + k_{HP} d^{-1/2}$ [31–33]. In this equation, σ_y is the yield strength, σ_0 represents the intrinsic resistance to dislocation motion, k_{HP} is the Hall–Petch slope that quantifies the effectiveness of grain boundaries in impeding dislocation movement, and d is the average grain diameter. Despite these benefits, Miller noted that [31] achieving and maintaining an ultrafine-grained (UFG) structure is challenging because of a strong tendency for grain growth. Many fine- and UFG microstructures are inherently unstable, and without a mechanism to restrict grain boundary movement, they will not retain their fine structure. A stable, UFG microstructure is typically achieved by intercritical annealing of cold-worked ferrous alloys [34–36]. Cold working, such as cold rolling, generates a high dislocation density, providing numerous nucleation sites for austenite formation. The resulting grain impingement limits grain growth, thereby stabilising the UFG microstructure [37]. However, in the case of adopting the '*one step from oxides to bulk alloy*' approach which uses HyDR, prior cold working is not possible [12]. An UFG microstructure can otherwise be obtained through careful control of phase transformations [38,39].

2.4. Heat treatment steps to form a fully reduced Fe-Ni bulk alloy with an ultrafine-grained duplex microstructure

This section discusses how heat treatment steps affect reduction, densification, and the final microstructure of Fe-Ni alloys produced via HyDR, aiming for an ultrafine-grained duplex microstructure. It explores the reduction and sintering conditions needed for complete reduction and full densification, emphasising the role of each with one another. A method for selecting intercritical annealing temperatures, based on predicted austenite retention

under equilibrium, is presented. Experimental findings from literature are given to highlight the practical effects of intercritical annealing temperature, holding time, and the heating/cooling rates before and after intercritical annealing on microstructural evolution and the characteristics of the final microstructure.

2.4.1. Reduction and sintering

A sintering step is required to consolidate the reduced Fe-Ni powder into a dense and bulk alloy. The driving force for sintering metallic compacts is the reduction of total interfacial energy. For a powder compact, the total interfacial energy is represented as $\gamma_I A_s$, where γ_I denotes the specific surface (interface) energy and A_s represents the total surface (interface) area of the compact. This energy reduction can be expressed mathematically as

$$\Delta(\gamma_I A_s) = \Delta\gamma_I A_s + \gamma_I \Delta A_s$$

In this equation, the change in interfacial energy ($\Delta\gamma_I$) results from densification, while the change in interfacial area (ΔA_s) is attributed to grain coarsening. In the context of HyDR of Fe- and Ni-oxides, solid-state sintering occurs. Change in interfacial energy occurs due to the transformation of solid/vapor interfaces (surface) into solid/solid interfaces. As illustrated schematically in Figure 8, the reduction in total interfacial energy occurs through two primary mechanisms: densification and grain growth, both of which are fundamental to the sintering process [40,41].

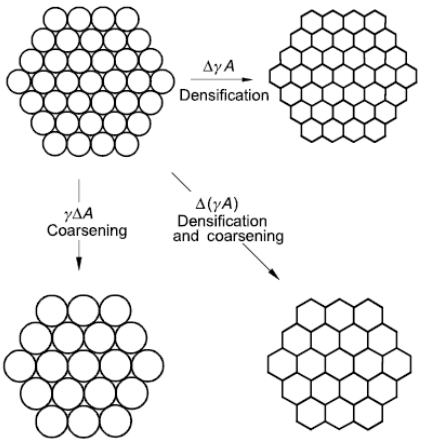

Figure 8. Fundamental processes that take place during sintering under the influence of the sintering driving force, γ_I (ΔA_s) [40].

The sintering behaviour of two spherical particles is primarily determined by two fundamental parameters: the neck radius (r) and the linear shrinkage (Δy). The latter is defined as the relative distance between the crystalline lattices of the two particles, here Fe_2O_3 and NiO, normalised by their initial separation. For shrinkage to occur during sintering, the grain boundaries must be capable of both absorbing and emitting vacancies, facilitating mass transport across the interface [41]. In HyDR of oxides, additional shrinkage occurs as the volume of the compact decreases due to a reduction in neck radius, which results from the progressive removal of oxygen from the oxide lattice.

Tougas et al. [42] identified three key diffusion mechanisms during sintering of a Fe-Ni system: surface diffusion, grain boundary diffusion, and volume diffusion. At lower temperatures, surface diffusion enabled initial nickel movement along particle surfaces but

did not lead to homogenization. Grain boundary diffusion dominated up to ~1050 °C and was found to be ~30,000 times faster than volume diffusion at 900 °C. Volume diffusion became relevant above 1121 °C but remained too slow for complete Ni homogenisation within typical sintering durations (~30 min). Even at 1150 °C, Ni diffusion was limited to ~20 µm. At 950 °C, Ni stayed near its original particles, and iron self-diffusion increasingly contributed to densification as temperature rose [42]. Contrastingly, Wei et al. [12] found that interdiffusion contributed significantly to densification during pressureless sintering and HyDR of Fe- and Ni- oxides. This was because of promotion of mass transport to the sintering neck was more effective than nickel's self-diffusion. Additionally, upon further densification, open pores were annihilated, hindering the reduction of FeO_x because of the retardation of effective H_2 transport and release of H_2O [12].

In the study, substantial densification occurred during the binder-free pressureless sintering process, evidenced by marked volumetric shrinkage in the oxide pellet on a macroscopic level (Figure 9(a)) [12]. Given that oxide reduction inherently involves volume contraction, theoretical calculations revealed that over 30% of the total shrinkage was attributed to sintering-driven densification. At a global conversion rate of approximately 0.5, metallic interparticle necks began to form and expand significantly as the redox reaction progressed toward a conversion rate of around 0.85 (Figure 9(b)). This reflected the evident densification in Figure 9(a), with multiple grains detectable after full reduction.

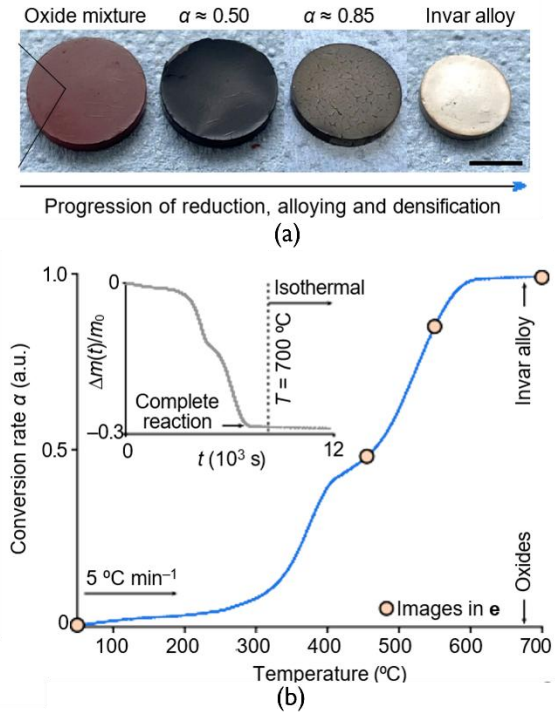

Figure 9. (a) Observable macroscopic (scale bar 5 mm) volume shrinkage at different conversion degrees during HyDR invar alloy synthesised at instances marked in a (b) TGA curve showing the reduction kinetics during the process at a heating rate of 5 °C/min [12].

This process, governed by both thermodynamic and kinetic factors, highlights the importance of the heating rate during synthesis. In Wei et al. [12], notable residual FeO_x and lower porosity was observed when using a higher heating rate of 20 °C/min. This contrasted to the successful formation of the fully invar phase and higher porosity achieved at a slower

heating rate of 5 °C/min. Sintering during 5 °C/min resulted in a refined and fine-grained microstructure, which was kept consistent at around 1.15 μm. In addition, a reduction of 17.4% to 1% in pore fraction was detected before and after sintering. This resulted in a final density equivalent to that of invar alloys fabricated by conventional melting, casting, and recrystallisation (~8.1 g/cm^3) [12].

When comparing the microstructures of alloys produced through heat treatment of wrought or worked materials versus those processed by powder metallurgy (PM), it is essential to consider the substantial influence of the initial processing routes on the final grain size and distribution. For instance, wrought materials typically undergo extensive deformation and recrystallisation, introducing a high density of dislocations that serve as effective nucleation sites for fine grains. In contrast, PM materials often start with heterogeneous structures, and the compaction and sintering steps may introduce residual porosity and promote irregular grain growth. This distinction is evident in sintered Fe–Ni systems, where nickel-rich regions can form due to the inherently low diffusivity of nickel in iron, resulting in microstructural inhomogeneities [40,42]. As a result, while austenitised wrought steels can retain grain sizes of approximately 8 μm [43].

2.4.2. Intercritical annealing

Appropriate processing parameters must be carefully selected to obtain the desired UFG duplex phase microstructure in Fe-Ni alloys. One approach to estimating the fraction of austenite retained after intercritical annealing and quenching involves evaluating its thermal stability, which is closely linked to the martensite start temperature [44–46]. De Cooman [47] developed a method based on this principle and applied it to medium-Mn steels to estimate the retained austenite fraction at room temperature (Figure 10).

Several empirical equations have been developed to predict the M_S, typically based on the equilibrium composition of the austenite phase. Notable examples include the equations developed by Steven and Haynes [48] and by Lee & Park [46], which are tailored for Fe-C-Mn-Cr-Mo-Ni and Fe-C-Mn-Si-Cr-Mo-Cu steels, respectively.

To estimate the final fraction of retained austenite, the fraction of α′-martensite ($f_{\alpha'}$) formed during cooling must also be determined. This can be calculated using the Koistinen-Marburger (KM) equation [49], which expresses the fraction of athermal martensite as a function of the temperature difference between the M_s temperature and the quenching temperature, T_Q (typically room temperature). The theoretical fraction of austenite retained (f_{RA}) at room temperature can then be calculated by subtracting the martensite fraction ($f_{\alpha'}$) from the equilibrium austenite fraction (f_γ^{eq}).

In De Cooman's study [47], the equation developed by Lee and Han [50] was applied to estimate the M_s. These values, calculated using the equilibrium composition of austenite at various intercritical annealing temperatures shown in Figure 10(b), were plotted as a function of temperature and are displayed in Figure 10(c). Thus, one can conclude that intercritical annealing at a temperature of 780 °C, results in a martensite start temperature low enough to a balanced fraction of retained austenite and ferrite at room temperature under equilibrium conditions (Figure 10 (d)).

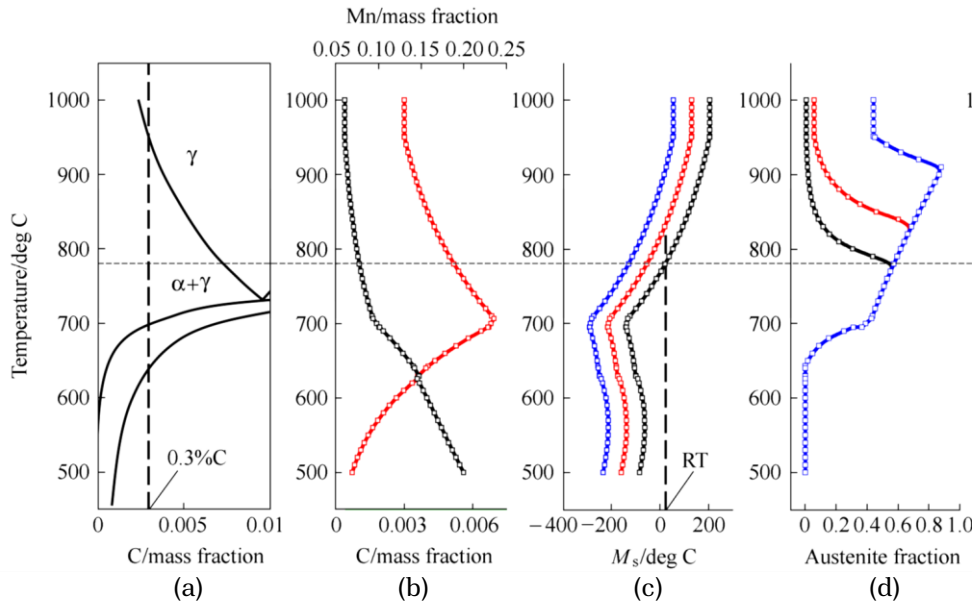

Figure 10. (a) Fe-C phase diagram and temperature against (b) carbon and manganese content in austenite phase (c) martensite start temperature and (d) austenite fraction and (e) stacking fault energy [51].

De Cooman's method provides a useful estimate for retained austenite based on equilibrium conditions, it serves only as a guideline. In practice, kinetic limitations such as limited diffusion, short holding times, and low interface mobility can hinder full stabilisation of austenite. Hence, results from this method need to be cross-referenced with experimental findings on the effect of varying intercritical annealing temperature, time, prior heating rate, and subsequent cooling parameters on the final microstructure.

2.4.3. The effect of intercritical annealing temperature and time on final microstructure

Liao et al. [52], studied the effect of different intercritical annealing processes on the microstructure and cryogenic toughness of 5%Mn-1.5%Ni low carbon steel. The materials were homogenised and subsequently hot rolled via a two-stage controlled rolling process and quenched to room temperature. After rolling, the steel plates were subjected to a two-step intercritical annealing heat treatment process. The first step included holding at 700 °C for 45 min then quenching. This was following be a second step involving reheating the steel plates to intercritical temperatures 590 °C, 620 °C, 650 °C or 680 °C for 60 min, followed by air cooling. The samples were labelled A590, A620, A650, and A680 accordingly.

With an increase in intercritical annealing temperature, the microstructure of the matrix coarsened. The X-ray diffraction (XRD) patterns in Figure 11(a), showed that all samples displayed austenitic peaks, with intensity increasing with temperature. The volume fraction of retained austenite were found to be 31.5%, 29.0%, 32.2% and 33.5% with increasing IA temperature [52].

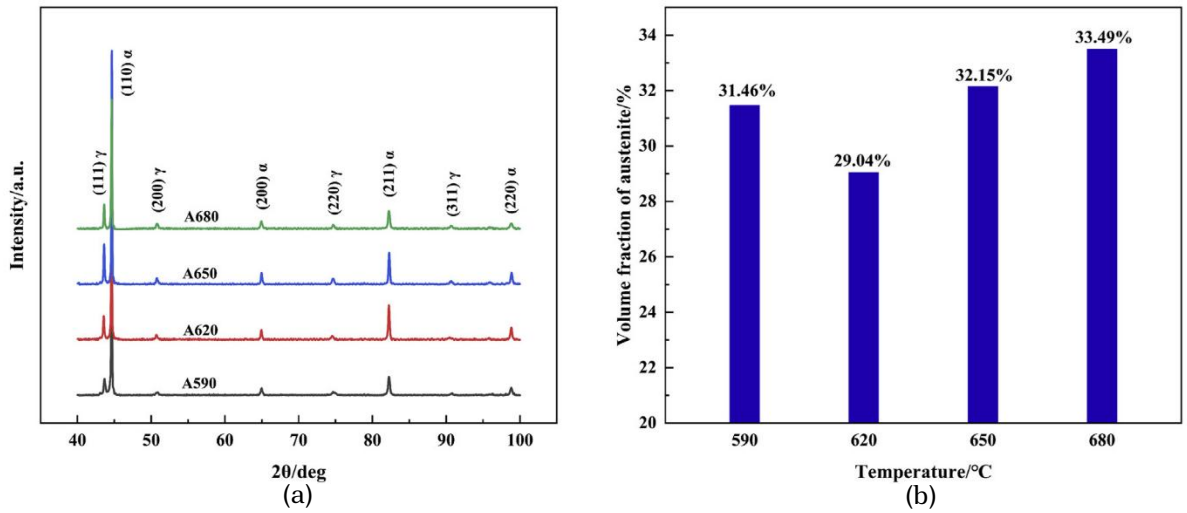

Figure 11. The (a) X-ray diffraction (XRD) spectra and (b) measured RA volume fractions of the different annealed samples [52].

Shirazi et al. [39] studied microstructural changes during intercritical annealing of a Fe-Ni-Mn martensitic steel at 600 °C for different holding times. Annealing at this temperature showed that a duplex phase (α + γ) was stable at room temperature, with the equilibrium phases consisting of 73 wt.% reversed austenite (Point O in Figure 12) [39].

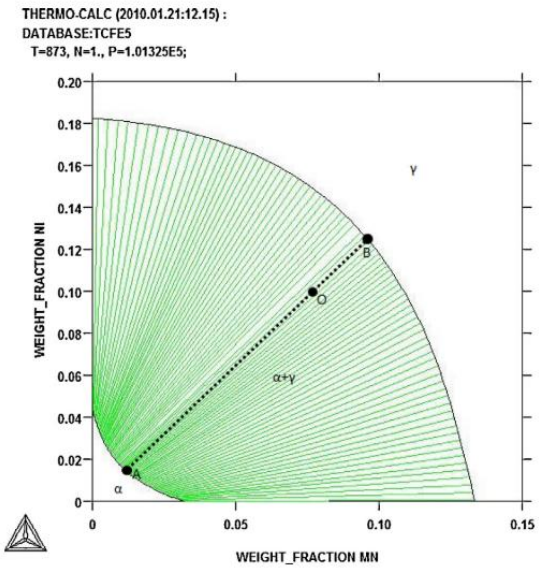

Figure 12. The phase diagram of the Fe-Ni-Mn alloy at 600 °C showing the equilibrium duplex phase [39].

Figure 13 presents optical micrographs of the solution-annealed (heated to above Ac_3) and intercritically annealed steel. Samples were heated in a salt bath at a rate of 0.8 °C/s to 600 °C and held for various durations. Figure 13(a) shows the solution-annealed steel with lath martensite substructures, providing nucleation sites for austenite, consistent with previous studies [38,39,53,54]. Figure 13(b-d) illustrates the microstructural evolution of lath martensite held for different durations in the intercritical region. After 4 minutes (Figure 13(b)), parallel austenite blocks were visible within a martensitic packet, while at 15 minutes (Figure 13(c)), the structure became more refined. Significant refinement occurred at 120 minutes, as seen in Figure 13(d), where blocks and packets were no longer distinguishable [39].

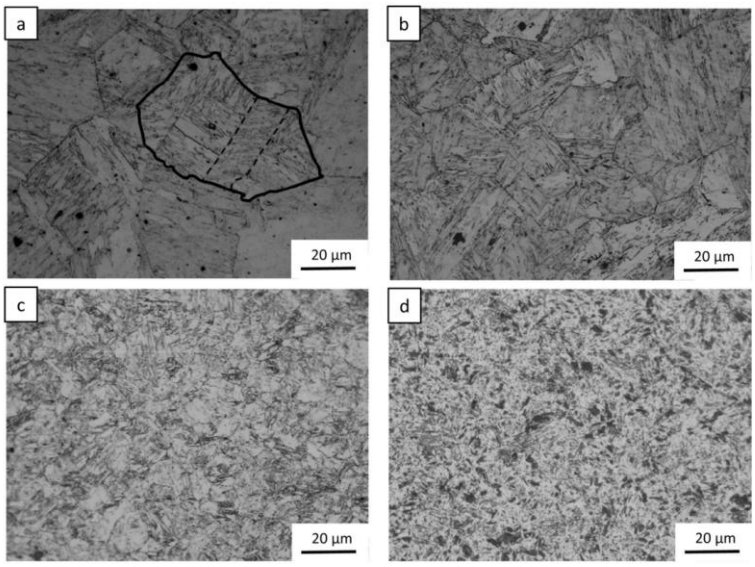

Figure 13. Optical micrographs of Fe-Ni-Mn steel (a) in solution-annealed, (b) intercritically annealed at 600 ℃ for 4 min (c) 15 min (d) 120 min [39].

XRD spectra (Figure 14) confirmed increased FCC phase volume fraction with prolonged annealing, revealing additional diffraction peaks corresponding to austenite formation. Extended annealing resulted in structural refinement, producing a fine dual-phase microstructure of martensite and austenite. The austenitic phase exhibited high thermal stability due to Ni and Mn enrichment, a behaviour also observed by Dmitrieva et al. [55], which stabilised it at room temperature. The prolonged holding time also enhanced the formation and distribution of reversed austenite, consequently improving mechanical properties of the material [39].

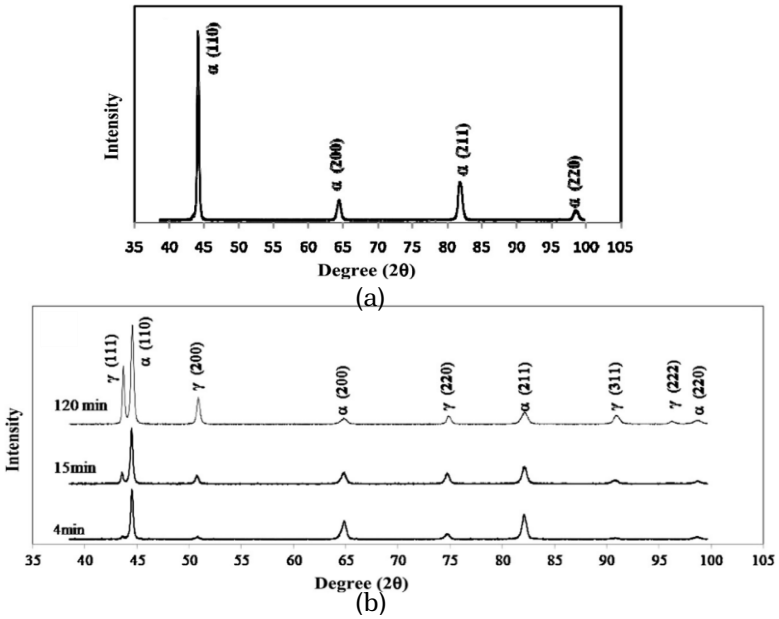

Figure 14. X-ray diffraction (XRD) spectra of Fe-Ni-Mn steel in the (a) solution-annealed (b) intercritically annealed for various holding times at 600 ℃ [39].

2.4.4. The effect of heating and cooling rates prior and after intercritical annealing on final microstructure

A study conducted by Zhang et al. [56] focused on the effect of heating rate on reversed austenite in a Fe-9Ni-C alloy prior to tempering. The heat treatment employed can be seen in Figure 15(a). Following austenitisation, the alloy was reheated using heating rates (2, 5, 10,20 and 40 °C/s) to 580 °C followed by quenching [56].

The relationship between the volume fraction of reversed austenite and the heating rate is shown in Figure 15(b) The data indicated that the volume fraction of reversed austenite increased with the heating rate, reaching a maximum of 8% at 10 °C/s. Additionally, retained austenite served as nucleation sites for subsequently formed reversed austenite. This prevented decomposition of reversed austenite during subsequent treatment, thereby increasing the final volume fraction of reversed austenite. The microstructure of the alloy formed at 10 °C/s comprised of blocky and thin film reversed austenite formed along martensitic boundaries [56].

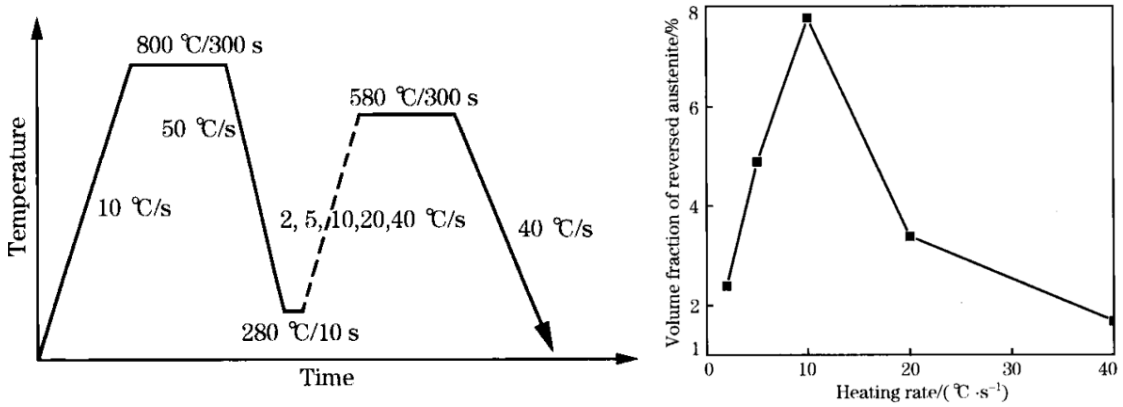

Figure 15. (a) The heat treatment applied to the Fe-9Ni-C alloys including heating to 800 °C with heating rate 10 °C/s, cooling at 50 °C/s followed by reheating at 2, 5, 10, 20 and 40 °C/s heating rates to 580 °C (b) volume fraction (%) of reversed austenite as a function of heating rate [56].

TEM images of the microstructures for samples heated at 2 °C/s and 40 °C/s are presented in Figure 16. The TEM image of the sample heated at 2 °C/s (Figure 16(a)) showed a typical lath martensitic microstructure. Substructural analysis under high magnification revealed that the martensite contained numerous dislocations, some of which appear as clusters highlighted in Figure 16(b). Some dislocations underwent slip or climb, which led to a reduction in dislocation density. The remaining dislocations rearranged into clusters, eventually forming dislocation cells. For the sample heated at 40 °C/s, martensite boundaries began to bend, and adjacent martensite structures started to collide, as illustrated in Figure 16(c, d) [56].

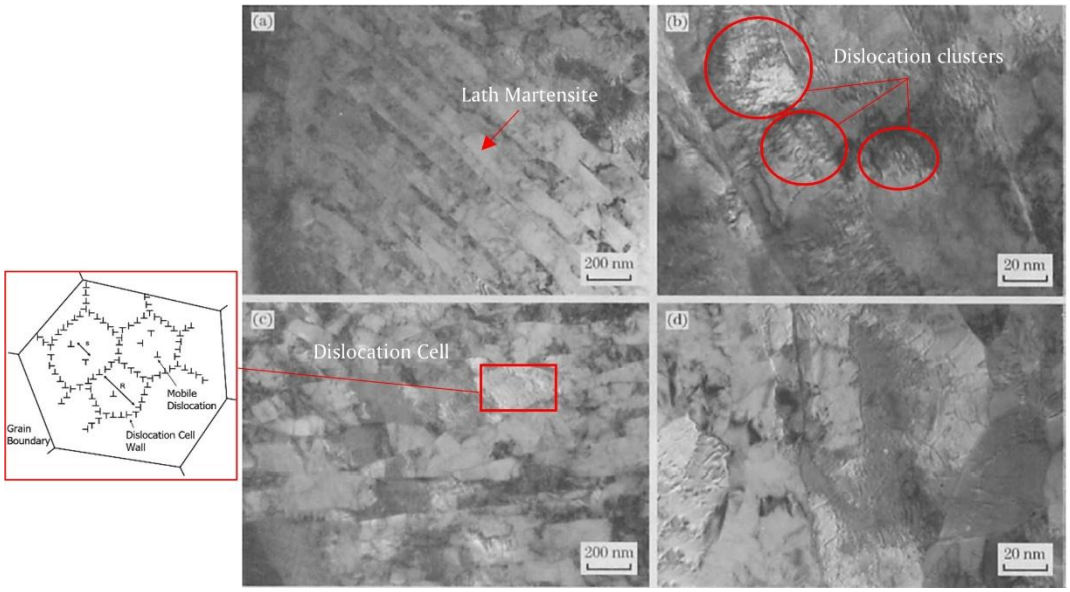

Figure 16. Bright-field transmission electron microscopy of samples heated at (a, b) 2 °C/s (c, d) 40 °C/s. [56] .

The heating rate also affected the distribution of the reversed austenite. EBSD maps (Figure 17) displayed the distribution of reversed austenite at heating rates of 2, 10, and 40 °C/s, where reversed austenite appeared in grey, the BCC matrix in white, and sub-boundaries (with angles of 10° and 5°) as grey lines. At 2 °C/s (Figure 17(a)) and 40 °C/s (Figure 17(c)), the majority of the reversed austenite was concentrated along the austenite grain boundaries and martensite packet boundaries. Contrastingly, at 10 °C/s (Figure 17(b)), reversed austenite was uniformly distributed across all types of boundaries, particularly along the martensite lath boundaries [56].

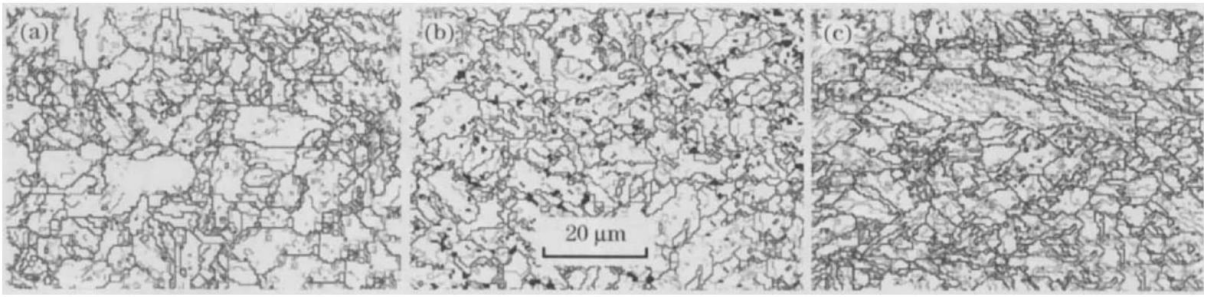

Figure 17. Electron backscattered diffraction (EBSD) maps of the distribution of reversed austenite [56].

Cai et al. [57] investigated the influence of intercritical annealing temperature and cooling rate on the stability of austenite in a medium-Mn steel. The cold-rolled sheets were heated to temperatures of 700, 750, 800, 850, and 900 °C for 5 minutes each, followed by cooling either in water or in a furnace. The water-quenching process resulted in rapid cooling rates ranging from 200 to 400 °C/s, while furnace cooling had a significantly lower rate, ranging between 0.01 and 0.43 °C/s. The SEM microstructure of water-quenched and furnace-cooled samples annealed at 700–850 °C comprised an austenitic matrix and ferrite. When the sample was water-quenched from 700 °C, it retained more of the banded structure that was present due to prior deformation compared to the furnace-cooled sample. This is because

rapid quenching prevented recrystallisation, freezing any existing microstructural features. With increasing annealing temperature, the banded structure faded, equiaxed grains became dominant, and the austenite fraction increased. At 900 °C, martensite appeared in water-quenched samples but was absent in furnace-cooled ones, indicating that rapid cooling reduced austenite stability, leading to a high-driving force for martensitic transformation. Grain size increased with annealing temperature, with furnace-cooled samples consistently showing larger grains in comparison to water-quenched samples due to longer residence times [57].

2.5. Microstructural evolution and transformation mechanisms in ultrafine-grained duplex Fe-Ni alloys

This section seeks to introduce the various microstructures that develop during phase formation and transformation processes in Fe-Ni alloys, focusing on the targeted microstructure outlined in this study. The mechanisms driving these microstructural changes are examined through the lens of both thermodynamic principles and kinetic constraints, giving insight as how factors such as composition and transformation mode influence the evolution and refinement of the microstructure.

2.5.1. Microstructural development during intercritical annealing

The initial microstructure prior to intercritical annealing strongly influences the final microstructure [52]. For example, Han et al. [58] demonstrated that starting with a martensitic microstructure and subsequently reversing it back to austenite, results in superior grain refinement and improved mechanical properties. It was observed that as the cooling rate from austenitising temperature was increased, the lath martensite size was significantly refined. This refinement in turn, facilitated the following intercritical annealing treatment by creating more austenite nucleation sites, enhancing kinetics, and promoting the formation of fine-grained ferrite and austenite structures [58]. Shirazi et al. [39] further emphasised that intercritical annealing of a prior martensitic phase is one of the most effective methods in enhancing the structural refinement whilst developing an austenite-ferrite duplex microstructure. The typical morphology of the initial, as-quenched, lath martensite in Fe-Ni alloys, has been found to be composed of hierarchical structure of packets and blocks, observed in Figure 18 [38,59,60].

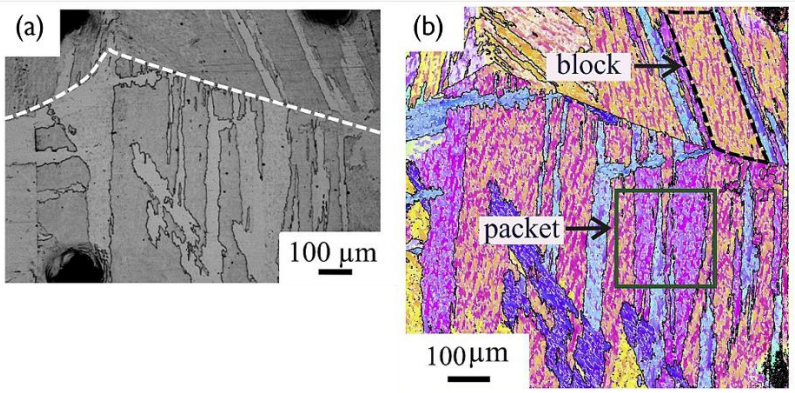

Figure 18. Initial microstructure of an Fe-18 wt.% Ni alloy, following homogenisation, austenitisation and quenching. (a) Optical micrograph displaying martensitic structure encased by prior austenite grains (white dashed lines) (b) EBSD image revealing packets and blocks of martensite [38]

The crystallographic orientation relationship (OR) between martensite and its parent austenite phase (prior austenite) is integral to the refinement of austenite formed during reversion. The transformation to martensite follows an OR close to the Kurdjumov–Sachs (K–S) OR [61], expressed as:

$$(111)_\gamma // (011)_{\alpha'}, [\bar{1}01]_\gamma // [\bar{1}\bar{1}1]_{\alpha'}$$

A single parent austenite grain can form up to 24 differently orientated martensite variants during transformation [38]. Upon reheating, each variant can independently nucleate reversed austenite, forming many smaller grains. Since these nuclei form on distinct variants, they rarely retain the original austenite orientation, effectively erasing the "memory effect". This variant multiplication increases nucleation sites and promotes grain refinement. Thus, the forward martensitic transformation and its crystallographic reversal enable the formation of a refined austenitic microstructure, a concept first introduced by d [38,39,62,63]. The concept of reversed austenite and its role in microstructural refinement was first proposed by Grange [64], through thermal cycling between martensite and austenite.

Diffusional reversion typically results in the formation of equiaxed austenite grains with low dislocation density [65]. This mechanism is more prevalent at slow heating rates, whereas increasing the heating rate significantly raises the reversion temperature. In contrast, the martensitic (displacive) mechanism of austenite reversion is generally observed at higher heating rates [38]. This process is often characterised by the appearance of surface relief, as reported in various alloy systems such as Fe-Ni [38], Fe-Ni-C [65,66] and Fe-Ni-Co [67]. In the study by Shirazi et al. [38] the reverse transformation mechanism in 11, 18 and 23 wt. % Ni Fe-Ni binary alloys were investigated. The reverse transformation temperatures observed in these alloys were notably higher than the T_0 temperature. Because rapid heating conditions (20 K/s) were applied, long range diffusion was kinetically suppressed, suggesting that both the partitionless massive and martensitic transformations were thermodynamically possible to take place.

In the studied Fe-Ni alloys, two distinct types of microstructural changes were observed during austenite reversion through in-situ imaging. The initial microstructure of the Fe-23Ni (wt.%) alloy shown in Figure 19(a), consisted of a fully martensitic structure enclosed within high angle grain boundaries (HAGB), as indicated by black arrows. Upon applying a rapid heating rate of 20 K/s, reversed austenite began to nucleate preferentially along these HAGB, as shown using white arrows in Figure 19(e). This preferential nucleation is attributed to high interfacial energy at HAGB, which lowers the thermodynamic barrier for nucleation. Additionally, the upper right prior austenite grain encased many austenite crystals which nucleated within a martensitic block, possibly at lath boundaries [39]. Austenite was acicular in shape and austenite reversion occurred rapidly, also observed in Zhang et al [54]. Subsequent EBSD, revealed a well-defined orientation relationship between the reversed austenite and the original martensite. Fe-18Ni displayed a similar austenite reversion process as Fe-23Ni. During reversion, PAGBs (example of these in Figure 18(a)), were preserved in both alloys. This effect is known as the *austenite memory effect [38,39,54,68]*. *D*espite the theoretically possibility of 24x24 martensite-austenite variant combinations during $\gamma \rightarrow \alpha' \rightarrow \gamma$ transformations, only a single austenite variant matching the original

orientation reappeared, indicating a strong orientation memory [38]. These features strongly indicate that the transformation occurred via a martensitic mechanism [62].

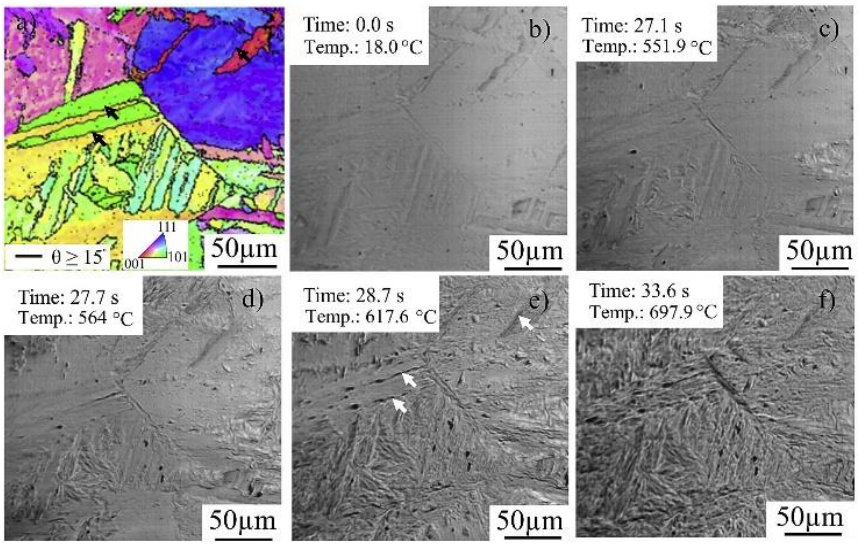

Figure 19. a) Ferrite orientation map of a Fe-23 wt.% Ni alloy before austenite reversion, where black arrows indicate high angle grain boundaries (b) - (f) In-situ confocal laser scanning microscopy (CLSM) images displaying austenite reversion during application of a 20 K/s heating rate. White arrows indicate show the nucleation of reversed austenite at HAGB [38].

In contrast, the ferrite orientation map of the initial microstructure of Fe- 11wt.% Ni, shown in Figure 20(a), displayed a lath martensitic structure with small amount of massive ferrite (encased by a red line). Microstructural evolution of this alloy (Figure 20(b)-(e)) revealed reversed austenite formation along HAGB, at the interface between massive ferrite and initial martensite. The reverse transformation of austenite proceeded by the migration of a relatively smooth interface as shown by the arrows in Figure 20(d). No specific orientation relationship between the initial martensite and reversely formed austenite was detected. The absence of a defined OR implies a lack of lattice correspondence, and thus, martensitic mechanism was not possible. In addition, PAGB were not retained throughout reversion [38]. Several characteristics of massive phases, were observed during the reverse transformation in Fe-11Ni, including irregular interface morphology [42,49,54,58]. Based on these observations, the reverse transformation in this alloy can be classified as a massive transformation.

In Fe–18Ni and Fe–23Ni alloys, quenching after austenite reversion produced martensite that retained the orientation and grain size of the parent austenite. High dislocation density led to recrystallisation, resulting in ultrafine martensitic grains, these microstructural changes are shown in Figure 21(a). In contrast, Fe-11Ni underwent a massive transformation, forming fine-grained austenite without orientation memory and yielding a coarse, blocky martensitic structure upon quenching (Figure 21(b)). Reversed austenite was not retained at room temperature in any of the compositions studied, likely due to insufficient Ni content to stabilise austenite below the M_s temperature [47,65,69]. In cases where Ni content is sufficiently high to stabilise austenite at room temperature, the final microstructure would consist of a mixture of acicular shaped reversed or recrystallised austenite, shown in Figure 21 for compositions x_{Ni_2} [54].

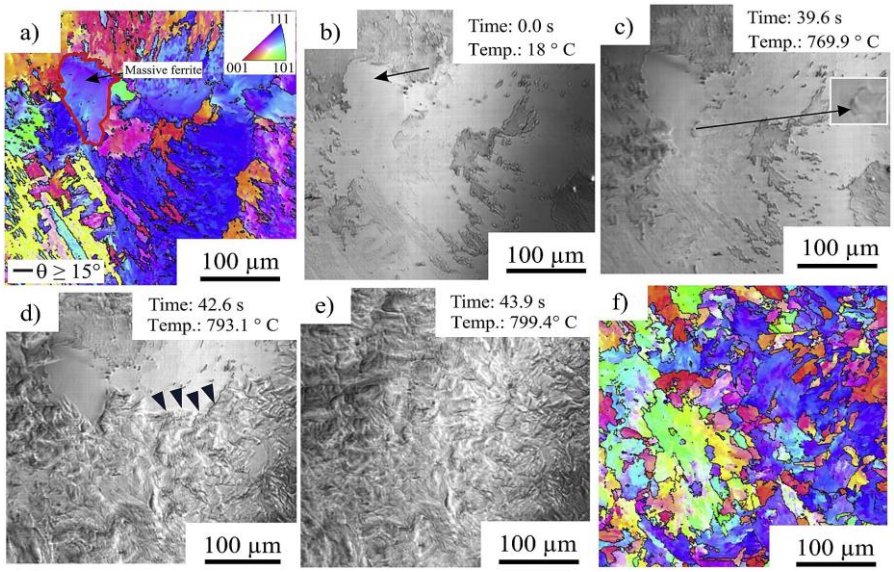

Figure 20. In-situ observations of Fe-11 wt.% Ni alloy. a) ferrite orientation map of initial, as-quenched microstructure, (b) - (e) in-situ CLSM images during heating at 20K/s d) ferrite orientation map after reversion and quenching to room temperature [38].

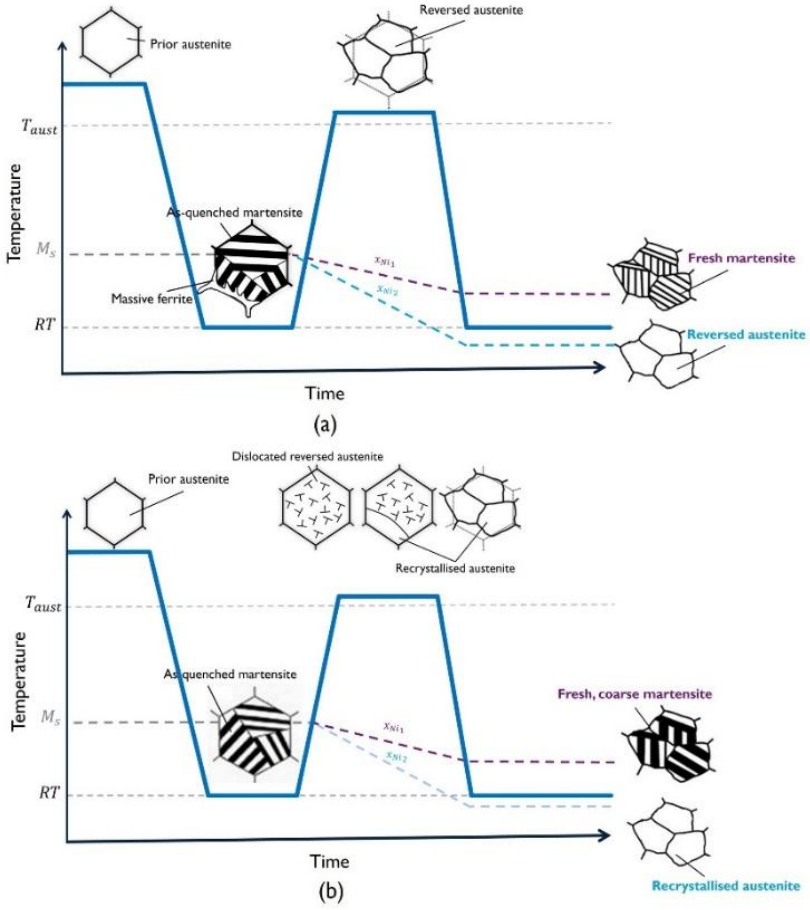

Figure 21. Schematics of resulting microstructures during each heat treatment step for the produced (a) Fe–18Ni and Fe–23Ni alloys (b) Fe–11Ni alloys in Shirazi et al. [38]. x_{Ni_1} denotes compositions where austenite is not retained at room temperature, while x_{Ni_2} corresponds to compositions sufficiently high in Ni to retain austenite phase at room temperature in the final microstructure.

2.5.2. Thermodynamic and kinetic considerations behind mechanisms governing ultrafine-grained duplex structure formation

At low Ni concentrations, Fe-Ni binary alloys[1] can exhibit a duplex phase microstructure consisting of both α and γ phases [70]. This microstructure can be achieved by applying an isothermal heat treatment within the intercritical region, shown in Figure 22. During this process, elemental partitioning of Ni between the α and γ phases occurs across the α/γ interface and is driven by the condition of equal chemical potentials, $\mu_{Ni}^{\alpha} = \mu_{Ni}^{\gamma}$. At equilibrium, the chemical potential of each component must be identical in all coexisting phases, driving the redistribution of elements until this condition is satisfied. Consequently, the lowest possible Gibbs free energy of the system is achieved. This results in Ni-rich austenite and Ni-lean ferrite, with equilibrium compositions defined by the tie line at the annealing temperature, as illustrated for a Fe- 10 wt.% Ni alloy in Figure 22 [18,71].

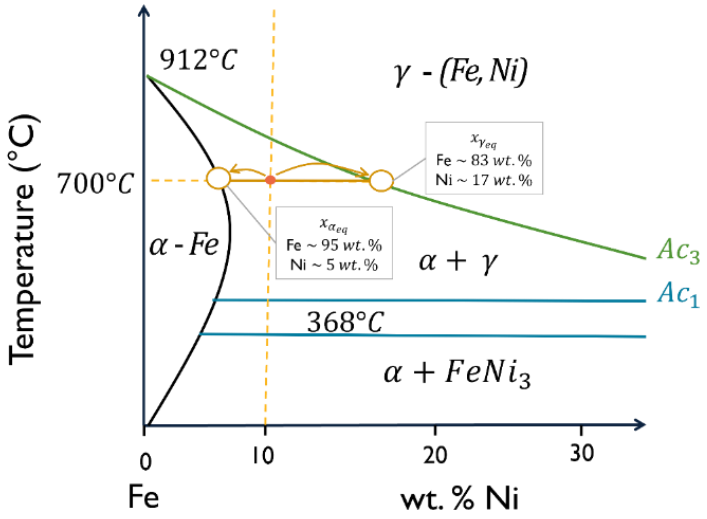

Figure 22. Fe-Ni phase diagram for low Ni concentrations (in wt.%). The diagram illustrates the equilibrium phase (α + γ) composition at 700 °C for an alloy with a nominal composition of Fe- 10 wt.% Ni, as indicated by the tie line. Created using data extracted from the TCFE13 database in Thermo-Calc (2024b).

While thermodynamic equilibrium defines the final phase compositions, kinetics governs how fast and how completely this duplex phase forms [71]. In particular, the growth rate of the γ-phase (FCC) within a α-matrix (BCC) for Fe-Ni binary system, is dictated by two kinetic factors: the diffusion coefficient of nickel in α (D_{Ni}^{α}), and the mobility of the α/γ interface [58,71]. At temperatures between A_{e1} and A_{e3}, two kinetic regimes can be considered under the assumption of local equilibrium at the interface. In diffusion-controlled transformations, the rate-limiting step is the slow bulk diffusion of Ni in ferrite. In contrast, interface-controlled transformations are limited by the low mobility of the phase boundary itself. In most practical cases, both mechanisms operate simultaneously and jointly determine the overall transformation rate [18,72].

[1] From this point onward, 'low-nickel' Fe–Ni alloys refer to compositions containing between (5 - 30 wt.%) Ni, in line with common usage in research on these alloy systems.

To account for these effects, a distinction is made between intrinsic interface mobility (M_{int}) and the effective interface mobility (M_{eff}). The intrinsic mobility reflects the interface's inherent ability to migrate, governed solely by lattice rearrangement and associated Gibbs energy dissipation. In contrast, the effective mobility accounts for additional dissipative processes that hinder interface motion due to an increase in activation energy across it [53], more applicable to most practical cases. These barriers arise from various atomic-scale factors including interfacial energy, lattice misfit, coherency strains, dislocation content, and compositional differences. The total interfacial energy of phase boundaries (γ_{PB}) consists of both atomic disorder (γ_d) and compositional differences (γ_c). Here γ_d arises from atomic misalignment at the boundary, while γ_c stems from chemical mismatch between adjacent phases [18,72].

Simulations by Zhu et al. [53] revealed that the effective interface mobility, as inferred from overall transformation kinetics in Fe-Ni systems, is significantly reduced at lower temperatures (Figure 23). This low interface mobility arises from its Arrhenius-type dependence on temperature, where the energy barrier for interface migration becomes increasingly difficult to overcome as the temperature decreases. Simultaneously, Ni exhibits particularly low diffusivity in the BCC (ferrite) phase of Fe-Ni alloys, with a bulk interdiffusion coefficient of approximately 5.91×10^{-21} m^2/s at 600 ℃. This value is significantly lower than typical diffusivities observed for other elements in this BCC system, by at least one to two orders of magnitude. For example, the diffusion coefficient of Mn in BCC Fe is $D_{Mn} \approx 1.46 \times 10^{-20}$ m^2/s at 600 ℃. It should be noted that these diffusion coefficients reflect the volume diffusion and do not account for potentially faster diffusion paths through grain boundaries or dislocation cores [73,74]. Nevertheless, the inherently low diffusivity of Ni in the BCC matrix leads to slow redistribution of Ni during phase transformations, particularly under short isothermal holding period or rapid thermal cycles.

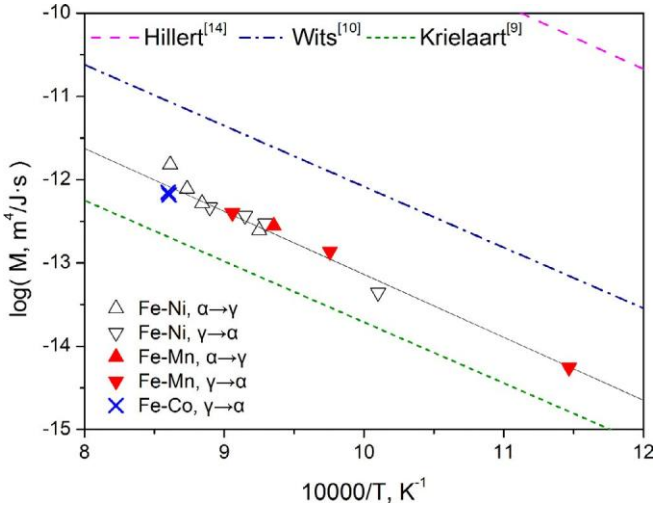

Figure 23. Interface mobility as a function of temperature in different Fe-X systems across an α/γ interface derived by fitting experimental findings to a Gibbs Energy Balance (GEB) model [53].

During reversion of austenite (γ) from ferrite (α), which require partitioning of Ni into austenite to satisfy thermodynamic equilibrium, the combination of slow bulk diffusion and low interface mobility strongly suppresses equilibrium growth. As a result, the γ phase tends to grow under partitionless or near-partitionless conditions, leading to compositional

invariance between product and parent phases [60,72]. This kinetic suppression of both diffusion and interface migration at temperatures lying between A_{e_1} and A_{e_3}, is consistent with the behaviour observed in massive transformations, where phase boundaries move rapidly and the transformation proceeds without maintaining equilibrium [60,75]. A massive transformation (MT) is defined as a diffusional nucleation and growth process, in which the product phase differs in crystal structure but retains the same composition as the matrix. At low undercoolings below the T_0 temperature, nucleation at grain boundaries requires high coherency with both adjacent grains, especially in two-phase regions as observed in Fe-Ni. Growth occurs via diffusional jumps across select areas of the interface, displaying a 'massive' appearance, including large, blocky and featureless regions typically observed in micrographs [53,59,75].

Figure 24 illustrates the Gibbs free energy change at temperature T_1 for two transformation scenarios; (a) partitioning transformation and (b) partitionless transformation. In the equilibrium case, sufficient diffusion allows full partitioning of Ni, and the two-phase α + γ state is defined by the common tangent construction yielding a greater overall free energy reduction. In contrast, the constrained case, representative of a massive transformation in Fe-Ni alloys, occurs with limited diffusion, resulting in α and γ phases of nearly identical composition to the parent alloy. This leads to a higher (local) free energy minimum rather than the global minimum achieved in full partitioning, typical during austenite reversion at temperatures within the intercritical region [53,75].

Depending on the chemical composition and heat treatment, austenite reversion can proceed via two primary mechanisms (i) a thermally activated diffusional process and (ii) an athermal displacive or martensitic process [38]. Martensitic transformation becomes thermodynamically favourable when the temperature falls below the T_0 temperature, at which the Gibbs free energy of martensite becomes equal to or lower than that of austenite at the same composition. However, the transformation typically initiates at a lower temperature (< M_s) due to the need to overcome the activation barrier for shear deformation [62,72]. In Fe–Ni binary systems, the martensitic phase forms with nearly ideal BCC symmetry (c/a ≈ 1) due to the absence of interstitials like carbon, resulting in minimal tetragonality [60,76].

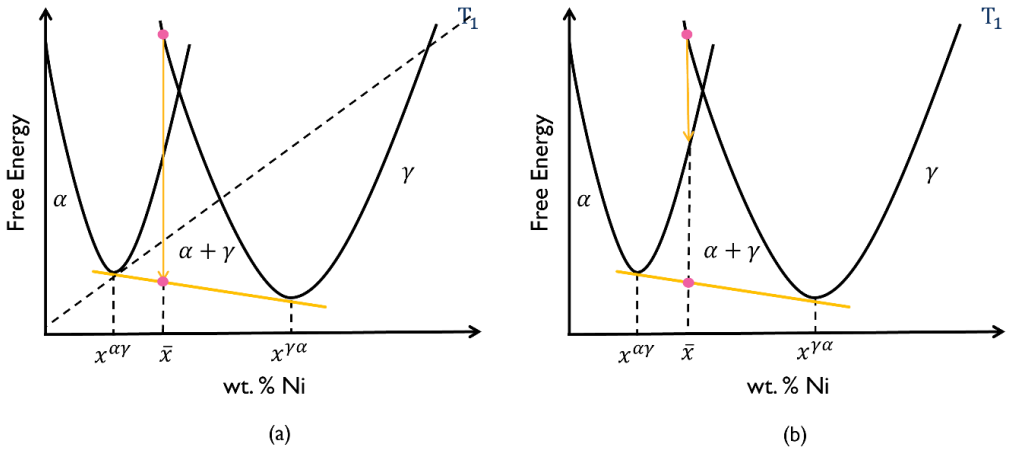

Figure 24. Gibbs free energy curves in the case of (a) an equilibrium transformation and (b) a partitionless, therefore composition invariant, transformation. Created using data extracted from the TCFE13 database in Thermo-Calc (2024b).

2.6. Research gaps identified from literature for the synthesis of Fe-Ni alloys via HyDR

Current research on hydrogen-based direct reduction of metallic oxides has primarily focused on the reduction of individual oxides, without fully integrating reduction, alloying, and thermomechanical processing into a single-step process. Wei et al. [12] successfully demonstrated the synthesis of a fully reduced, dense bulk invar alloy that retained a fully FCC phase at room temperature. However, the application of HyDR to produce a final bulk Fe-Ni alloy with a tailored microstructure has not yet been explored. Moreover, grain refinement via austenite reversion during intercritical annealing, without prior deformation, remains under-researched. At low intercritical annealing temperatures, slow diffusion kinetics and the partitionless nature of the dominant transformation mechanisms hinder the stabilisation of austenite, posing a challenge to achieve a stable duplex microstructure comprising of ferrite and austenite at room temperature. Therefore, this study aims to apply the HyDR approach to Fe-Ni oxides to obtain an ultrafine-grained duplex-phase microstructure, consisting of austenite and ferrite, through austenite reversion, addressing these gaps in the literature.

3. Materials and experimental methods

3.1. Oxide selection and pellet fabrication

The Fe-Ni binary alloys researched in this study were synthesised using Fe_2O_3 (particle size < 5 µm, Sigma-Aldrich, USA) and NiO (particle size < 35 µm, Thermo Fisher Scientific, USA) as starting materials. Both oxides had a purity greater than 99% and were used as received, without further purification. The powders were prepared to target an Fe-10Ni composition by weight[2], chosen based on prior literature [12,77] and does not represent an optimised or application-specific ratio. Thermodynamic predictions were later used to inform the selection of Fe-17Ni, which was prepared in a similar manner to the former Fe-Ni composition.

The powder mixtures were ball-milled to achieve a homogeneous mixture and break down oxide particles into smaller sizes, thereby promoting full reduction. High-energy ball-milling was performed using a Retsch's (Germany) planetary milling machine at 200 rpm, employing a 250 ml hardened steel grinding jar and balls, with a ball-to-powder ratio of 5:1. Milling was consisted of a continuous single 16-hour run with 30-minute intervals, totalling 8 hours of effective mixing. The as-milled powders were compacted into individual cylindrical green bodies, as shown in Figure 25, using a graphite die and a uniaxial press at room temperature. A consistent compaction force of 5 tonnes (64 MPa) was applied for a holding time of 30 minutes. The resulting pellets were approximately 10 mm in diameter, with heights ranging from 1 to 3 mm (measurement locations shown in Figure 25). The mass of the pellets ranged between 400 to 600 mg, taking in consideration the maximum change in mass loss that can be recorded during thermogravimetric analysis.

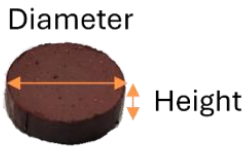

Figure 25. Measurement locations of the cylindrical green-body pellet.

3.2. Material synthesis

The samples were synthesised in a horizontal tube furnace (resistance heating) under a reducing atmosphere of 100% hydrogen gas with a purity exceeding 99%. The hydrogen was supplied at a controlled flow rate of 250 mL/min throughout the heat treatment process. Three sets of samples, description given in Table 2, were prepared using the thermal profile shown in Figure 26.

[2] All compositions in wt.% unless specified

Table 2. Sample naming convention adopted throughout the study. Each term in the naming format represents: F – furnace, x – composition, T – temperature, β_1 – heating rate during reduction, β_2 – heating rate during intercritical annealing. Each sample is represented by [F_β_1/β_2_x_T].

Set	F	x (wt.%)	Sample	T (°C)	β_1 (°C/min)	β_2 (°C/min)
Set 1	TGA	Fe-10Ni	**TGA_10/5_10Ni_620**	620	10	5
			TGA_10/5_10Ni_590	590		
			TGA_10/5_10Ni_560	560		
Ref	TGA	Fe-10Ni	**TGA_5_10Ni_RSS900**[1]	900	5	N/A
Set 2	TF	Fe-10Ni	**TF_5/5_10Ni_620**	620	5	5
			TF_5/5_10Ni_590	590		
			TF_5/5_10Ni_560	560		
Set 3	TF	Fe-17Ni	**TF_5/20_17Ni_560**	560	5	20
			TF_5/20_17Ni_490	490		
			TF_5/20_17Ni_460	460		

[1]*Reference sample, subjected to only step 1 of the heat treatment (Figure 26).*

Step 1 of the heat treatment, shown in Figure 26, involved heating the samples from room temperature at a selected heating rate of either 5 °C/min (set 1) or 10 °C/min (sets 2, 3) to 900 °C. This step was designed to simultaneously promote both the reduction of the oxide phases and densification of the material. The samples were held at 900 °C for 0.5 hours, then cooled to room temperature in oil to form a martensitic phase at room temperature. The cooling rate following step 1 depended on the furnace type (thermogravimetric analyser (TGA) or Tube furnace (TF)) and was limited by the furnace's safety rating for rapid cooling in a hydrogen atmosphere. Step 2, aimed at microstructural control through intercritical annealing, was applied immediately afterward. Heating rates during this step were 5 °C/min for sets 1 and 2, and 20 °C/min for set 3. The target intercritical annealing temperatures were 560 °C, 590 °C, and 620 °C for sets 1 and 2, and 460 °C, 490 °C, and 560 °C for set 3. The samples were held at the target annealing temperature for 1 hour (sets 1 and 2) or 6 hours (set 3), followed oil quenching to retain the resulting microstructure.

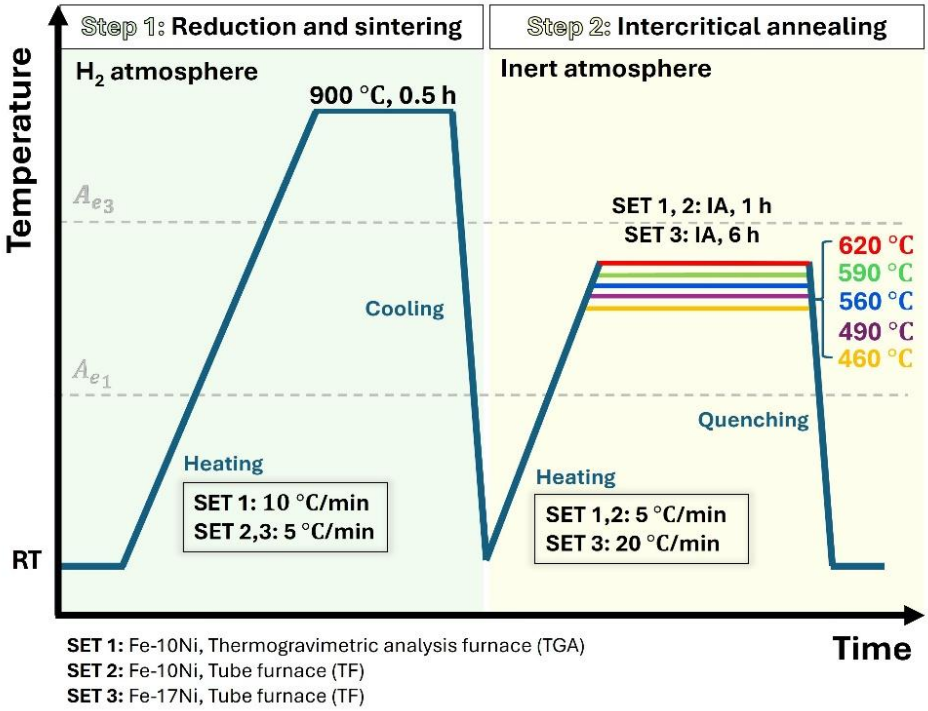

Figure 26. The designed heat treatment comprising of step 1 (reduction and sintering) and step 2 (intercritical annealing for microstructural control) for the synthesis of Fe-Ni alloys. Texts give the (i) stages along the heat treatment (dark blue), (ii) the parameters for different sample sets (black) and (iii) the selected intercritical annealing (IA) temperatures (red 620 °C, green 590 °C, blue 560 °C, violet 490 °C, yellow 460 °C)

3.3. Reduction behaviour and degree of densification

To study the reduction behaviour of the samples, TGA was performed using a thermogravimetric analyser from SETARAM (France), equipped with a resistance heating furnace and thermal balance for precise mass measurement with a resolution of 0.01 μg. The same heat treatment shown in Figure 26 was applied, except that the cooling rates after each heating stage were limited by the equipment's intrinsic cooling rate (~20 °C/min). During the TGA process, a mixed gas atmosphere of hydrogen (83.3%) and argon (16.7%) was employed, in accordance with the instrument's maximum allowable hydrogen amount. These conditions were held constant throughout the analysis, with a total gas flow rate of 180 mL/min. To prevent mass loss due to handling, the alumina crucible was weighed separately, and its mass was later subtracted from the combined weight of the crucible and the pelletised blended oxide powder. Mass measurements were carried out using a precision balance with an accuracy of $\pm$0.001 g. The crucible was mounted into TGA where the instantaneous mass of the pellet was continuously recorded during the test. The data was processed and allowed for the calculation of the reduction degree using equation(m.1).

$$R(t) = \frac{m(t) - m_0}{m_\infty - m_0} \tag{m.1}$$

Here, $m(t)$ is the instantaneous mass, m_0 the initial mass, and m_∞ is the theoretical mass after complete reduction, estimated assuming full reduction of $Fe_2O_3 \rightarrow Fe$ and $NiO \rightarrow Ni$ across the pellet. Theoretical mass values were calculated based on the molar ratios corresponding to the target compositions.

3.4. Sample preparation, microstructural analysis and characterisation

Samples were sectioned parallel to their height (Figure 27) using an Al_2O_3 (Struers, Denmark) cutting disk at 3000 rpm and 0.100 mm/s. This was done to expose the cross-section, enabling microstructural examination from the core to the outer surface of the cylindrical specimens. Following this step, the samples were mounted in conductive resin at 180 ℃ and 250 mbar (Struers, Denmark). Standard metallographic preparation procedures outlined in ASTM E3-11 [78] were followed. Samples from sets 1 and 2 were initially ground from P180 to P2500 using SiC paper, then polished using 3 µm and 1 µm diamond suspensions, and finally with a 0.25 µm oxide polishing suspension (OPS, colloidal silica) (all from Struers, Denmark) for SEM analysis. This sample preparation procedure was also applied to one half of the samples in set 3 for EBSD characterisation, while the other half was etched using 2% nitric acid for approximately 20 s to enable backscattered electron (BSE) imaging. All samples were ultrasonically cleaned in ethanol for around one hour, followed by air drying and degassing in preparation for microstructural characterisation. Prepared samples were stored in a desiccator until use.

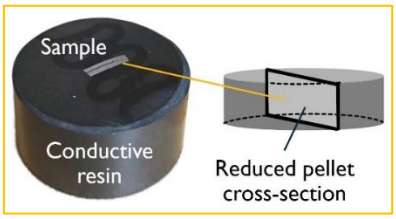

Figure 27. Schematic showing the cross-section of the reduced Fe-Ni alloy embedded in conductive resin. The highlight region indicates the area sectioned for microstructural and compositional analysis.

Microstructural characterisation, including imaging (all sets), as well as energy dispersive X-ray spectroscopy (EDX) and EBSD (set 3 only), was carried out using a JEOL scanning electron microscope (Japan) equipped with detectors from Oxford Instruments (United Kingdom). SEM-BSE imaging was performed at an accelerating voltage of 10 kV at a working distance of 10 mm, and a using a probe current of 4 nA. For set 3, imaging was conducted on etched samples. EDX was used to obtain compositional information over areas, lines, and points on polished samples from set 3. EDX analysis was performed using a silicon drift detector (Oxford Instruments, United Kingdom) at an accelerating voltage of 20 kV, a working distance of 9.1 mm, with an acquisition time of approximately 60 seconds and scan areas of 12.8×9.6 µm at ×10,000 magnification. EBSD was conducted on the same polished samples from set 3, using an accelerating voltage of 15 kV, probe current of 4 nA, a working distance of 8.5 mm, a step size of 0.1 µm, and scan areas of 64×48 µm at ×2000 magnification. Data points with a confidence index below 0.1 were excluded from the analysis to ensure reliable orientation measurements.

Phase analysis was carried out using a D8 Advance X-ray Diffractometer (Bruker, USA) in Bragg Brentano geometry equipped with Co K_α radiation source (λ_{Co,K_α}= 1.78897 Å) to minimise fluorescence from iron. XRD patterns were collected over a 2θ range of 30° to 130°, with a step size of 0.05° and a counting time of 2 s per step. Data evaluation was performed using DiffracSuite.Eva and Profex software with phase fractions obtained through Rietveld refinement showing a model fitting error of ±0.002 wt.%. Signal smoothening and baseline subtraction were carried out using Origin.

3.4.1. Determination of grain size and pore fraction

Grain size measurements were carried out using Heyn's Lineal Intercept Method (LIM) in accordance with ASTM E112-24 [79]. Measurements were performed on ImageJ on the SEM images, acquired at a magnification of ×1300 for sets 1 and 2 and ×2000 for set 3. Multiple parallel straight test lines of equal length were drawn on each micrograph to ensure representative sampling. To satisfy the ASTM requirement of atleast 50 grain boundary intercepts per micrograph, five test lines were used per image. Grain boundary intersections were classified and counted as follows: endpoints lying exactly on grain boundaries (EoGB) were counted as 0.5 intersections, whole section grain boundary intersections (WS), including tangential intersections, as 1, and triple-point intersections (TP) as 1.5. This classification method is illustrated in Figure 28, where EoGB, WS and TP intersections are marked with cyan, red, and green dots, respectively.

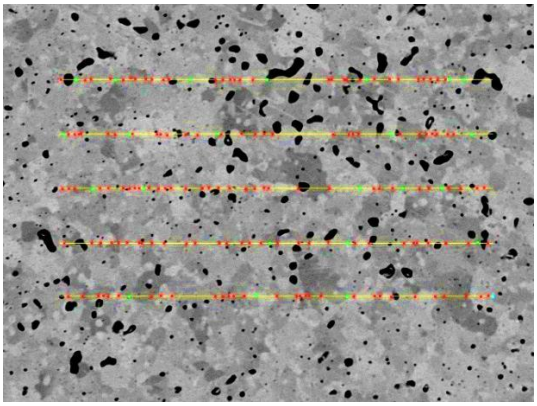

Figure 28. An example of the LIM applied to a section across a sample to obtain the average grain size in microns. Cyan, red and green dots represent the number of intersections with the end of grain boundaries (EoGB), whole sections (WS) and triple points (TP), respectively.

The total number of grain boundary intersections (P_i) for each individual test line, i, (where i = 1, 2, ..., n) was determined using equation(m.2).

$$P_i = 0.5 \cdot EoGB_i + 1 \cdot WS_i + 1.5 \cdot TP_i \tag{m.2}$$

This was followed by obtaining the intercept density for each line using equation(m.3).

$$\bar{P}_{L_i} = \frac{P_i}{y} \tag{m.3}$$

where, y is the length of each line in microns.

The corresponding mean intercept length for each line was obtained using equation (m.4). For each micrograph, with n = 5 test lines, the average intercept length was calculated.

$$\bar{l}_i = \frac{1}{\bar{P}_{L_i}} \tag{m.4}$$

To estimate the error associated with the measurements, the standard deviation of the intercept lengths across the test lines within each micrograph was calculated. To quantify the uncertainty in the grain size measurement and to statistically express the reliability of the estimated mean, a 95% confidence interval (CI) was computed for each micrograph. This was based on the t-distribution corresponding to n - 1 degrees of freedom. For n = 5, a typical value of $t_{(0.975,\ 4)}$= 2.776 was used. The final grain size for each micrograph was therefore reported as $\bar{l}_{micrograph} \pm CI_{95\%}$.

Pore analysis was carried out using the ImageJ software. First, the SEM images were converted to 8-bit grayscale format followed by the application of a thresholding technique to isolate the pores from the background, as shown in Figure 29. The 'Analyze Particles' tool was then used to measure and quantify pore parameters, including pore size (μm), circularity (1 being most circular), connectivity (%) and volume fraction (%). This analysis was conducted to assess whether the pores originated from (i) oxygen removal during reduction or (ii) insufficient sintering.

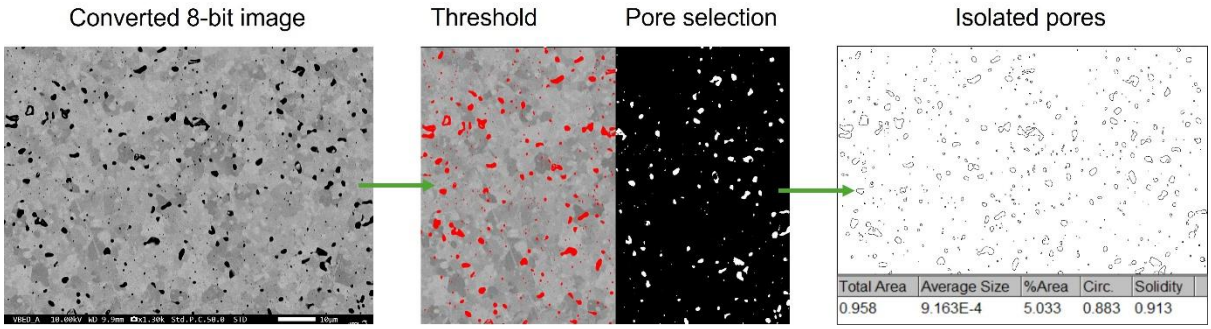

Figure 29. Method used to determine the pore fraction across each sample.

3.5. Thermodynamic predictions of phase fractions

The method provided by De Cooman [47] was used to thermodynamically predict the phase fractions of ferrite, fresh martensite, and reversed austenite in a Fe-Ni binary system. A combination of empirical modelling and thermodynamic simulation was employed for this purpose. This calculation procedure was applied to the initial Fe-10Ni composition to estimate the expected final phase constitution as a function of the chosen intercritical annealing temperature. Furthermore, this was applied across varying nickel contents (between 11 – 30 wt.% Ni, classified as low nickel) and intercritical annealing temperatures. This along with experimental results obtain throughout this study was used to inform the selection of Fe-17Ni.

To derive an accurate equation for the martensite start temperature (M_s) for a Fe-Ni binary system, linear regression was applied to an experimental data set published by Kaufman and Cohen [63]. The general form of the regression model is shown in equation(m.5):

$$M_s = k_0 + k_1 x_{Ni} \tag{m.5}$$

Where, k_1 is the constant representing the rate at which M_s changes with Ni content, and k_0 is the M_s at 0 wt.% Ni. Here, x_{Ni} is the nickel content (in wt.%).

Equations (m.6) and (m.7) define the constants k_1 and k_0, respectively, based on the linear regression method. Here, n denotes the number of experimental data points.

$$k_1 = \frac{\left(n\sum\left(x_{Ni_r} M_{s_r}\right) - \sum x_{Ni_r} \sum M_{s_r}\right)}{n\sum\left(x_{Ni_r}^2\right) - \left(\sum x_{Ni_r}\right)^2} \tag{m.6}$$

$$k_0 = \frac{\left(\sum M_{s_r} - k_1 \sum x_{Ni_r}\right)}{n} \tag{m.7}$$

Where x_{Ni_r} represents the Ni content (in wt.%) at the r-th data point, and M_{s_r} is the experimentally measured martensite start temperature corresponding to that composition. These values vary across the dataset and are used to perform the regression analysis.

The resulting equation, presented in equation(m.8), showed a high degree of statistical accuracy, with an R^2 value of 0.9944. The quality of the fit is illustrated in Figure 30.

$$M_s\ (℃) = 762.88 + \ -27.41 \cdot x_{Ni}(wt.\%) \tag{m.8}$$

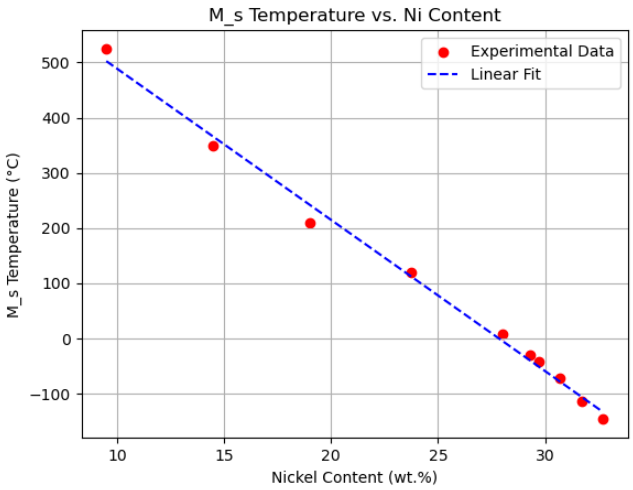

Figure 30. Linear regression applied to experimental data for a Fe-Ni binary system.

Thermodynamic calculations were performed using the TCFE13 database in Thermo-Calc (2024b) to simulate phase equilibria over a temperature range of 25-1000 ℃. From these simulations, the volume fractions of ferrite and austenite were obtained, along with the nickel content in the austenite phase at each temperature. The concentration values of nickel in austenite (wt.%) were used to determine the M_s temperatures for various the varying composition of austenite as a function of intercritical annealing temperature using equation(m.8). The volume fraction of fresh martensite ($f_{\alpha'}$) formed due to insufficient stabilisation of the austenitic phase during quenching, was estimated using the Koistinen-Marburger (KM) equation quoted in equation(m.9) [49],

$$f_{\alpha'} = (1 - exp(-\alpha \cdot (M_s - T_Q))) \tag{m.9}$$

where, α is a material-dependent coefficient (taken as 0.011), and T_Q is the quenching temperature, assigned to room temperature (25 ℃). Since holding in the intercritical region $(A_{e_1}<T_1 < A_{e_3})$ results in the formation of a duplex phase of austenite and ferrite, the calculated fresh martensite fraction was multiplied by the volume fraction of prior austenite (f_γ). Finally, the volume fraction of reversed austenite ($f_{\gamma_{RA}}$) was calculated using equation (21).

$$f_{\gamma_{RA}} = f_\gamma - f_{\alpha'} \tag{m.10}$$

However, this method has certain limitations when applied to practical scenarios. It assumes an infinitely fast heating rate to the intercritical region and that the system reaches full equilibrium during annealing. In reality, heating rates are finite, and phase transformations are governed by kinetic factors such as diffusion rates and interface mobility. In cases that the M_s temperature is below room temperature, the fraction of fresh martensite in the final microstructure equates to 0. The final microstructure will then consist of the duplex phase ferrite and austenite.

4. Results

The objectives in this study include achieving near-complete reduction of mixed Fe–Ni oxides, controlling densification during sintering, and promoting the formation of stable, ultrafine duplex phase assemblies through optimised intercritical annealing. The following section presents the experimental findings related to reduction behaviour, densification, phase constitution, and microstructural characteristics of the produced alloys.

4.1. Degree of reduction and densification

Thermogravimetric analysis was carried out to assess the initially chosen heat treatment parameters and to optimise them for complete reduction and high densification. For samples in set 1, the relative mass loss, the rate of relative mass loss, and the reduction degrees during step 1 in Figure 26 (including reduction and sintering) were recorded and calculated. For sample TGA_5_10Ni_RSS900, only the reduction degree is shown graphically. Additionally, pore analysis was conducted to determine the degree of sintering under the applied processing conditions. These results enable comparison and discussion of the extent of reduction, densification and their interactions.

TGA results for samples in set 1 are shown in Figure 31 (a - c). All samples displayed similar mass loss trajectories, as depicted in Figure 31(a). At the end of the reduction step (values provided in Table 3), reference sample, TGA_5_10Ni_RSS900, exhibited the highest relative mass loss, followed by TGA_10/5_10Ni_590. Figure 31(b) reveals comparable peak patterns across all samples, with distinct regions of mass loss rates, suggesting a stepwise reduction process driven by varying thermodynamic driving forces. The progression of reduction degree over time is shown in Figure 31(c). As noted in Table 3, TGA_10/5_10Ni_590 readily achieved complete reduction, completing the process at approximately 5800 s. In contrast, TGA_10/5_10Ni_620 and TGA_10/5_10Ni_560 reached final reduction degrees of 0.996 and 0.995 at around 6200 s and 7300 s, respectively. The extended reduction time beyond 7050 s, the end of the isothermal segment in step 1 (Figure 26), confirms that reduction in TGA_10/5_10Ni_560 continued during cooling. This is undesirable, as completing the reduction before the onset of cooling is essential for achieving greater control over reduction and densification process. It is also important to note that, because the samples in set 1 underwent the complete heat treatment (step 1 and 2 in Figure 26), the final mass may not exclusively reflect reduction-related mass loss during step 1. This may also include additional mass loss that occurred in step 2.

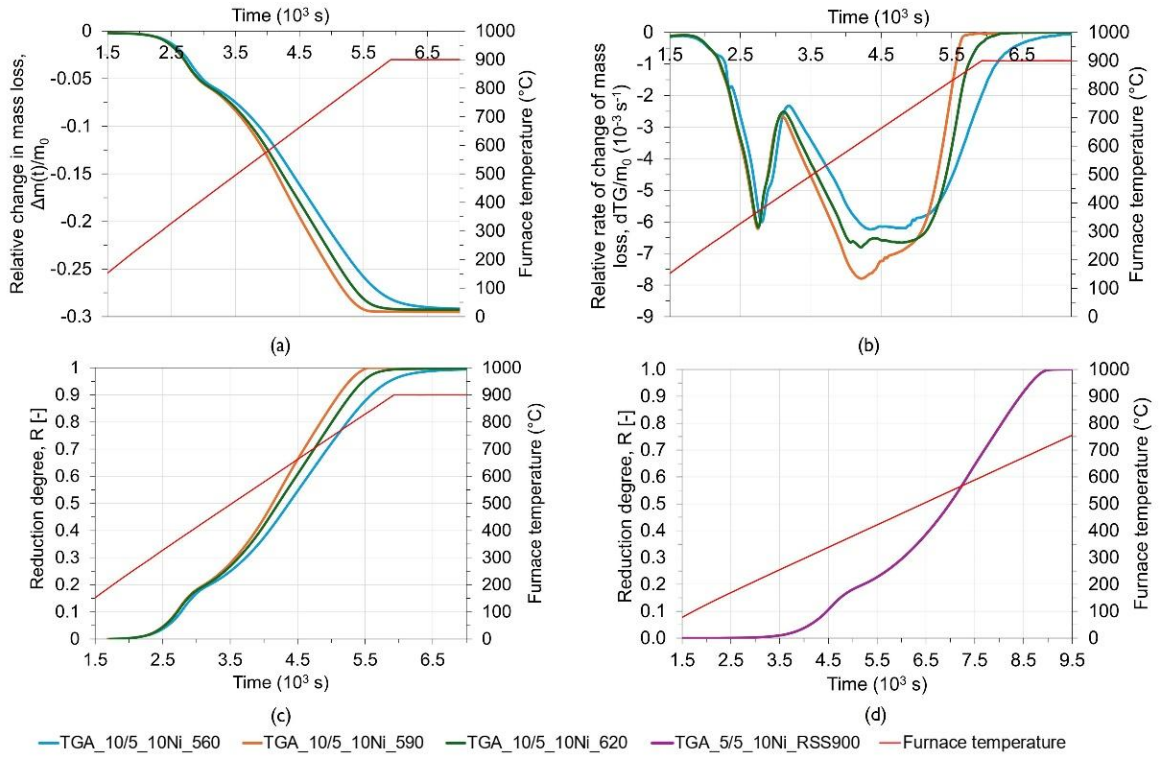

Figure 31. (a) Relative change in mass loss, $\Delta m(r)/m_0$, (b) rate of relative mass loss, $\Delta m(r)/m_0 \Delta t$, (10^{-3} s^{-1}) and (c) reduction degree (R) of set 1 samples and (d) of TGA_5_10Ni_RSS900 as a function of time, t, (10^3 s).

Since TGA_10/5_10Ni_560 exhibited continued reduction during cooling, sample TGA_5_10Ni_RSS900 was subjected to a slower heating rate of 5 °C/min to ensure complete reduction during production in the tube furnace. Under these conditions, the sample exhibited a relative mass loss of 0.2936 and achieved a reduction degree of 1 ± 0.002 (Figure 31(d) and Table 3), indicating complete reduction. The reduction trajectory closely resembled those of samples in set 1. In this case, complete reduction was achieved at 10,407 s, well before cooling commenced at 12,300 s. Given the high repeatability in mass loss trends observed in set 1, and the confirmed complete reduction in TGA_5_10Ni_RSS900, TGA measurements were not performed for samples in sets 2 and 3. However, their initial masses were kept consistent to ensure comparable reduction behaviour.

Table 3. Values of the initial mass (m_0), relative change in mass loss ($\Delta m(t)/m_0$) and reduction degree (R) for samples in set 1 and TGA_5_10Ni_RSS900, along with the corresponding temperatures (T) and times (t) at which these occurred.

Sample	**m_0 (mg)**	**$\Delta m(t)/m_0$, $\pm$ 0.002**	***R* [-] $\pm$ 0.002**	***T* (°C)**	***t* (s)**
TGA_10/5_10Ni_560	508	-0.2940	0.995	900	7300
TGA_10/5_10Ni_590	386	-0.2974	1.002	836	5600
TGA_10/5_10Ni_620	440	-0.2946	0.996	900	6200
TGA_5_10Ni_RSS900	442	-0.2936	1.000	830	10407

The theoretical mass loss for complete reduction of the Fe_2O_3 + NiO (9:1) system was calculated as 0.2920. All experimental values exceeded this theoretical prediction. Several factors may explain these deviations. First, the initial oxide composition may have deviated

from the ideal stoichiometric 9:1 Fe_2O_3 to NiO ratio, potentially due to: (i) incomplete homogenisation during ball milling, (ii) segregation of powders during handling and cold isostatic pressing, and/or (iii) incorrect sampling of the powder mixture. These factors could introduce local variations in oxygen content. Second, instrumental effects such as baseline drift (although often negligible) and gas buoyancy changes during TGA may have contributed to small measurement errors. Third, sintering during reduction might have caused physical dislodgement or spallation of fine particles, leading to apparent mass loss unrelated to oxygen removal. Cross-validation using XRD and microstructural analysis is therefore essential for accurate interpretation of the reduction extent.

Pore analysis was performed on the SEM-BSE images acquired from various sections of each sample, as shown in Figure 33 to 43. The resulting data, presented in Figure 32, compares the average pore size, circularity and connectivity across samples in sets 1, 2 and 3. Overall, significantly smaller pore sizes (Figure 32(a)) were observed in sets 2 and 3 (< ~0.2 μm) compared to set 1 (average of 0.4 μm). This highlights the effect of a slower heating rate (10 °C/min vs 5 °C/min), which allowed reduction to progress further before sintering became dominant. All samples displayed pore circularity (Figure 32(b)) greater than 0.83, with set 2 displaying the highest average pore circularity (0.94 ± 0.03). The combination of high circularity and low pore connectivity (< 7%) for samples in set 2 suggested the formation of well-isolated, rounded pores. In contrast, sample TF_5/20_17Ni_460 displayed the highest connectivity due the abnormally large pores seen in Figure 39, section (e), which skewed the average and increased error (observed in Figure 32(c)).

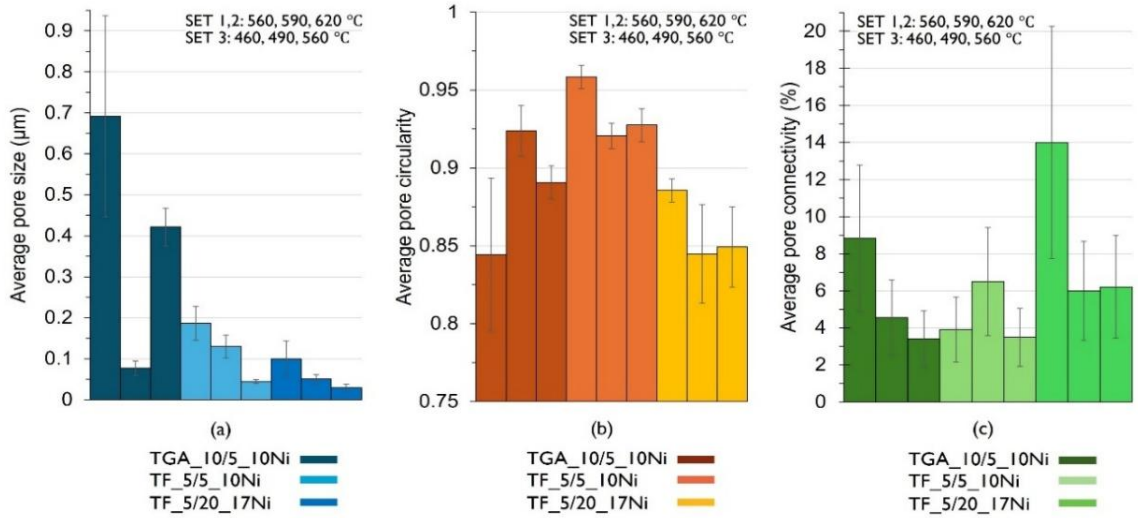

Figure 32. (a) Average pore size (μm) (b) pore circularity (1 indicates a perfect circle) and (c) pore connectivity (%), for samples in sets 1, 2 and 3.

In both TGA_10/5_10Ni_560 (Figure 33) and TF_5/20_17Ni_460 (Figure 39), pore fraction varied significantly across the specimen. In these samples, as well as in sample TF_5/5_10Ni_560 (Figure 36), sections (d) and (e), showed the highest pore fractions. These regions featured pores with irregular and/or elongated morphology, paired with lower circularity (0.84 ± 0.1) for TGA_10/5_10Ni_560. High pore connectivity was also recorded in both TGA_10/5_10Ni_560 (9% ± 4%) and TF_5/20_17Ni_460 (14% ± 6%). In contrast, the cores of TGA_10/5_10Ni_560 and TF_5/20_17Ni_460 contained more circular pores and

exhibited the lowest pore fractions. Other samples displayed relatively uniform pore fractions across sections (< 1.4% standard deviation). Occasionally, localised regions of differing density were observed within the same section, as illustrated in Figure 36(d) for TF_5/5_10Ni_560, where high density (orange), and low density (green) areas are highlighted. Notably, samples synthesised in TGA (set 1) showed greater deviations in pore fraction compared to those produced in the tube furnace (sets 2 and 3), underscoring the influence of the slower heating rate in promoting more uniform thermal gradients. Additionally, differences in experimental set-up and atmospheric conditions may have further contributed to these variations.

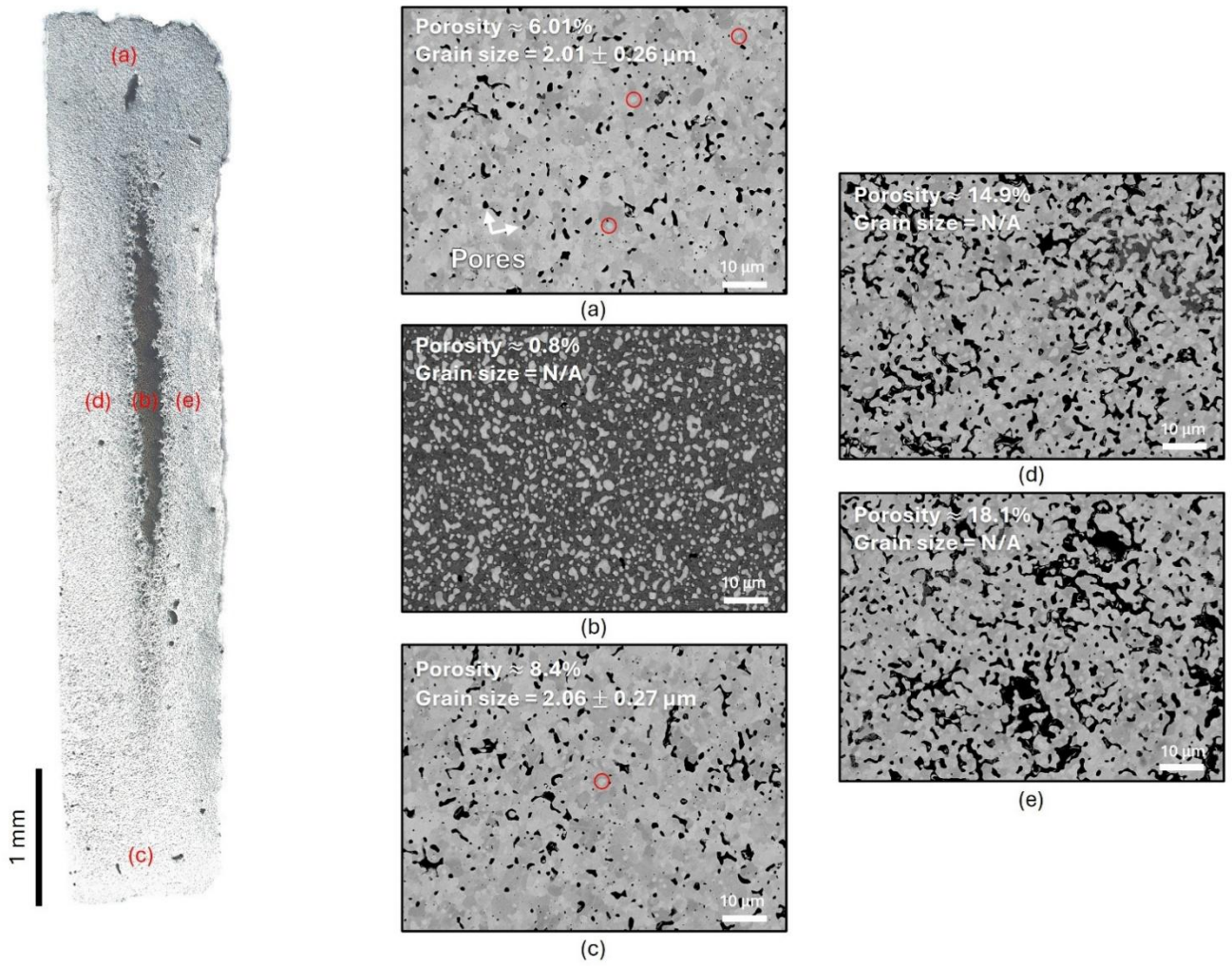

Figure 33. Optical micrograph of the cross-section of TGA_10/5_10Ni_560 (left). BSE images of sections (a – e) show the polished microstructures used for microstructural analysis. White arrows show examples of pores and red circles highlight smaller and brighter features.

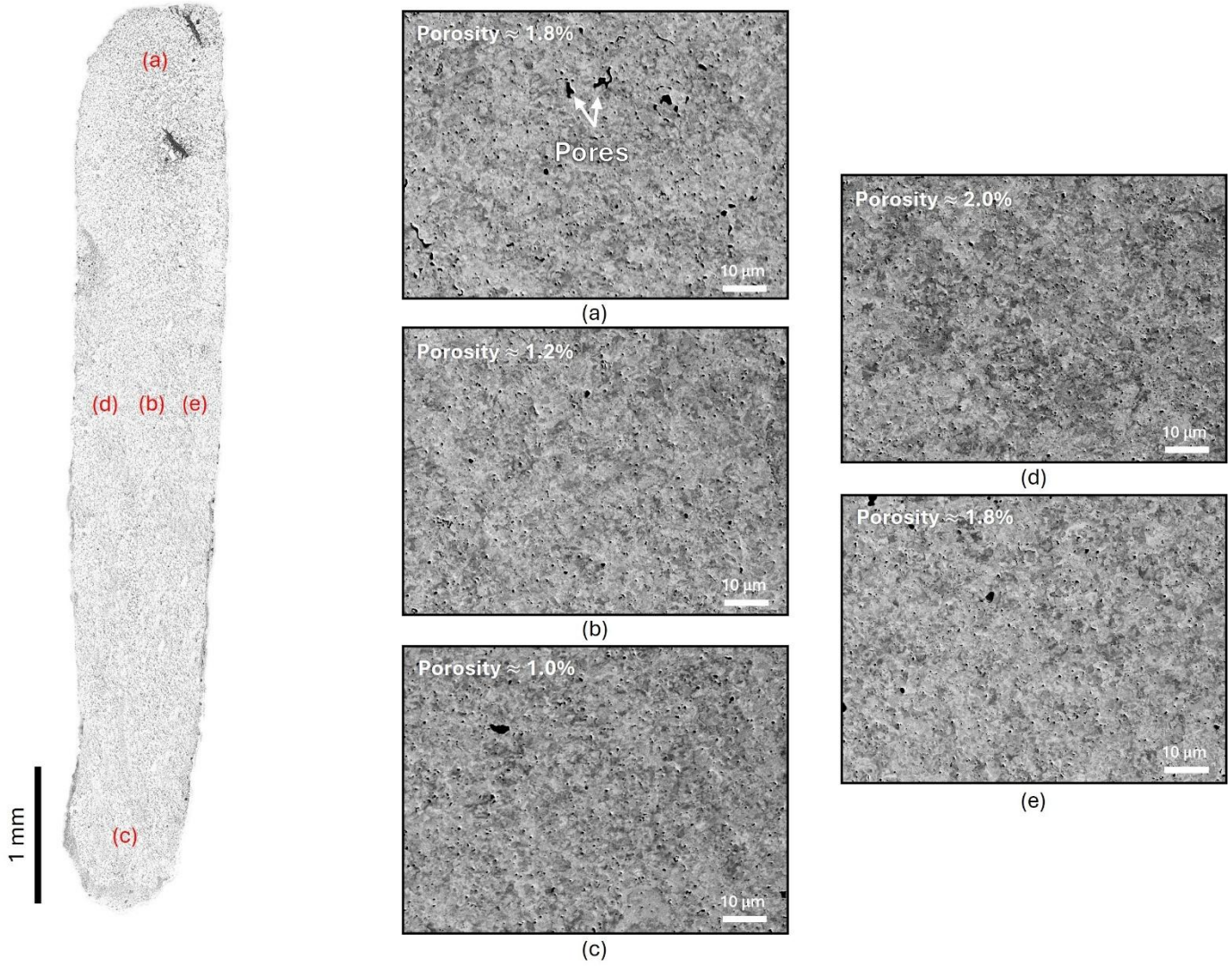

Figure 34. Optical micrograph of the cross-section of TGA_10/5_10Ni_590 (left). BSE images of sections (a – e) show the polished microstructures used for microstructural analysis. White arrows show examples of pores.

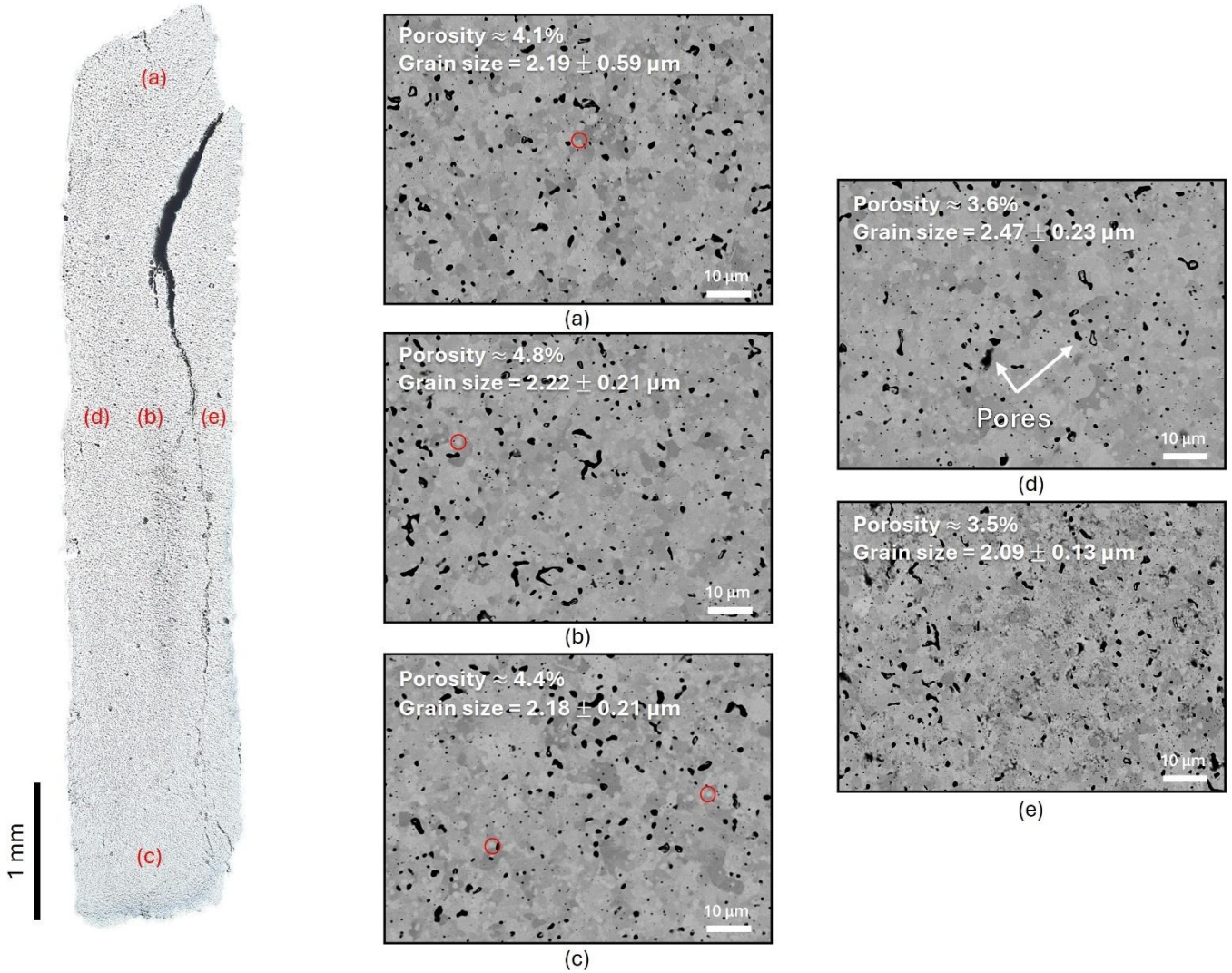

Figure 35. Optical micrograph of the cross-section of TGA_10/5_10Ni_620 (left). BSE images of sections (a – e) show the polished microstructures used for microstructural analysis. White arrows show examples of pores and red circles highlight smaller and brighter features.

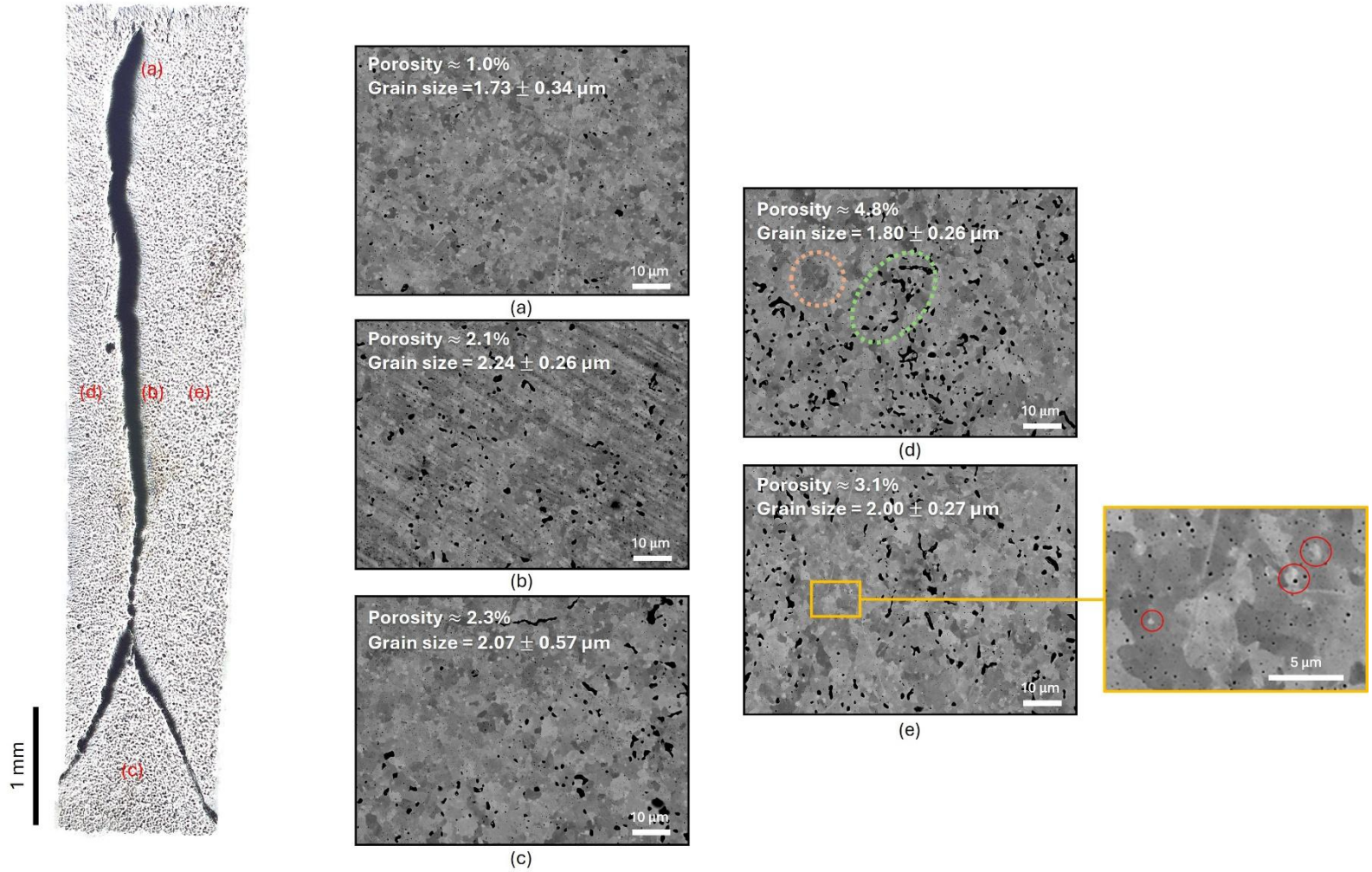

Figure 36. Optical micrograph of the cross-section of TF_5/5_10Ni_560 (left). BSE images of sections (a – e) show the polished microstructures used for microstructural analysis. Examples are given of pores (white arrows), smaller and brighter features (circled in red) and varying density across the across section (d) (high marked with orange and low with green).

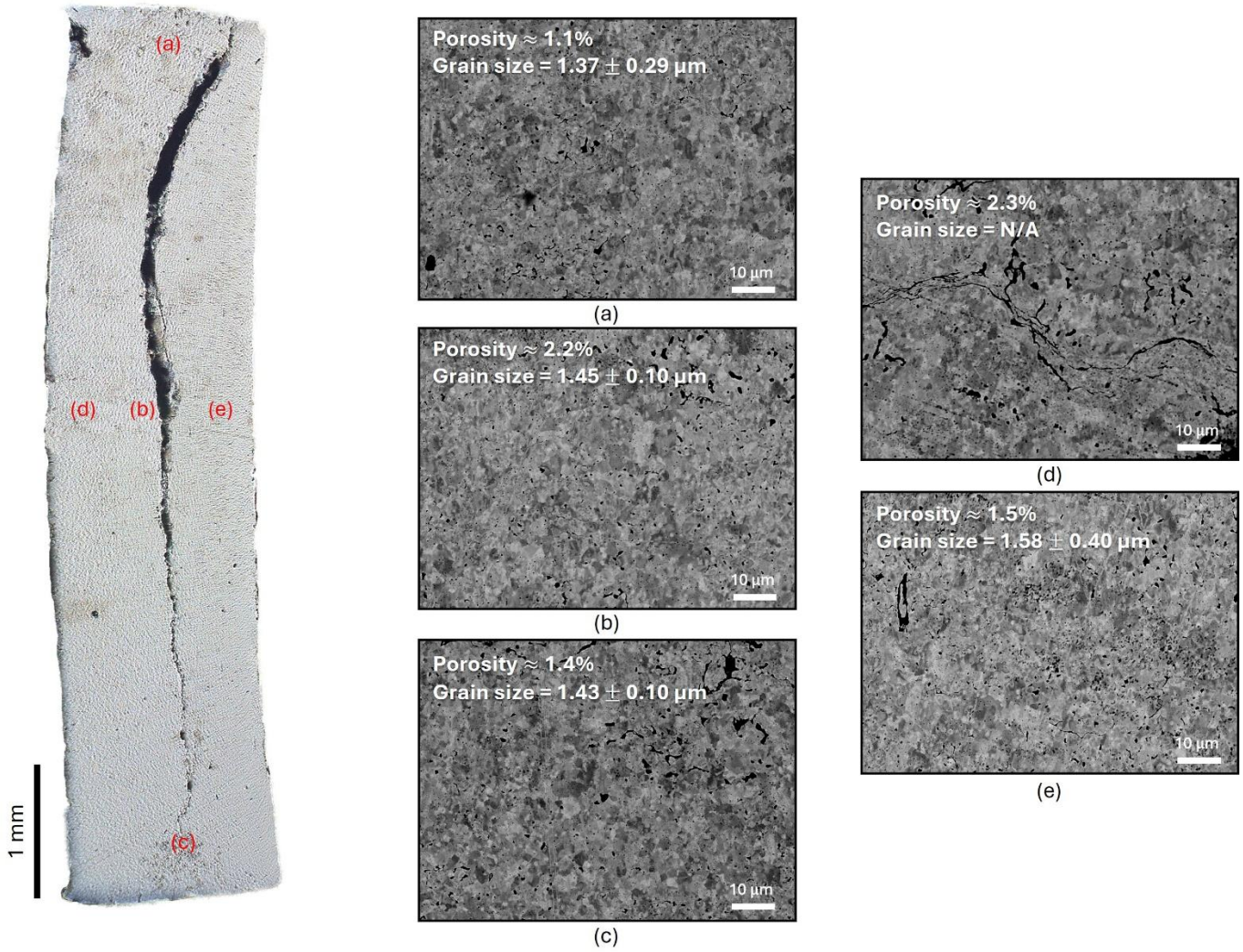

Figure 37. Optical micrograph of the cross-section of TF_5/5_10Ni_590 (left). BSE images of sections (a – e) show the polished microstructures used for microstructural analysis.

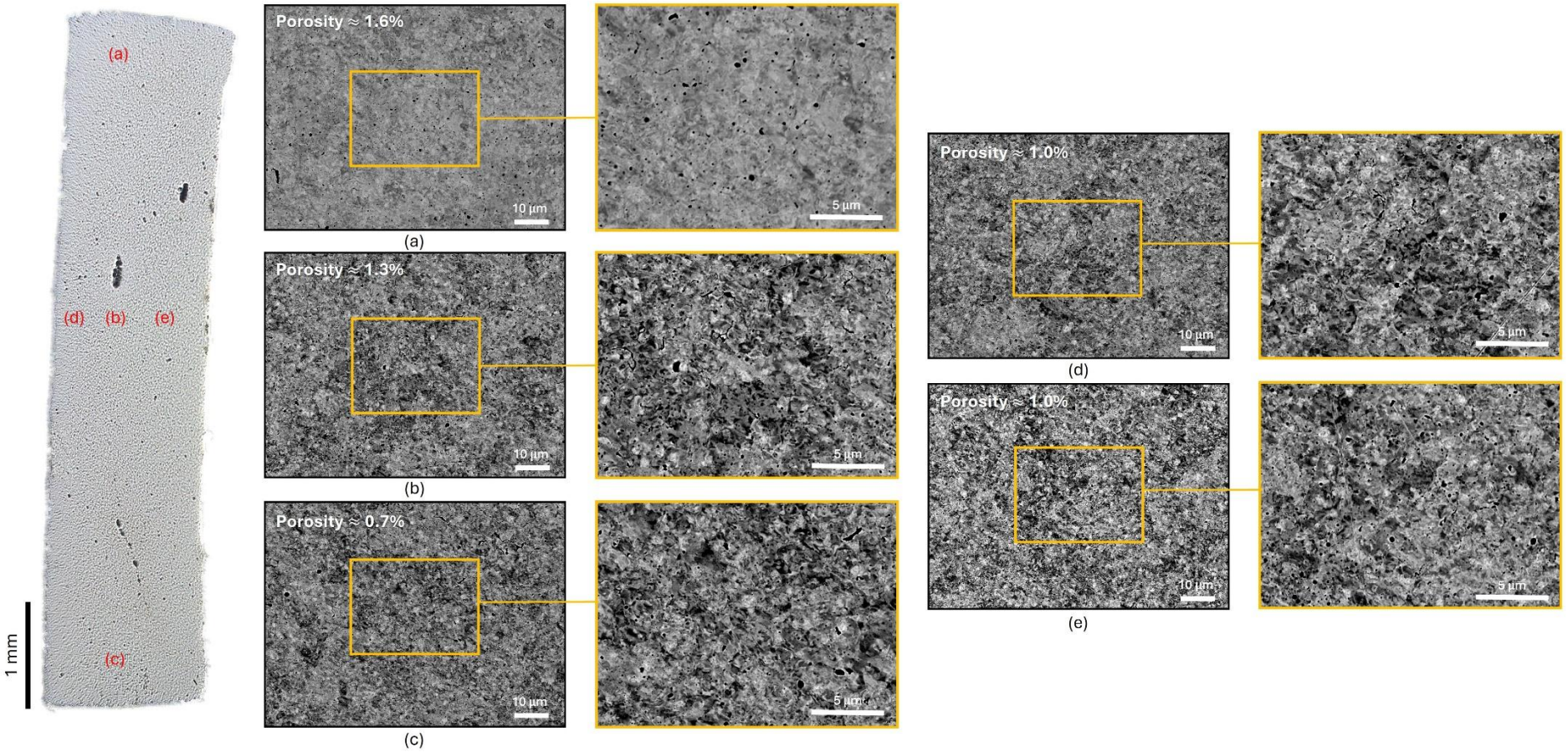

Figure 38. Optical micrograph of the cross-section of TF_5/5_10Ni_620 (left). BSE images of sections (a – e) show the polished microstructures used for microstructural analysis.

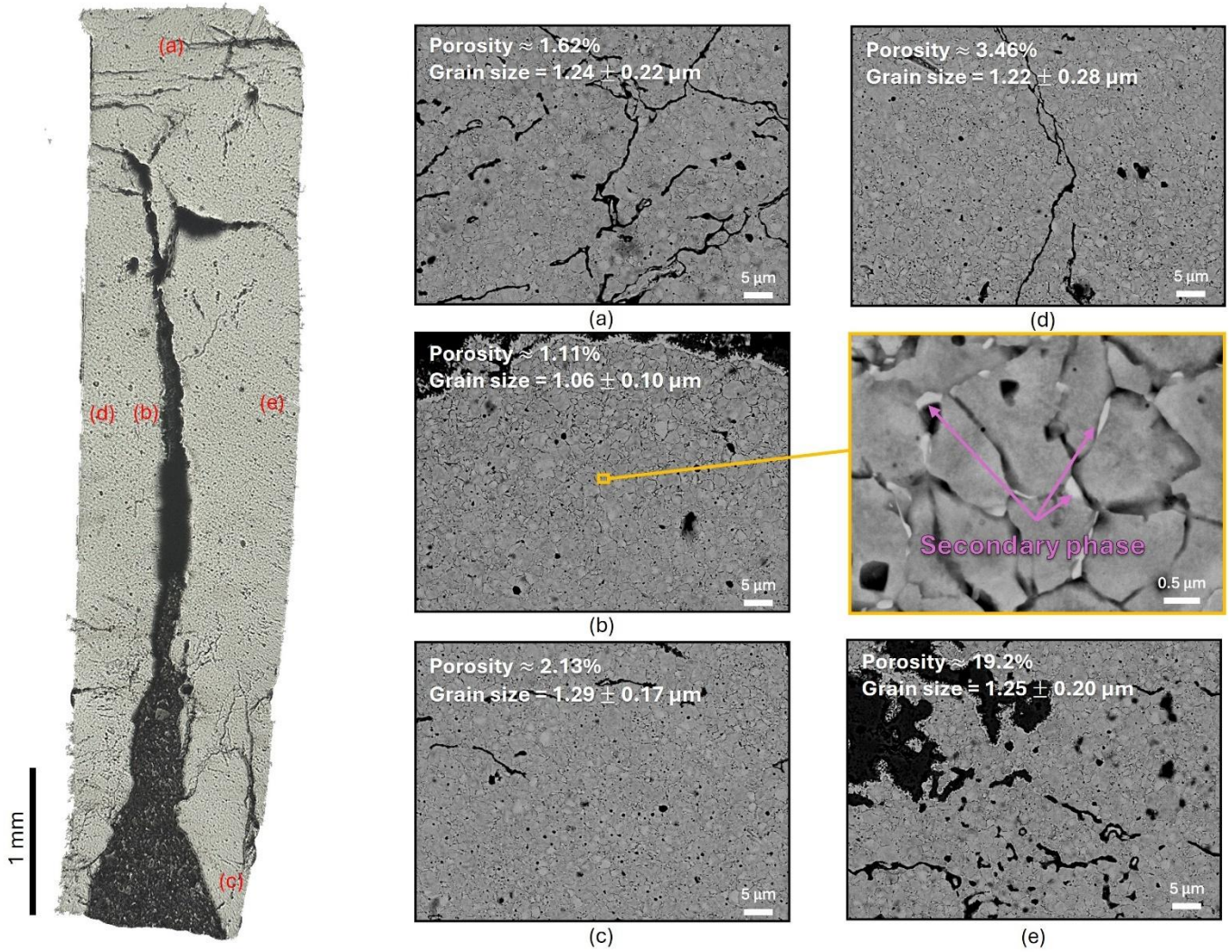

Figure 39. Optical micrograph of the cross-section of TF_5/20_17Ni_460 (left). BSE images of sections (a – e) show the etched microstructures used for microstructural analysis. Examples of a secondary phase at grain boundaries is indicated by purple arrows.

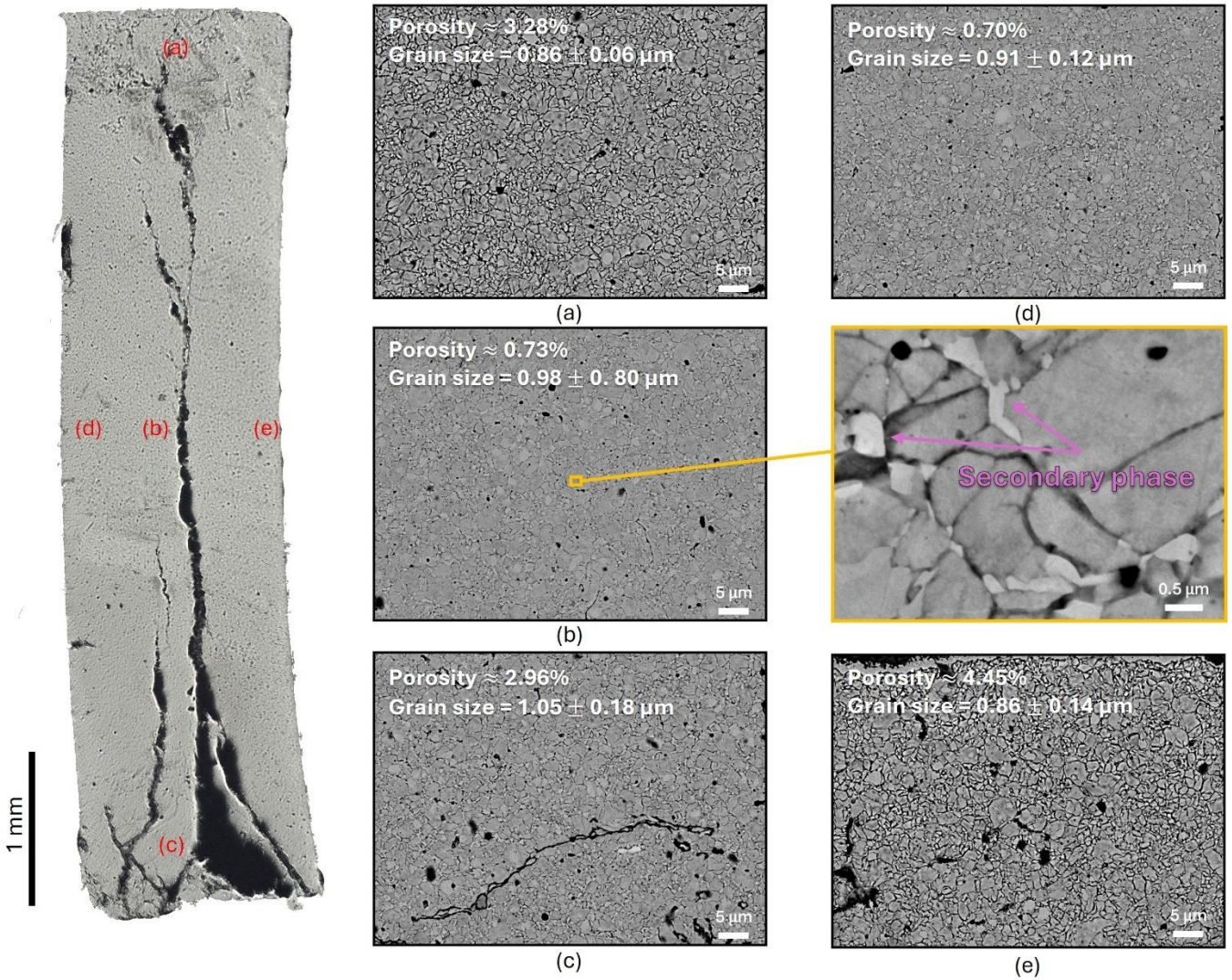

Figure 40. Optical micrograph of the cross-section of TF_5/20_17Ni_490 (left). BSE images of sections (a – e) show the etched microstructures used for microstructural analysis. Examples of a secondary phase at grain boundaries is indicated by purple arrows.

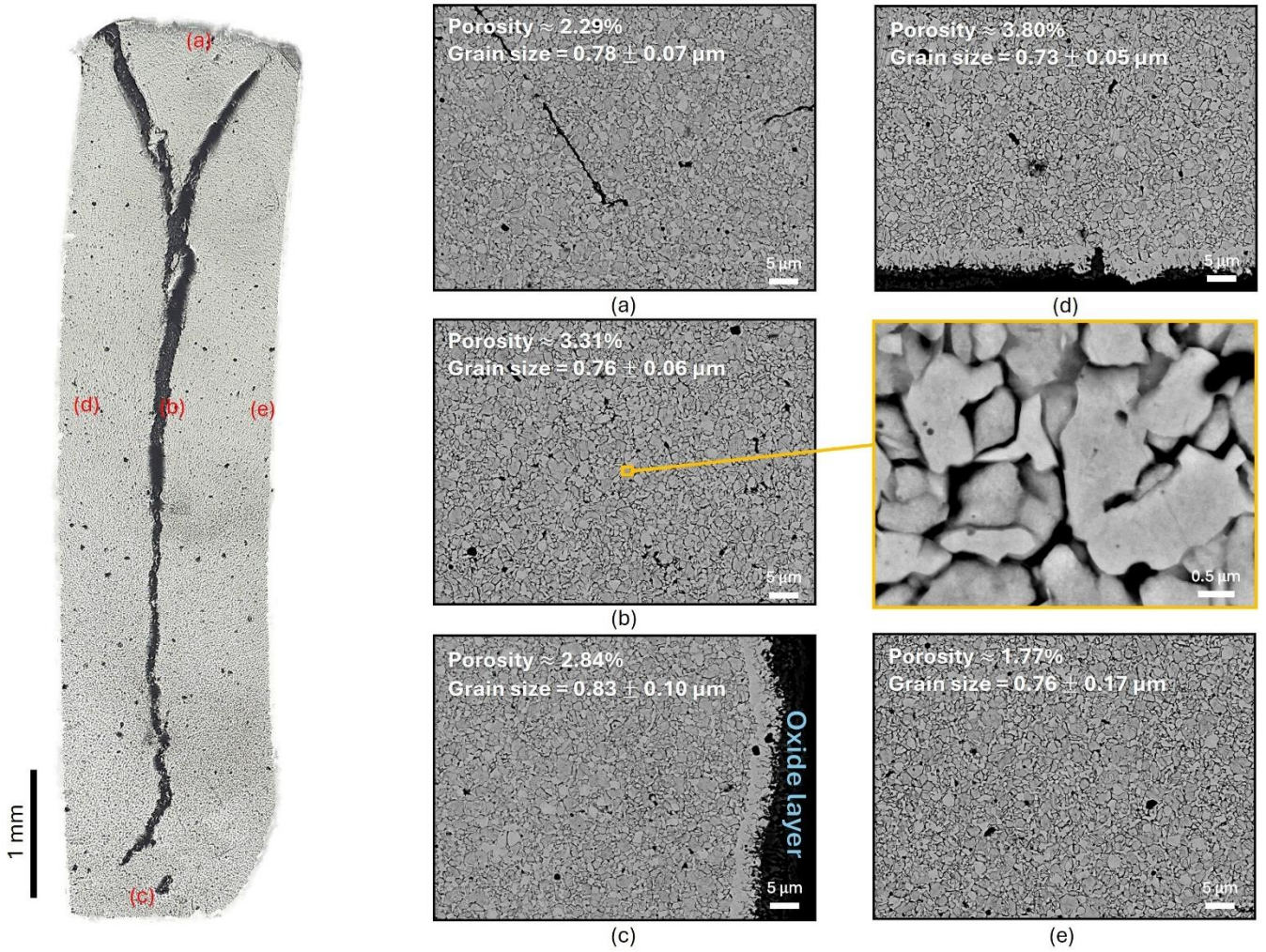

Figure 41. Optical micrograph of the cross-section of TF_5/20_17Ni_560 (left). BSE images of sections (a – e) show the etched microstructures used for microstructural analysis.

4.2. Microstructural analysis after intercritical annealing

Microstructural analysis after intercritical annealing was conducted on all samples (Figure 33 to 43) to evaluate which processing conditions were most effective in producing a duplex austenite-ferrite phase with a UFG microstructure, as targeted in this work. Observations focused on grain morphology and contrast to distinguish between the phases and assess the microstructural characteristics.

Samples in set 2 consistently exhibited finer grain sizes compared to their set 1 counterparts. Among them, sample TGA_10/5_10Ni_620 exhibited the coarsest grains, reaching up to 2.47 ± 0.23 µm (Figure 35(d)). In contrast, TF_5/5_10Ni_590 exhibited the most refined grain structure, with grains as small as 1.37 ± 0.29 µm, shown in Figure 37(a). In addition to differences in thermodynamic driving forces, grain size variations may also have originated from differences in the initial martensitic microstructure, despite nominally identical heat treatments. Within each sample, grain size differences across sections were influenced by differing local diffusion kinetics due to thermal gradients, compositional inhomogeneity, and variations in porosity and/or reduction extent. Generally, higher local temperatures or Ni content promote grain growth, whereas poorly homogenised or more porous regions tend to retain finer grains.

All samples in set 3 exhibited average grain sizes below ~1.25 µm with low variations across individual sections (< 0.09 µm standard deviation). Although all samples exhibited some degree of cracking along the centre, smaller grains adjacent to the cracks were not observed except in TF_5/20_17Ni_460 (Figure 39), which had the largest crack spanning the entire cross-section. This may have contributed to localised grain refinements near the fracture (Figure 39 (b)). These cracks likely resulted from high internal stresses during sintering, cooling and/or phase transformations. Both samples TF_5/20_17Ni_490 (Figure 40) and TF_5/20_17Ni_560 (Figure 41) had ultrafine grains (100 nm < x < 1 µm). Unexpectedly, grain size decreased with increased intercritical annealing temperature. The marked differences in grain sizes between sets 1 and 2 versus set 3 are likely due to the higher Ni content in set 3, which promoted secondary phase nucleation (see magnified image in TF_5/20_17Ni_460 Figure 39(b)). This nucleation led to grain impingement and inhibited growth.

No distinct grain boundaries were observed in TGA_10/5_10Ni_590 (Figure 34) and TF_5/5_10Ni_620 (Figure 38) at the given magnification, suggesting an ambiguous phase, possibly fresh martensite. This was accompanied by significantly lower average pore fractions compared to other samples. All samples in sets 1 and 2 contained a high fraction of nanoscale features; an example is shown in the magnified image in Figure 36(e). It remains unclear whether these are $FeNi_3$ precipitates formed during slow heating from room temperature to the intercritical annealing temperature, or nano-sized pores.

All samples in sets 1 and 2, except those with the ambiguous phase, displayed brighter, well-defined circular grains, examples in Figure 33, 5 and Figure 36. These features may indicate the nucleation of a secondary, possibly FCC phase, observed at grain boundaries, pore boundaries, and occasionally within relatively darker grains (Figure 36(e)). Similar features were also present in the set 3 samples, though with less circularity, due to the etching. In set 3, these features nucleated exclusively at grain boundaries, with largest size and highest frequency observed in TF_5/20_17Ni_490 (Figure 40).

4.3. Thermodynamic predictions of phases and their fractions upon intercritical annealing of Fe-10Ni and Fe-17Ni alloys

The method by De Cooman [47] explained in 2.4.2, was applied to the Fe-10Ni and Fe-17Ni binary systems, shown in Figure 42 and Figure 43, respectively. The predictions were made under equilibrium conditions, considering only thermodynamic factors. However, designing a heat treatment for real systems also requires accounting for nucleation and diffusion, as these affect the kinetics and element partitioning between phases.

In both systems, Figure 42(a) and Figure 43(a) show that below 368 ℃, only ferrite and $FeNi_3$ are stable. Between 368 ℃ and 408 ℃, a ferrite-austenite region exists. In this range, austenite formed has ferromagnetic properties, as its equilibrium composition lies below the Curie temperature. Beyond 408 ℃, the austenite phase becomes paramagnetic. Both types of austenite share the same crystal structure. The intercritical region, shown shaded in grey, lies between approximately 368 ℃ and 680 ℃ and 610 ℃ for Fe-10Ni and Fe-17Ni alloys respectively. Figure 42(b) and Figure 43(b) present the phase fractions corresponding to equilibrium conditions, which clearly demonstrate the evolving proportions of both phases with increasing IA temperature.

The composition of the austenite phase for both compositions is shown in Figure 42(c) and Figure 43(c). In Fe-10Ni (Figure 42(c)), the austenite phase contains approximately 23 wt.% Ni at 560 ℃ and increases to ~16 wt.% Ni at 620 ℃. In Fe-17Ni (Figure 43(c)), the austenite Ni content drops from ~36 wt.% at 460 ℃ to ~23 wt.% at 560 ℃. This decline demonstrates that lower intercritical annealing temperatures significantly increase the thermodynamic driving force for Ni partitioning into austenite. Figure 42(d) and Figure 43(d) display the martensite start temperatures at different IA temperatures. For both systems, intercritically annealing ≤ 520℃ results in a M_s temperature at or below room temperature, meaning that no martensite forms during cooling. Finally, Figure 42(e) and Figure 43(e) present the final phase fractions of reversed austenite and fresh martensite (transformed from unstable austenite) at room temperature. For the selected IA temperatures marked in green, the final fractions of all phases present at room temperature are given in Table 4. Specifically, reversed austenite fractions of 9%, 4%, and 2% are expected in Fe-10Ni, and 38%, 45% and 20% in Fe-17Ni, corresponding to the lowest to highest IA temperatures, respectively.

Table 4. Predicted phase fractions of ferrite (%), fresh martensite (%) and reversed austenite (%) for Fe-10Ni and Fe-17Ni binary systems.

x_{Ni} (wt.%)	T (℃)	f_{α} (%)	f_{RA} (%)	$f_{\alpha'}$ (%)
Fe-10Ni	560	71	8	21
	590	63	4	33
	620	52	2	46
Fe-17Ni	460	62	38	0
	490	55	45	0
	560	32	20	48

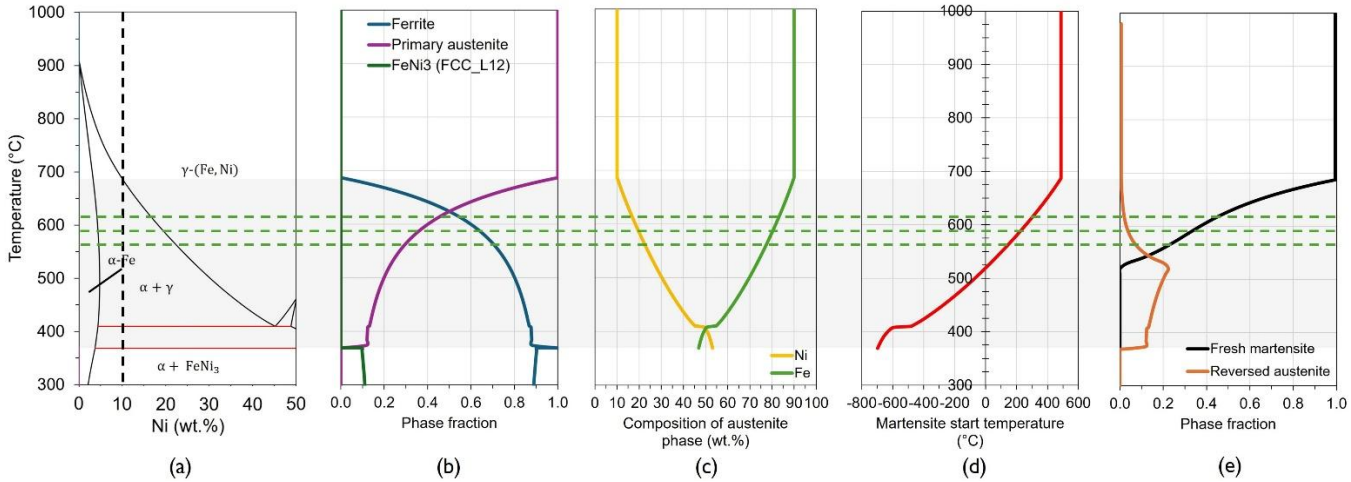

Figure 42. (a) Fe-Ni phase diagram. Temperature (℃) plotted against (b) phase fraction (c) austenite phase composition (wt.%) (d) martensite start temperature (℃) and (e) final fractions of reversed austenite and fresh martensite in Fe-10Ni at intercritical annealing temperatures of 560 ℃, 590 ℃ and 620 ℃.

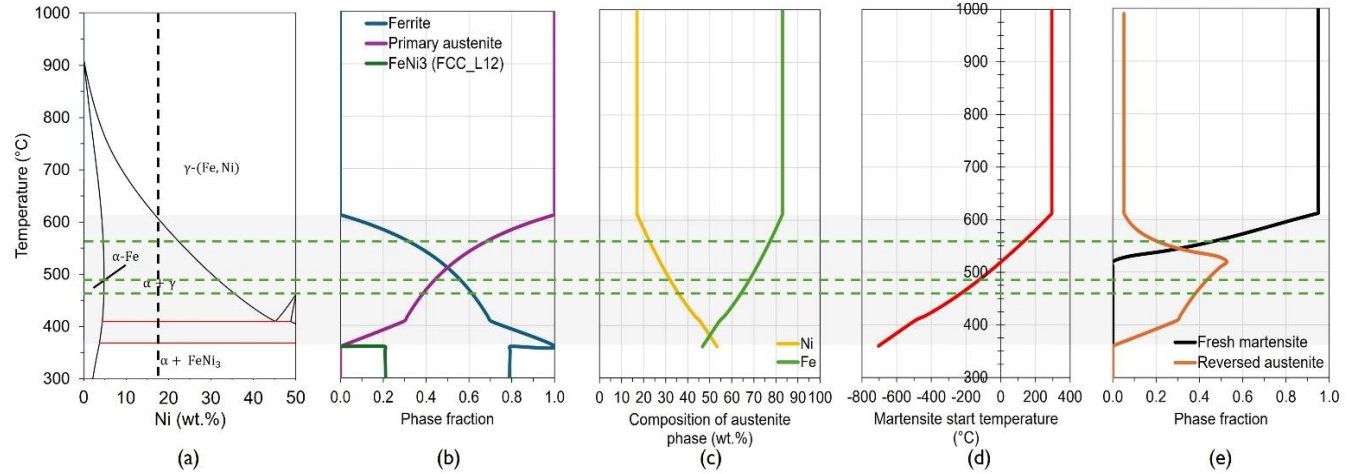

Figure 43. (a) Fe-Ni phase diagram. Temperature (℃) plotted against (b) phase fractions (c) austenite phase composition (wt.%) (d) martensite start temperature (℃) and (e) final fractions of reversed austenite and fresh martensite in Fe-17Ni at intercritical annealing temperatures of 460 ℃, 490 ℃ and 560 ℃.

4.4. Phase identification, fractions, and their correlation with intercritical annealing tempreature

The XRD patterns of both sets 1 and 2, and set 3 are presented in Figure 44(a) and (b) respectively. The diffraction patterns revealed the presence of both FCC and BCC phases in all samples, indicating that a two-phase structure has been obtained with the chosen processing conditions. Quantitative phase analysis of diffraction patterns seen in Figure 44 was carried out via Rietveld refinement, and are presented in Table 5. The analysis revealed that BCC is the dominant phase across all samples with FCC phase fractions of < 5% and < 15% for Fe-10Ni and Fe-17Ni compositions respectively.

The BCC phase detected by XRD may not exclusively correspond to ferrite. As predicted in Table 4 for Fe-10Ni compositions, given the thermal history and transformation pathways of these samples, it is plausible that a portion of the BCC signal arises from the presence of fresh martensite at room temperature. Similarly, the FCC phase may not be solely attributed to austenite but rather to a combination of austenite and ordered intermetallic $FeNi_3$. Shoulder peaks at α-Fe peaks at approximately 100° and 123° were observed in all sets. These are mostly likely a result of incomplete filtering of the Co K_{α_2} line (1.792 Å), which diffracts the X-rays to slightly higher angles than the main K_{α_1} component (1.789 Å), leading to peak asymmetry at these high 2θ values [80].

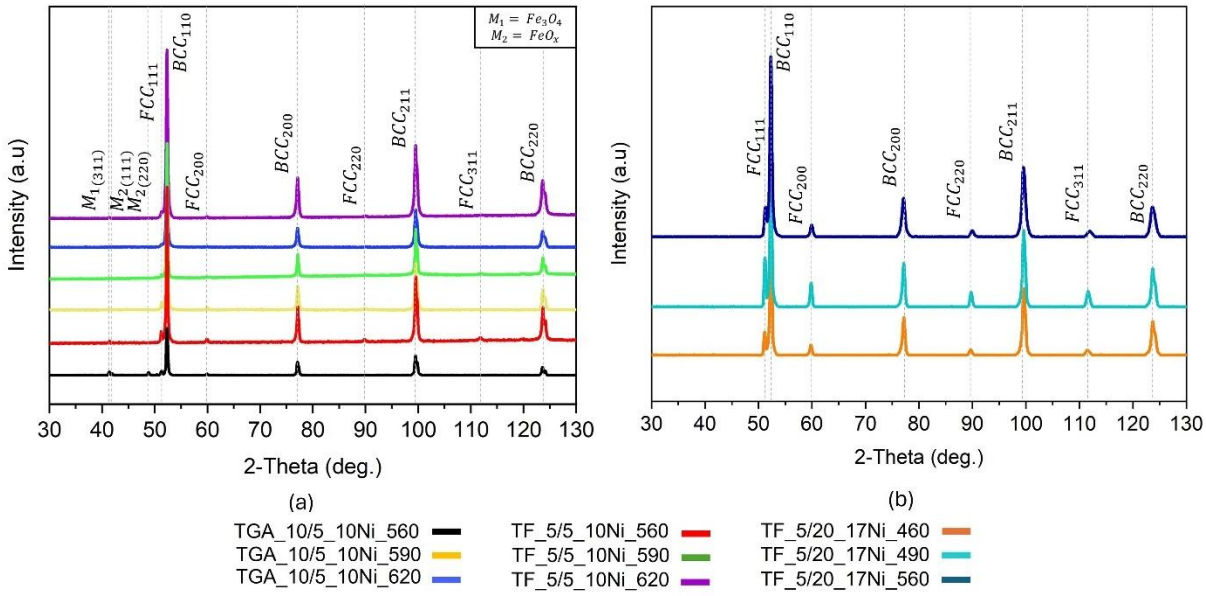

Figure 44. X-ray diffraction patterns for (a) sets 1 and 2 and (b) set 3. The diffraction pattern of sample TGA_10/5_10Ni_560 was initially measure using Cu radiation and later converted to Co radiation which resulted in shifted peaks to different 2θ that satisfy Bragg's law for this radiation type. Sample TGA_10/5_10Ni_560 showed the presence of phases $M_1 = Fe_3O_4$ and $M_2 = FeO_x$.

Additional peaks were detected in sample TGA_10/5_10Ni_560 at low 2θ, corresponding to a total 10% residual Fe_3O_4 and FeO_x. Based on the evidence of microstrucutral differences in Figure 33, section (b), and the detection of oxides, the reduction degree of this sample was reassessed and esimtated using two approahces. First, by calculating the ratio of the surface area of oxides to the assumed fully reduced portion of the sample. Second, by comparing the oxide phase fractions, provided in Table 5, to the fraction of the metallic phases. An average final reduction degree of 0.925 was obtained. The stark discrepancy between this value and

the reduction degree dervied from TGA indicated that the TGA_derived result was unreliable and should be considered an outlier. In contrast, other Fe-10Ni samples exhibited negligible oxide content and therefore corresponded well with the reduction degrees calculated from TGA measurements.

A general correlation between FCC phase fraction and IA temperature was observed for sets 1 and 2. The highest FCC phase fractions were recorded at 560 ℃, reaching up to 5% for TGA samples and 3% for TF samples, while a lower fraction of 1% was measured at 620 °C. Typically, phases present under 5% are considered unreliable due to the detection capability of laboratory XRD as this leads to weak peak intensity (low signal-to-noise ratio) and overlapping features. Due to the low FCC fractions in samples forming sets 1 and 2, no confident conclusions can be drawn from these values as these results are likely affected by high experimental error.

In contrast, the relative intensity of the diffraction patterns for the Fe-17Ni samples is considered more reliable, given the higher FCC fraction (Table 5). The highest relative intensity for set 3 was observed for TF_5/20_17Ni_490, which displayed a 15% FCC volume fraction. Meanwhile, the lowest relative intensity was seen for TF_5/20_17Ni_460, which achieved an FCC phase fraction of 7%. Factors such as sample misalignment, surface roughness, and the relatively shallow penetration depth of approximately 16 μm (compared to 20 μm [80] for Cu K_α radiation) for Co K_α radiation in iron-based materials might have given rise to measurement uncertainty in all samples.

Table 5. Phase fractions and a fitting error of 0.002% obtained using Rietveld refinement.

Sample	FCC (%)	BCC (%)	FeO_x (%)	Fe_3O_4 (%)
TGA_10/5_10Ni_620	1	97	-	-
TGA_10/5_10Ni_590	3	97	-	-
TGA_10/5_10Ni _560	5	85	5	5
TF_5/5_10Ni_620	1	99	-	-
TF_5/5_10Ni_590	3	99	-	-
TF_5/5_10Ni_560	3	97	-	-
TF_5/20_17Ni_560	8	92	-	-
TF_5/20_17Ni_490	15	85	-	-
TF_5/20_17Ni_460	7	93	-	-

Microstructural and phase characterisation of Fe-17Ni samples using EBSD and EDX

Further investigation into the phase distribution, fraction, and relative misorientation was conducted exclusively on the Fe-17Ni samples. Section (b) in Figure 39 to 11, corresponding to the samples comprising set 3, was subjected to EBSD analysis. Inverse pole figures (IPF), phase maps and KAM maps were generated to visualise local phase orientation, distribution and grains with higher strains indicate of local lattice distortions due to martensitic transformation. In addition, phase maps were used to determine average phase fractions for

these sections. EDX was performed to completement the EBSD analysis by providing local composition information to help distinguish between FCC and BCC phases.

Inverse pole figures for all samples in SET 3 revealed no dominant orientation in reference to the given sample direction. This is indicative of a random texture along the ND; an example is shown for TF_5/20_17Ni_460 in Figure 45. This was expected, as samples in this study were synthesised from powders and were not subjected to any texturising process.

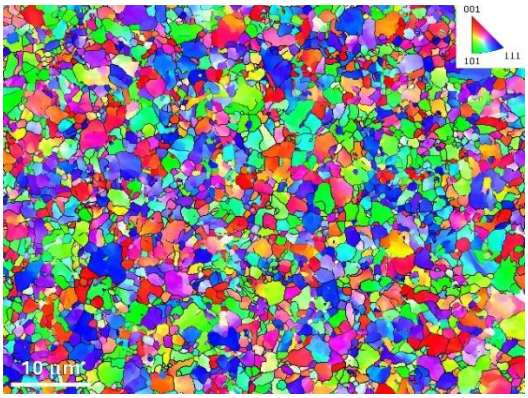

Figure 45. The inverse pole figure of sample TF_5/20_17Ni_460 at section (b). Grain boundaries (black) indicate misorientation angles greater than 10°.

Phase maps for each section of the set 3 samples are presented in Figure 47. As recorded for the global FCC fraction by XRD, sample TF_5/20_17Ni_490 (Figure 47(b)) exhibited the highest local FCC fraction (5.57%), followed by TF_5/20_17Ni_560 (2.27%), shown in Figure 46(c). Consistent with these results, TF_5/20_17Ni_490 showed the largest and most uniformly distributed FCC grains, with TF_5/20_17Ni_560 displaying fewer FCC grains with far less extensive distribution. FCC phases were observed to form predominantly along high angle grain boundaries, possibly confirming that the brighter secondary phase seen in the SEM-BSE images (Figure 39 to Figure 41). Some FCC was also seen within BCC phases for TF_5/20_17Ni_460 and TF_5/20_17Ni_490, suggesting the presence of high-energy defects promoting localised phase transformation.

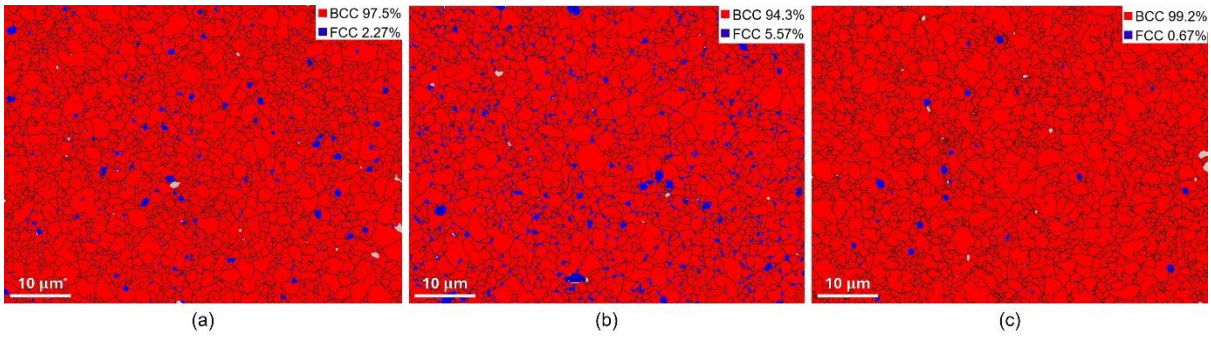

Figure 46. Phase maps taken at the core for (a) TF_5/20_17Ni_460, (b) TF_5/20_17Ni_490 and (c) TF_5/20_17Ni_560.

Compositional information was gathered using energy dispersive X-ray (EDX) to identify the nature of the contrasted grains observed in Figure 33 to 11. In the EDX area maps shown in Figure 47(a-c), blue regions indicate higher concentrations of Fe, whilst orange regions represent areas enriched with Ni. The average nickel contents measured from the area maps for samples intercritically annealed at 460 ℃, 490 ℃ and 560 ℃, were 16.89 wt.%, 16.41 wt.%

and 16.31 wt.%, respectively. More specifically, the line scan profiles shown in Figure 47(d – f) illustrate the composition variations across individual grains, where an increase in Ni wt.% corresponds to a decrease in Fe content. This inversed relationship was most pronounced in the TF_5/20_17Ni_560 sample. In this sample, although multiple Ni-enriched regions were observed, highlighted by the widespread orange zones in the area map, the overall Ni content of this area (16.31 wt.%) was the lowest. When cross-referenced with back-scattered electron imaging, higher Ni content was consistently observed within brighter grains, while darker grains were enriched in Fe.

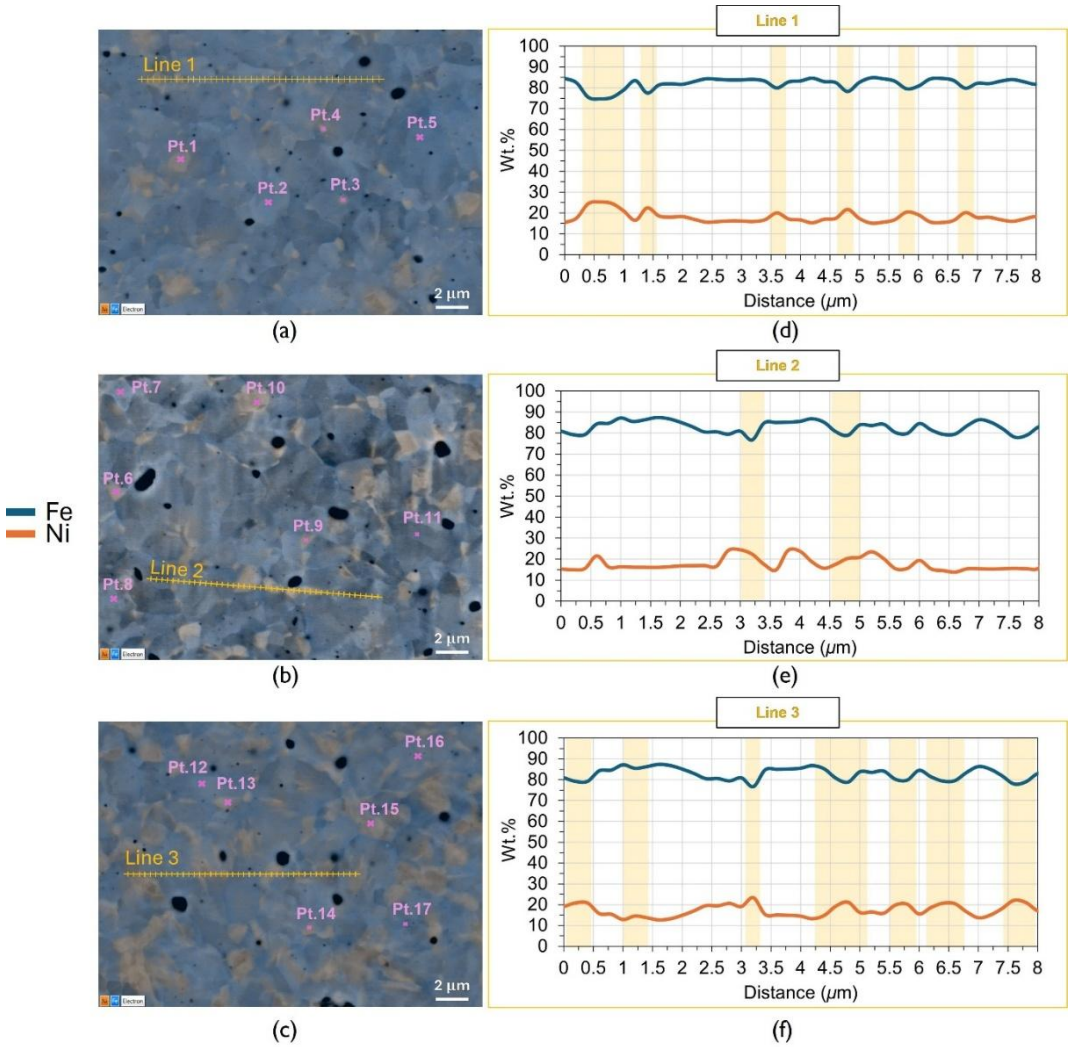

Figure 47. (a-c) EDX area maps showing elemental distribution (orange = Ni-rich regions, blue = Ni-lean) and mark locations of point and line scans. (d-f) Compositional profiles along lines 1 - 3, were recorded at 0.2 µm intervals. Samples correspond to (a,d) TF_5/20_17Ni_460, (b, e) TF_5/20_17Ni_490 and (c, f) TF_5/20_17Ni_560. All data were collected from the core regions.

Point measurements were taken from both Ni- enriched and lean regions (also shown in Figure 47(a-c)), as presented in Table 6. These measurements reveal significant compositional differences between these two regions. Among the samples, TF_5/20_17Ni_460 exhibited the highest nickel enrichment, with Ni content reaching an average of 25.75 wt.%. Contrastingly, sample TF_5/20_17Ni_490 showed the highest nickel content within nickel-lean area, suggesting a more uniform distribution of Ni. Sample TF_5/20_17Ni_560, had the highest overall Fe content in both nickel- rich and lean areas.

Table 6. Fe and Ni compositions (in wt.%) for regions marked by points 1 – 17 in Figure 47, corresponding to localised EDX measurements in Ni-rich and Ni-lean phases.

Sample	Points in Figure 47(a-c)	Ni (wt.%)	Fe (wt.%)	Std. Dev. (wt. %)
TF_5/20_17Ni_460	1 + 3 + 4	25.75	74.25	0.74
	2 + 5	14.24	85.72	1.10
TF_5/20_17Ni_490	6+7+11	25.63	74.37	1.33
	8+9+10	14.96	85.04	0.50
TF_5/20_17Ni_560	14+15+16	22.52	77.48	0.57
	12+13+17	14.16	85.84	1.05

The kernel average misorientation (KAM) quantifies the average misorientation around a measurement point relative to its nearest neighbours. The KAM maps and corresponding peak values distributions for the Fe-17Ni samples are presented in Figure 48. As shown in Figure 48(a) and 17(b), samples TF_5/20_17Ni_460 and TF_5/20_17Ni_490 exhibited regions with higher local misorientation, indicative of increased lattice distortions in these areas. In Figure 48(c), sample TF_5/20_17Ni_560 displayed higher average misorientation throughout the chosen section when compared to the other two samples in this set. This observation is further corroborated by the distribution plot in Figure 48(d), which confirmed that TF_5/20_17Ni_560 has the highest average misorientation, followed by TF_5/20_17Ni_460, and finally TF_5/20_17Ni_490. These findings are consistent with the predicted phases and their fractions in Table 4, which indicated that IA at 560 °C would result in the greatest fraction of martensite.

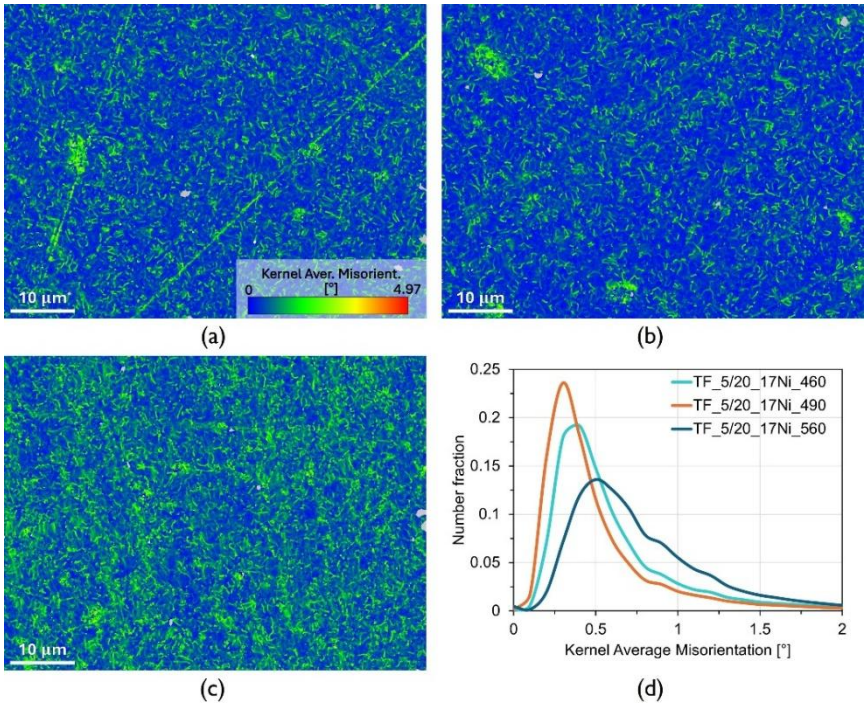

Figure 48. EBSD results of kernel average misorientation (KAM) maps of SET 3 samples, (a) TF_5/20_17Ni_460, (b) TF_5/20_17Ni_490 and (c) TF_5/20_17Ni_560. (d) KAM value distributions for this set.

5. Discussion

5.1. Reduction degree and reaction mechanism behaviour

The lower reduction degree of TGA_10/5_10Ni_560 (Fig 1 in results) can be traced to its higher initial mass (Table 1 in results), which yielded a denser green body and fewer hydrogen-adsorption sites. This can be seen from Figures 1(b) and (c) (results), which showed delayed mass loss as well as lower rate of mass loss in comparison to the other two samples, with higher reduction degrees. The slowed reduction kinetics likely allowed sintering to dominate, which further restricted both the inward diffusion of hydrogen and the outward escape of the reaction products. Consequently, reduction ceased before completion under the chosen heating rate (10 °C/min).

Figure 49 plots the reduction rate as a function of time and reduction degree for TGA_5_10Ni_RSS900, which obtained complete reduction, deconvoluted into three Gaussian peaks (orange = peak 1, green = peak 2, dark blue = peak 3) obtaining a $R^2 = 0.9816$. This data allows for clearer separation of the kinetic stages in these gas-solid reactions, since each transformation follows its own mechanism and produces a distinct rate profile. The phase fractions in Figure 6, derived for a Fe-36Ni invar alloy under the same heating rate, can therefore be used to match individual reduction-rate peaks to their corresponding reduction reaction mechanisms [12].

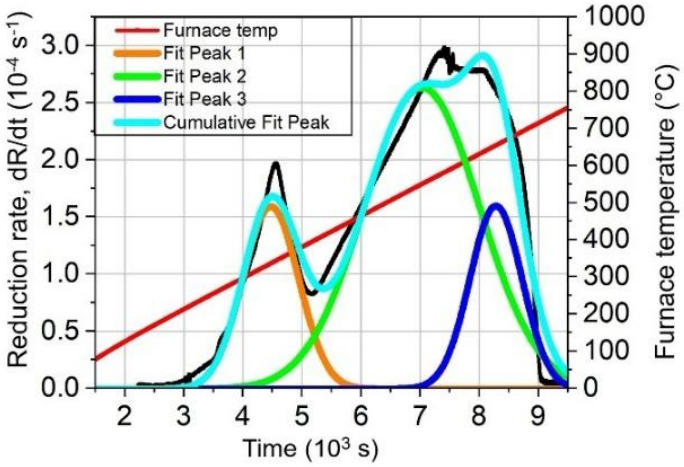

Figure 49. Reduction rate (dR, dt) against time for sample TGA_5_10Ni_RSS900, with deconvolution to three Gaussian peaks (orange = peak 1, green = peak 2, dark blue = peak 3) and cumulative fit (cyan) with R^2= 0.9816. The furnace temperature profile is shown in red on the secondary y-axis.

The onset temperature of the first reaction mechanism ($Fe_2O_3 \rightarrow Fe_3O_4$), was 170 °C in Fe-10Ni and 230 °C in Fe-17Ni alloys (Figure 49) in this study, whereas in Fe-36Ni samples, it occurred at 350 °C (Figure 6) [12]. This shift toward earlier temperatures in the lower-Ni alloys may indicate a predominance of the Fe_2O_3 to Fe_3O_4 transformation, driven by their higher Fe_2O_3 content and its higher thermodynamic driving force compared to NiO to Ni reduction. Conversely, in higher-Ni alloys, the increased dominance of the NiO to Ni transformation produces metallic Ni that can encapsulate Fe oxide particles, slowing hydrogen access and delaying subsequent Fe oxide reduction. The increased NiO fraction in these oxide blends increases the overall diffusion barrier in the oxide mixture, further promoting later onset of Fe_2O_3 reduction.

In this study, only one peak could be resolved at ≤ 350 ℃ (Figure 49). This is likely because the reduction rate of Fe_2O_3 is significantly higher at these temperatures (250℃-400 ℃) compared to NiO to Ni (Figure 6), which effectively masks the signal of the slower reaction. Peak 2 in Figure 49 exhibits a broader full width at half maximum, spanning over approximately 2×10^3 s compared to peaks 1 and 3, which each span around 1×10^3 s. Additionally, peak 2 shows the highest maximum reduction rate at 2.7×10^{-4} s^{-1}, compared to 1.60×10^{-4} s^{-1} for peak 1 and 1.75×10^{-4} s^{-1} for peak 3. The higher reduction rate of the second peak and the persistence of the observable shoulder in the original reduction rate trajectory (representing peak 3 in Figure 1(a)), provides strong evidence that the stepwise reduction of Fe_3O_4 to FeO and FeO to Fe did in fact occur. While Wei et al. [12] observed comparable reduction rates for peak maxima at low and higher temperatures, Y Zhang et al.[81] reported distinctively higher reduction rates at elevated temperatures, matching the pronounced kinetics seen here in Figure 49. The difficulty of fitting peaks 2 and 3 with a symmetrical model further highlights the inherent asymmetric rate profiles of each reduction mechanism.

5.2. Pore analysis to determine densification degree and mechanisms

TGA_10/5_10Ni_560 displayed the highest standard deviation across all pore metrics given in Figure 32. The distinct microstructural features and contrast between the core and other sections in Figure 33 suggested that residual oxides detected by XRD (Table 5) are likely concentrated within this region. The lower pore fraction (~0.8%) recorded at the central region in Figure 33(b) can therefore be attributed to the lower extent of pores originating from oxygen removal. Given the remaining detectable amounts of oxides, densification occurred before full reduction was allowed. In contrast, the side regions (d) and (e) displayed high porosity (14.9% and 18.9%, respectively) with large, irregular pores with a high interconnectivity, characteristic of limited densification and more advanced reduction progressions. These observations highlight the typical shell-core reduction mechanism associated with hydrogen-based direct reduction, where the outer regions are reduced first and the core is reduced last often modelled using the shrinking core model in literature [25,82].

The elongated and interconnected pores observed in sample TF_5/5_10Ni_590 Figure 37(d) and all set-3 samples, is typical of end-stage reduction, where evolving water vapour escapes and leaves behind open channels, later closed by subsequent sintering. Microstructural observations by Kim et al. [83] revealed increased and widespread cracking and delamination between ferrite and wüstite, driven by the large volume changes during reduction where the $Fe_2O_3 \rightarrow Fe_3O_4$ (r.4) step shrinks by ~1.9%, $Fe_3O_4 \rightarrow FeO_x$ (r.5) by ~19%, and FeO → Fe (r.6) by ~ 44%. This generates high elastic stresses that once exceeded, can trigger the exacerbated growth of these channels, causing cracks and creep pores. This explains the large cracks propagating along entire cross-sections in samples TF_5/5_10Ni_560, TF_5/5_10Ni_590, all samples in set 3. By contrast, Figure 39 of TF_5/20_17Ni_460 showed isolated, faceted-shaped pores located along grain boundaries and triple junctions. These distinctive shapes likely arise because reduction proceeded more rapidly than sintering, and as densification advanced, grains grew around these pores, trapping them in the grain interiors. With limited mobility, the pores adopted faceted geometries that minimises the interfacial energy by aligning with specific crystallographic planes.

Sample TF_5/5_10Ni_620 (Figure 38) displayed the lowest average pore fraction of 1.1%, corresponding to the highest measured density of 7.30 g/cm^3 based on recorded mass loss and pellet dimensions. This differs from the theoretical Fe-17Ni density of 7.95 g/cm^3 at this porosity. This discrepancy likely arises from measurement uncertainties and from basing pore fraction on only five microstructural sections, thereby underestimating true porosity, especially the larger pores within this sample.

5.3. Interpretation of the final microstructure

A correlation was observed between FCC phase fraction and intercritical annealing temperatures for sets 1 and 2 (Table 5). This aligns with thermodynamic predictions for Fe-10Ni (Table 4), where the maximum predicted reversed austenite fraction was 22%, occurring at an IA temperature of 560 ℃, explaining the increase in FCC fraction as IA temperature decreased in both sets. Higher IA temperatures led to lower FCC fractions due to a reduced thermodynamic driving force for Ni partitioning into FCC, which in turn decreased its stability and retention upon cooling to room temperature. For Fe-17Ni samples, Figure 43(e) predicted an increase in reversed austenite volume fraction; reaching a maximum of 0.53 at IA temperature 520 ℃. This was mirrored through the phase fractions measured, with 490 ℃ being the highest in FCC fraction among the set 3 samples (Table 5).

The same correlation seen in sets 1 and 2 between IA temp and FCC phase fraction was not observed in samples TF_5/20_17Ni_460 and TF_5/20_17Ni_560. Although the equilibrium phase diagram predicted a stronger driving force for FCC formation at 460 ℃ than at 560 ℃, the phase fractions measured by XRD (7% and 8%, respectively) suggests the influence of kinetics during partitoning. At the lower temperature, Ni diffusion is slower compared to that at higher temperatures, so despite the high driving force, the shorter diffusion distances and limited atom mobility restrict the extent of partionining in TF_5/20_17Ni_460. In other words, slow kinetics at lower temperatures versus faster but reduced driving force at higher temperature governs the observed FCC distributions.

Local phase mapping in Figure 46 revealed FCC fractions of 2.27%, 5.57%, and 0.67% for samples annealed at 460 ℃, 490 ℃ and 560 ℃, respectively. Tese local measurements deviate from bulk XRD trends, particularly for TF_5/20_17Ni_560, likely due to the limited sapmling volume of local techniques versus the bulk-averaging nature of XRD. This mismatch indicates microstructural inhomogeneity. As a result, they may over- or under-represent FCC-rich areas depending on the specific microstructural features present within the scanned zone. The observed discrepancies between predicted (Table 4) and measured FCC fractions (Table 5) likely reflect limited Ni diffusion at the applied intercritical annealing temperatures. Achieving full Ni partitioning from BCC into FCC across the observed grain sizes would require much longer hold times to allow equilibrium conditions to be approached.

FCC phases identified in the phase maps were predominantly located at grain boundaries. This, combined with the elevated Ni content measured by point spectra in EDX analysis (Figure 47) for grains situated along HAGBs, strongly indicates that these regions are both FCC in structure and nickel rich. The propagation of secondary phases along higher-energy HAGBs and pore boundaries, as observed in SEM-BSE images, further supports the conclusion that these features correspond to FCC regions, stabilised by local nickel enrichment.

No clear correlation was observed between FCC regions and Ni-rich areas in the phase maps or EDX measurements. This is likely due to the selected measurement parameters selected during EBSD analysis, which limited spatial resolution and sensitivity required to accurately resolve the FCC phases. Thus, the distinct nanoscale features observed in SEM-BSE images, were not observed in phase maps. These features were retained in all samples proving that these are a third phase rather than a product of the reduction and sintering mechanisms. Their invariance, scale and morphology are typical of stable intermetallic compounds. In these systems, $FeNi_3$ formation is favoured at lower temperatures, which precipitated prior to intercritical annealing because of the slow heating rates. XRD alone cannot definitively confirm these compounds, since most of the additional low-intensity h-k-l reflections characteristic of an ordered FCC structure fall below the resolution limit of laboratory XRD when compared to the stronger BCC and disordered-FCC peaks. In addition, limited published work on the microstructural analysis of $FeNi_3$ precipitates in Fe-Ni alloys leads to challenging interpretation of these features.

The marked differences in grain sizes between sets 1 and 2 versus set 3 likely stem from their higher Ni content, which promotes secondary phase nucleation. This is supported by the elevated FCC phase fractions identified by XRD (Table 5) and the increased local FCC fraction visible in the phase maps presented in Figure 46. Among the Fe-17Ni samples, TF_5/20_17Ni_560 exhibited the most refined microstructure, along with the highest BCC fraction measured by XRD (92%). Furthermore, the KAM map displayed in Figure 48, showed the highest overall KAM values for this sample, indicating elevated local lattice distortions. Although no distinct martensitic features were visible in the SEM-BSE images, these observations along with the high fraction of martensite predicted for this sample, are suggestive of martensitic transformation.

The microstructural refinement in TF_5/20_17Ni_560 likely results from a cyclic transformation during annealing, involving the sequence of α' (as quenched martensite)→ γ (reversed austenite)→ α' (fresh martensite). Initially, the as-quenched martensite consists of multiple martensite variants that act as nucleation sites for fine austenite grains during austenite reversion. The reversed austenite, in turn, becomes the parent phase for the subsequent formation of fresh martensite within each of these grains, leading to a highly refined microstructure. A similar refinement was reported by Shirazi et al [39] following austenite reversion for a Fe-11Ni alloy. The associated heat treatment and transformation sequence are illustrated in Figure 21(a). EDX line scans (Figure 47(d-f)) revealed pronounced Ni segregation and depletion in TF_5/20_17Ni_560, with Ni being more localised than uniformly distributed. This observation can be partly explained by the cyclic transformation processes. During austenite reversion, Ni preferentially partitions into the γ phase, but limited diffusion and low driving force localise enrichment around austenite grains. This partitioning is retained during retransformation to martensite, resulting in distinct compositional variations.

As shown in Figure 48(d), the lowest average misorientation angle was recorded for sample TF_5/20_17Ni_490, followed by TF_5/20_17Ni_460. The low misorientation angle in TF_5/20_17Ni_490 supports the detection of the highest FCC fraction, suggesting reduced local lattice strain. If martensite is indeed present in the matrix, this could imply a higher ferrite-to-martensite ratio in this sample. However, distinguishing ferrite from martensite

through ex-situ measurements remains challenging due to their similar crystallographic structure and overlapping features in EBSD imaging. Moreover, the relatively low resolution of SEM-BSE imaging in this study, proved insufficient to resolve typical Fe-Ni martensite, as reported in literature [39]. Consequently, it is not possible to conclusively determine the presence of austenite-memory effects or to quantify the ferrite-to-martensite balance at room temperature.

A summary of key experimental findings and their proposed interpretations for each sample is provided in Table 7.

Table 7. Summary of notable observations and possible explanations for each sample examined in this study.

Sample	Key observations	Explanations
TGA_10/5_ 10Ni_560	• Highest initial mass amongst set • Incomplete reduction degree (0.925) • Lowest mass-loss rates amongst set • Core densest (0.8% pore fraction), edges highly porous (~15 – 19 %)	• High initial mass → dense green body → fewer adsorption sites → slowed reduction → early sintering → closed outward reduction channels prematurely • Distinct microstructural features between residual oxides and reduced microstructure
TGA_10/5_ 10Ni_590	• Lowest initial mass amongst its set • Fastest reduction rate among TGA samples • Low pore fraction (1.58%)	• Loosely packed initial pellet →improved reduction kinetics due to
TGA_10/5_ 10Ni_620	• Consistent pore fraction across sections < 0.56 μm standard deviation • Lowest FCC fraction (1%)	• High initial homogenisation and heterogeneity across sample • Low thermodynamic driving force for Ni partitioning into FCC
TF_5/5_ 10Ni_560	• Inconsistent pore fraction across sample	• Lower homogeneity and/or thermal gradients → higher Fe-oxides, → areas with higher and lower densities
TF_5/5_ 10Ni_590	• Elongated, interconnected pores at section (d)	• Typical of end-stage reduction due to water vapour removal and entrapment by subsequent • Volumetric changes and rapid H_2O egress → stress-driven crack propagation.

TF_5/5_ 10Ni_620	• Lowest initial mass and porosity (1.1%) • Highest measured density (7.3 g/cm^3) • Lowest FCC fraction (1%)	• Faster initial reduction, leading to complete reduction with sufficient sintering • Differences between measured and theoretical densities due to unrepresentative pore fraction • Lowest thermodynamic driving force for FCC nucleation compared to its set
TF_5/20_ 17Ni_460	• High pore interconnectivity • Percolating pores at section Figure 39(e) • Faceted, isolated pores at grain boundaries, and within BCC matrix	• Reduction outpaces sintering → grains grow around trapped pores • Limited pore mobility ⇒ faceted shapes minimize interfacial energy • Short diffusion distance → insufficient Ni mobility • Reduced extent of partitioning at lower temperatures, despite higher driving force
TF_5/20_ 17Ni_490	• Highest FCC fraction (15%) • Lowest strain indicated by KAM	• Highest thermodynamic force for Ni partitioning into austenite, driving higher FCC nucleation • Lower overall strain → higher fraction of FCC & higher ferrite to martensite ratio
TF_5/20_ 17Ni_560	• Finest grains (~0.77 μm) • High local BCC fraction • Highest KAM	• Refined grains formed via cyclic transformation during annealing ($\alpha' \rightarrow \gamma \rightarrow \alpha'$) → multiple martensite variants • Multiplied martensite variants → ultrafine reversed austenite & martensite • Increased local lattice strain

6. Conclusions and future directions

This work implemented the '*one-step oxide-to-bulk-alloy*' hydrogen direct reduction approach to produce ultrafine-grained austenite–ferrite duplex microstructures in Fe–Ni systems. To address gaps in the literature on tailoring microstructures in reduced metal oxides, the study demonstrated microstructural control via a single reduction–sintering–annealing sequence.

6.1. Reduction degree and mechanism behaviour

- Increased Ni content shifted the onset of iron oxide reduction $Fe_2O_3 \rightarrow Fe_3O_4$ to higher temperatures
- Complete reduction (= 1) was observed for Fe-10 wt.% Ni and Fe-17 wt.% Ni when subjected to a heating rate of 5 °C/min and 250 ml partial pressure of hydrogen

6.2. Density and pore mechanisms

- All samples had a pore fraction below 5%, indicative of effective concurrent sintering during reduction.
- The exception, TGA_10/5_10Ni_560, exhibited residual oxides and porous edges indicative of slow reduction kinetics and early sintering. The higher density in the core, proves the shell-like reduction sequence of metal oxides by hydrogen

6.3. Microstructural formation via intercritical annealing

- Fe-10 wt.% Ni specimens exhibited a direct correlation between intercritical annealing temperature and FCC fraction, in agreement with Thermo-Calc simulations, validating predictive thermodynamic modelling.
- Ultrafine-grains were realised in TF_5/20_17Ni_490 (via increased FCC nucleation and impingement) and TF_5/20_17Ni_560 (via cyclic transformations).

✓ The optimised Fe-Ni alloy with the desired microstructure

- Sample TF_5/20_17Ni_490, Fe-17 wt.% Ni, exhibited a fully reduced, dense (< 3% porosity), ultrafine-grained (0.93 ± 0.08 μm) two-phase microstructure comprising a 15% Ni-rich FCC phase (25.63 wt.% Ni) and a 85 vol% Ni-lean BCC phase (14.16 wt.%). Proving the applicability of HyDR to achieve a final bulk alloy with desired microstructures.

Distinguishing austenite from ferrite proved difficult due to poor correlation between phase maps and EDX data and the limited resolution of SEM-BSE imaging; to address this, future work should employ in-situ phase transformation studies (e.g., synchrotron X-ray or high-temperature EBSD) to directly track $\gamma \leftrightarrow \alpha'$ evolution and identify any austenite-memory effects during intercritical annealing, use dilatometry to pinpoint austenite reversion temperatures and quantify their impact on grain-refinement. Comprehensive kinetic analyses of reduction coupled with concurrent sintering including varying heating profiles, H_2 partial pressure, and feedstock parameters can be optimised to promote phase formation and densification.

7. References

[1] J.G.J. Olivier, J.A.H.W. Peters, Trends in global CO2 and total greenhouse gas emissions, The Hague, 2020. www.pbl.nl/en. (accessed January 20, 2025).

[2] International Energy Agency, Iron and Steel Technology Roadmap: Towards more sustainable steelmaking, Paris, 2020. www.iea.org/t&c/ (accessed January 5, 2025).

[3] Worldsteel Association, 2024 World Steel in Figures, Brussels, 2024. https://worldsteel.org/wp-content/uploads/World-Steel-in-Figures-2024.pdf (accessed December 26, 2024).

[4] K. Daehn, R. Basuhi, J. Gregory, M. Berlinger, V. Somjit, E.A. Olivetti, Innovations to Decarbonize Materials Industries, Nat Rev Mater 7 (2022) 275–294.

[5] D. Raabe, The Materials Science behind Sustainable Metals and Alloys, Chem Rev 123 (2023) 2436–2608. https://doi.org/10.1021/acs.chemrev.2c00799.

[6] Climate action and the Green Deal, Brussels, 2022. https://commission.europa.eu/strategy-and-policy/priorities-2019-2024/european-green-deal/climate-action-and-green-deal_en (accessed December 27, 2024).

[7] M. Elias, Nickel laterite deposits-geological overview, resources and exploitation, in: Giant Ore Deposits: Characteristics, Genesis and Exploration, 1st ed., Centre for Ore Deposit Research, University of Tasmania, 2002: pp. 205–220. https://www.researchgate.net/publication/281422746.

[8] Environmental Guidelines for Nickel Smelting and Refining, Washington, 2020. https://www.miga.org/sites/default/files/archive/Documents/NickelSmelting.pdf (accessed February 5, 2025).

[9] M. Pei, M. Petäjäniemi, A. Regnell, O. Wijk, Toward a Fossil Free Future with HYBRIT: Development of Iron and Steelmaking Technology in Sweden and Finland, Metals (Basel) 10 (2020) 972. https://doi.org/10.3390/met10070972.

[10] A. Otto, M. Robinius, T. Grube, S. Schiebahn, A. Praktiknjo, D. Stolten, Power-to-steel: Reducing CO2 through the integration of renewable energy and hydrogen into the German steel industry, Energies (Basel) 10 (2017). https://doi.org/10.3390/en10040451.

[11] P. Cavaliere, Clean Ironmaking and Steelmaking Processes: Efficient Technologies for Greenhouse Emissions, Springer International Publishing, Cham, Switzerland, 2019. https://doi.org/10.1007/978-3-030-21209-4.

[12] S. Wei, Y. Ma, D. Raabe, One step from oxides to sustainable bulk alloys, Nature 633 (2024) 816–822. https://doi.org/10.1038/s41586-024-07932-w.

[13] M. Shiga, Invar alloys, Curr Opin Solid State Mater Sci 1 (1996) 340–348. https://doi.org/10.1016/S1359-0286(96)80023-4.

[14] C. Guillaume, Invar and Its Applications, Nature 71 (1904) 134–139. https://doi.org/10.1038/071134a0.

[15] A. Sahoo, V.R.R. Medicherla, Fe-Ni Invar alloys: A review, Mater Today Proc 43 (2021) 2242–2244. https://doi.org/10.1016/j.matpr.2020.12.527.

[16] T. Ochirkhuyag, D. Tuvshin, T. Tsevelmaa, S.C. Hong, K. Odbadrakh, D. Odkhuu, Fe-Ni based alloys as rare-earth free gap permanent magnets, Acta Mater 268 (2024). https://doi.org/10.1016/j.actamat.2024.119755.

[17] G. Cacciamani, A. Dinsdale, M. Palumbo, A. Pasturel, The Fe–Ni system: Thermodynamic modelling assisted by atomistic calculations, Intermetallics (Barking) 18 (2010) 1148–1162. https://doi.org/10.1016/j.intermet.2010.02.026.

[18] D.R. Gaskell, D.E. Laughlin, Introduction to the Thermodynamics of Materials, CRC Press, Boca Raton, 2024. https://doi.org/10.1201/9781003375388.

[19] P. Atkins, J. De Paula, J. Keeler, Atkin's Physical Chemistry, 11th ed., Oxford University Press, 2017.

[20] Q. Fradet, M. Kurnatowska, U. Riedel, Thermochemical reduction of iron oxide powders with hydrogen: Review of selected thermal analysis studies, Thermochim Acta 726 (2023). https://doi.org/10.1016/j.tca.2023.179552.

[21] O.A. Cortez, F.J. Moura, E. de Albuquerque Brocchi, R.N.C. de Siqueira, R.F.M. de Souza, Fe-Ni Alloy Synthesis Based on Nitrates Thermal Decomposition Followed by H2 Reduction, Metall Mater Trans A 45 (2014) 2033–2039. https://doi.org/10.1007/s11663-014-0221-x.

[22] Y. Ma, I.R. Souza Filho, Y. Bai, J. Schenk, F. Patisson, A. Beck, J.A. van Bokhoven, M.G. Willinger, K. Li, D. Xie, D. Ponge, S. Zaefferer, B. Gault, J.R. Mianroodi, D. Raabe, Hierarchical nature of hydrogen-based direct reduction of iron oxides, Scr Mater 213 (2022). https://doi.org/http://dx.doi.org/10.1016/j.scriptamat.2022.114571.

[23] A. Heidari, N. Niknahad, M. Iljana, T. Fabritius, A review on the kinetics of iron ore reduction by hydrogen, Materials 14 (2021). https://doi.org/10.3390/ma14247540.

[24] M. Pijolat, L. Favergeon, Kinetics and Mechanisms of Solid-Gas Reactions, in: Handbook of Thermal Analysis and Calorimetry, Elsevier B.V., 2018: pp. 173–212. https://doi.org/10.1016/B978-0-444-64062-8.00011-5.

[25] E. Salucci, S. Ghosh, V. Russo, H. Grénman, H. Saxén, Modelling of iron oxide reduction with hydrogen, Comput Aided Chem Eng 52 (2023) 715–720. https://doi.org/10.1016/B978-0-443-15274-0.50114-1.

[26] E.M. Minaev, T.I. Mryakina, Alloyed Powders Produced by Reduction of a Complex Oxide, Poroshkovaya Metall (1968) 1–5.

[27] S.H. Jung, T. Lee, S.W. Song, Y.J. Kwon, H.-G. Kang, C. Dongchul, C.S. Lee, Enhanced Resistance to Delayed Cracking in Deep-drawn Lean Duplex Stainless Steel: the Role of Residual Stress, Korean J of Met and Mater 55 (2017). https://doi.org/10.3365/KJMM.2017.55.8.544.

[28] M. Okayasu, D. Ishida, Effect of Microstructural Characteristics on Mechanical Properties of Austenitic, Ferritic, and γ-α Duplex Stainless Steels, Metall Mater Trans A 50 (2019) 1380–1388. https://doi.org/10.1007/s11661-018-5083-4.

[29] W. Bleck, X. Guo, Y. Ma, The TRIP Effect and Its Application in Cold Formable Sheet Steels, Steel Res Int 88 (2017) 1700218. https://doi.org/10.1002/srin.201700218.

[30] M. Knyazeva, M. Pohl, Duplex Steels: Part I: Genesis, Formation, Structure, Metallogr Microstruct Anal 2 (2013) 113–121. https://doi.org/10.1007/s13632-013-0066-8.

[31] R.L. Miller, Ultrafine-Grained Microstructures and Mechanical Properties of Alloy Steels, Metall Trans 3 (1972) 905–912. https://doi.org/https://doi.org/10.1007/BF02647665.

[32] E.O. Hall, The Deformation and Ageing of Mild Steel: III Discussion of Results, Proc Phys Soc. Section B 64 (1951) 747–753. https://doi.org/10.1088/0370-1301/64/9/303.

[33] X. Guo, P. Liu, Y. Xia, Z. Dong, H. Liu, Y. Chen, Two-step hydrogen reduction of oxides for making FeCoNiCu high entropy alloy: Part I – Process and mechanical properties, Mater Charact 193 (2022). https://doi.org/10.1016/j.matchar.2022.112271.

[34] Y. Ma, Processes, microstructure, and mechanical properties of cold-rolled medium-Mn steel, PhD, Technischen Hochschule Aachen, 2019. http://dnb.ddb.de.

[35] Y. Ma, W. Song, S. Zhou, A. Schwedt, W. Bleck, Influence of intercritical annealing temperature on microstructure and mechanical properties of a cold-rolled medium-Mn steel, Metals (Basel) 8 (2018). https://doi.org/10.3390/met8050357.

[36] J. Shi, X. Sun, M. Wang, W. Hui, H. Dong, W. Cao, Enhanced work-hardening behavior and mechanical properties in ultrafine-grained steels with large-fractioned metastable austenite, Scr Mater 63 (2010) 815–818. https://doi.org/10.1016/j.scriptamat.2010.06.023.

[37] G.E. Dieter, Mechanical Metallurgy, McGraw-Hill, 1986.

[38] H. Shirazi, G. Miyamoto, S. Hossein Nedjad, T. Chiba, M. Nili Ahmadabadi, T. Furuhara, Microstructure evolution during austenite reversion in Fe-Ni martensitic alloys, Acta Mater 144 (2018) 269–280. https://doi.org/10.1016/j.actamat.2017.10.068.

[39] H. Shirazi, G. Miyamoto, S. Hossein Nedjad, H. Ghasemi-Nanesa, M. Nili Ahmadabadi, T. Furuhara, Microstructural evaluation of austenite reversion during intercritical annealing of Fe-Ni-Mn martensitic steel, J Alloys Compd 577 (2013). https://doi.org/10.1016/j.jallcom.2012.02.015.

[40] S.L. Kang, Sintering: Densification, Grain Growth & Microstructure, Elsevier, 2005.

[41] L. Klinger, E. Rabkin, Sintering of spherical particles of two immiscible phases controlled by surface and interphase boundary diffusion, Acta Mater 61 (2013) 2607–2616. https://doi.org/10.1016/j.actamat.2013.01.040.

[42] B. Tougas, C. Blais, F. Chagnon, S. Pelletier, Characterization of Nickel Diffusion and its Effect on the Microstructure of Nickel PM Steels, Metall Mater Trans A 44 (2013) 754–765. https://doi.org/10.1007/s11661-012-1417-9.

[43] W.J.C. Price, M.M. Rebbeck, A.S. Wronski, Comparison of heat treatment response of wrought and sintered bt1 grade high speed steel, Powder Metall 28 (1985) 79–84. https://doi.org/10.1179/pom.1985.28.2.79.

[44] E. De Moor, D.K. Matlock, J.G. Speer, M.J. Merwin, Austenite stabilization through manganese enrichment, Scr Mater 64 (2011) 185–188. https://doi.org/10.1016/j.scriptamat.2010.09.040.

[45] H. Yang, H. Bhadeshia, Austenite grain size and the martensite-start temperature, Scr Mater 60 (2009) 493–495. https://doi.org/10.1016/j.scriptamat.2008.11.043.

[46] S.-J. Lee, K.-S. Park, Prediction of Martensite Start Temperature in Alloy Steels with Different Grain Sizes, Mater Metall Trans A 44 (2013) 3423–3427. https://doi.org/10.1007/s11661-013-1798-4.

[47] B.C. De Cooman, The State-of-the-Knowledge on Medium Mn Steel, in: Proc Int Conf Adv Mater Syst & High Mn Steels (ICAS & HMnS 2016), Pohang University of Science and Technology, Jeju, Korea, 2016: pp. 35–41.

[48] W. Steven, A.G. Haynes, The Temperature of Formation of Martensite and Bainite in Low-Alloy Steels, J Iron Steel Ins 183 (1956) 349–359.

[49] D.P. Koistinen, R.E. Marburger, A general equation prescribing the extent of the austenite-martensite transformation in pure iron-carbon alloys and plain carbon steels, Acta Metall 7 (1959) 59–60. https://doi.org/10.1016/0001-6160(59)90170-1.

[50] Y.-K. Lee, J. Han, Current opinion in medium manganese steel, Mater Sci Tech 31 (2015) 843–856. https://doi.org/10.1179/1743284714Y.0000000722.

[51] B.C. De Cooman, The State-of-the-Knowledge on Medium Mn Steel, Materials Design Laboratory, Jeju, Korea, 2016.

[52] Z. Liao, Y. Dong, Y. Du, X. Wang, M. Qi, H. Wu, X. Gao, L. Du, Effects of different intercritical annealing processes on microstructure and cryogenic toughness of newly designed medium-Mn and low-Ni steel, J Mater Res Technol 23 (2023) 1471–1486. https://doi.org/10.1016/j.jmrt.2023.01.058.

[53] J. Zhu, H. Luo, Z. Yang, C. Zhang, S. van der Zwaag, H. Chen, Determination of the intrinsic α/γ interface mobility during massive transformations in interstitial free Fe-X alloys, Acta Mater 133 (2017) 258–268. https://doi.org/10.1016/j.actamat.2017.05.045.

[54] X. Zhang, G. Shen, C. Li, J. Gu, Phase-field simulation of austenite reversion in a Fe-9.6Ni-7.1Mn (at.%) martensitic steel governed by a coupled diffusional/displacive mechanism, Mater Des 188 (2020). https://doi.org/10.1016/j.matdes.2019.108426.

[55] O. Dmitrieva, D. Ponge, G. Inden, J. Millán, P. Choi, J. Sietsma, D. Raabe, Chemical gradients across phase boundaries between martensite and austenite in steel studied by atom probe tomography and simulation, Acta Mater 59 (2011) 364–374. https://doi.org/10.1016/j.actamat.2010.09.042.

[56] K. Zhang, D. Tang, H.-B. Wu, Effect of Heating Rate Before Tempering on Reversed Austenite in Fe-9Ni-C Alloy, J Iron Steel Res Int 19 (2012) 73–78. https://doi.org/https://doi.org/10.1016/S1006-706X(13)60011-4.

[57] Z. Cai, S. Li, D. Zhang, L. Ma, Y. Feng, J. Hu, R.D.K. Misra, The Significant Influence of Cooling Rate and Intercritical Annealing Temperature on Austenite Stability and Relationship to Mechanical Behavior in Medium Manganese Steel, Steel Res Int 94 (2023). https://doi.org/10.1002/srin.202200571.

[58] J. Han, A.K. da Silva, D. Ponge, D. Raabe, S.M. Lee, Y.K. Lee, S.I. Lee, B. Hwang, The effects of prior austenite grain boundaries and microstructural morphology on the impact toughness of intercritically annealed medium Mn steel, Acta Mater 122 (2017) 199–206. https://doi.org/10.1016/j.actamat.2016.09.048.

[59] J.M. Marder, A.R. Marder, The morphology of iron-nickel massive martensite, Trans ASM 62 (1969) 1–10.

[60] H. Bhadeshia, R. Honeycombe, Formation of Martensite, in: Steels: Microstructure and Properties, 4th Edition, Elsevier, 2017: pp. 135–177. https://doi.org/10.1016/B978-0-08-100270-4.00005-6.

[61] G. Kurdjomov, G. Sachs, Over the mechanisms of steel hardening, Z Phys 64 (1930) 325–343.

[62] Z. Nishiyama, Martensitic Transformation, Academic Press, 1978.

[63] L. Kaufman, M. Cohen, The martensitic transformation in the iron-nickel system, JOM (1956) 1393–1401.

[64] R.A. Grange, Strengthening steel by austenite grain refinement, Trans ASM (1966) 26–48.

[65] S.-J. Lee, Y.-M. Park, Y.-K. Lee, Reverse transformation mechanism of martensite to austenite in a metastable austenitic alloy, Mater Sci Eng A 515 (2009) 32–37. https://doi.org/10.1016/j.msea.2009.02.010.

[66] C.A. Apple, G. Krauss, The effect of heating rate on the martensite to austenite transformation in Fe-Ni-C alloys, Acta Metall 20 (1972) 849–856. https://doi.org/10.1016/0001-6160(72)90077-6.

[67] R. Kossowsky, D.A. Colling, Correlation of coercive force to microstructure in cyclic martensite → austenite transformations in an Fe-Ni-Co alloy, Metall Trans 4 (1973) 799–806. https://doi.org/10.1007/BF02643090.

[68] A. Alaei, H. Jafarian, A.R. Eivani, Observation austenite memory and significant enhancement of tensile properties during cyclic reverse martensite transformation in a Fe-Ni-C TRIP steel, Mater Sci Eng: A 676 (2016) 342–350. https://doi.org/10.1016/j.msea.2016.09.003.

[69] S. Lee, S.-J. Lee, B.C. De Cooman, Austenite stability of ultrafine-grained transformation-induced plasticity steel with Mn partitioning, Scr Mater 65 (2011) 225–228. https://doi.org/10.1016/j.scriptamat.2011.04.010.

[70] L.J. Swartzendruber, V.P. Itkin, C.B. Alcock, The Fe-Ni (iron-nickel) system, J Phase Equilib 12 (1991) 288–312. https://doi.org/10.1007/BF02649918.

[71] E.S. Machlin, An Introduction to Aspects of Thermodynamics and Kinetics Relevant to Materials Science, 3rd ed., Elsevier, Oxford, 2007.

[72] H.K.D.H. Bhadeshia, Theory of Transformations in Steels, CRC Press, CRC Press, 2021. https://doi.org/10.1201/9781003056782.

[73] E. Brandes, G. Brook, Smithells Metals Reference Book, 7th ed., B&H, 1999.

[74] R.E. Smallman, A.H.W. Ngan, Surfaces, Grain Boundaries and Interfaces, in: Modern Physical Metallurgy, 8th ed., Elsevier, 2014: pp. 415–442. https://doi.org/10.1016/B978-0-08-098204-5.00010-9.

[75] H.I. Aaronson, Mechanisms of the massive transformation, Metall Mater Trans A 33 (2002) 2285–2297. https://doi.org/10.1007/s11661-002-0352-6.

[76] H. Bhadeshia, Phase transformations in metals and alloys: Lecture notes, (2000). https://www.phase-trans.msm.cam.ac.uk/2000/C9/lectures45.pdf (accessed June 1, 2025).

[77] M. Al-Buainain, D.C. Dunand, Sustainable Fe-Cr-Ni Stainless Steels via Hydrogen Reduction of Blended Oxides, ACS Sustain Chem Eng (2025). https://doi.org/10.1021/acssuschemeng.5c02264.

[78] ASTM E3-11: Standard Guide for Preparation of Metallographic Specimens., West Conshohocken, PA, 2017. https://doi.org/10.1520/E0003-11.

[79] ASTM E112-24: Standard Test Methods for Determining Average Grain Size, West Conshohocken, PA, 2024. https://doi.org/10.1520/E0003-11.

[80] B.D. Cullity, S.R. Stock, Elements of X-ray diffraction, 3rd ed., Pearson Education Limited, 2014.

[81] Y. Zhang, W. Wei, X. Yang, F. Wei, Reduction of Fe and Ni in Fe-Ni-O systems, Journal of Mining and Metallurgy, Section B: Metallurgy 49 (2013) 13–20. https://doi.org/10.2298/JMMB120208038Z.

[82] A. Rukini, M.A. Rhamdhani, G.A. Brooks, A. Van den Bulck, Metals Production and Metal Oxides Reduction Using Hydrogen: A Review, J Sustain Metall 8 (2022). https://doi.org/10.1007/s40831-021-00486-5.

[83] S.H. Kim, X. Zhang, Y. Ma, I.R. Souza Filho, K. Schweinar, K. Angenendt, D. Vogel, L.T. Stephenson, A.A. El-Zoka, J.R. Mianroodi, M. Rohwerder, B. Gault, D. Raabe, Influence of microstructure and atomic-scale chemistry on the direct reduction of iron ore with hydrogen at 700°C, Acta Mater 212 (2021). https://doi.org/10.1016/j.actamat.2021.116933.